Wegener Center
SCIENTIFIC REPORT
109 | 2024

Evaluating the Performance of the CCLM in Representing Subsidence Inversions: A Case Study of the Basin of Graz

David Kneidinger

December 2024

Climate Change Graz
Field of Excellence
University of Graz

Wegener Center

UNI GRAZ

The Wegener Center for Climate and Global Change is an interdisciplinary, internationally recognized research and graduate education institute of the University of Graz that is pooling the University's expertise in Climate, Environmental and Global Change. It brings together research teams and scientists from fields such as geophysics and climate physics, meteorology, economics, geography, and social sciences. At the same time, close links are maintained and further developed with many national and international cooperation partners. The research interests range from monitoring, analysis, and modeling of climate and environmental change to the investigation of climate change impacts and the analysis of the human dimensions of these changes related to mitigation, adaptation, and loss & damage. More information at **wegcenter.uni-graz.at**.



Alfred Wegener (1880 – 1930), after whom the Wegener Center is named, was founding holder of the University of Graz Geophysics Chair (1924 – 1930). In his work in the fields of geophysics, meteorology, and climatology he was a brilliant scientist and scholar, thinking and acting in an interdisciplinary way, far ahead of his time with this style. The way of his ground-breaking research on continental drift is a shining role model. His sketch on the relations of continents based on traces of an ice age about 300 million years ago (left) as basis for the Wegener Center Logo is thus a continuous encouragement to explore equally innovative ways: paths emerge in that we walk them (motto of the Wegener Center).

SR 109 | 2024 Evaluating the Performance of the CCLM in Representing Subsidence Inversions: A Case Study of the Basin of Graz
ISBN 978-3-9508053-6-8 December 2024

Suggested citation:
Kneidinger, D. (2024), Evaluating the Performance of the CCLM in Representing Subsidence Inversions: A Case Study of the Basin of Graz, Wegener Center Scientific Report 109-2024, Wegener Center Verlag, University of Graz, Austria, December 2024. ISBN 978-3-9505053-8-2

(c) 2024 Wegener Center Verlag, University of Graz, Austria
The usage of images, tables, or texts of this Scientific Report is permitted for non-commercial purposes if appropriate credit is given.
For any other purposes, please contact: wegcenter@uni-graz.at

Publishing institution:
Wegener Center for Climate and Global Change, University of Graz
Brandhofgasse 5, 8010 Graz, wegcenter.uni-graz.at

Contact: David Kneidinger
david.kneidinger@uni-graz.at

David Kneidinger, BSc

Evaluating the Performance of the CCLM in Representing Subsidence Inversions: A Case Study of the Basin of Graz

MASTER'S THESIS

to achieve the university degree of

Master of Science

Master's degree programme: Physics

submitted to

Graz University of Technology

Supervisor

Mag. Dr.rer.nat. Heimo Truhetz

Wegener Center for Climate and Global Change

University of Graz

Graz, June 2024

Abstract

The Basin of Graz frequently experiences temperature inversions that significantly impact local temperatures, cloud cover, and aerosol accumulation. Long-term (period from 1961 to 2020) observational records of temperature in Graz indicate that the characteristics of inversions during winter time have changed due to climate change: the magnitude, the height, the frequency of occurrence as well as the intensity have decreased. The analysis of the weather types during inversion periods, i.e., periods with consecutive days of temperature inversions, shows that the occurrence of anticyclonic weather types has a significant impact on the formation and strength of temperature inversions in the Basin of Graz. A reduction in the frequency of the anticyclonic weather type relate to the found decrease in the number of inversion events over the last 60 years. Furthermore, the records show a stronger warming trend in winter on inversion days compared to non-inversion days, with an additional warming trend for minimum temperatures of 0.1 K per decade and for maximum temperatures of 0.2 K per decade. Multiple linear regression analyses show that inversion magnitude significantly contributes to the warming trend on local temperature during inversion days. For the seasonal maximum temperatures, increased sunshine duration additionally contributes significantly to the warming trend on inversion days. These findings highlight the critical need for accurate representation of temperature inversions in Regional Climate Models (RCMs), for reliable local climate assessments and future climate projections. To assess the performance of COSMO model in CLimate Mode (CCLM) in representing subsidence temperature inversions, convection permitting simulations with 3 km×3 km grid spacing of a large scale inversion event in January 2009 are conducted. The results indicate that CCLM captures the presence of the inversion quite well, however the model under represents the inversion magnitude and erroneously underestimates the inversion layer bottom height, introducing considerable biases in modeled temperature and radiation fields, with the biases reaching values of up to 8 K for minimum temperatures and 4 K for maximum temperatures.

A preliminary analysis of the evaluation runs of the CORDEX-FPSCONV ensemble shows that a correct representation of subsidence inversion is still challenging for state-of-the-art convection permitting models.

Abstract (Deutsch)

Das Grazer Becken erfährt häufig Temperaturinversionen, die lokale Temperaturen, Bewölkung und Aerosolanreicherung erheblich beeinflussen. Langzeitbeobachtungen der Temperatur in Graz aus dem Zeitraum von 1961 bis 2020, basierend auf dem Spatiotemporal Reanalysis Dataset for Climate in Austria (SPARTACUS), zeigen, dass sich die Eigenschaften der Winterinversionen aufgrund des Klimawandels verändert haben: Die Stärke, die Höhe, die Häufigkeit des Auftretens sowie die Intensität haben abgenommen. Die Analyse der Wettertypen während Inversionsperioden zeigt, dass das Auftreten von Hochdruck Wetterlagen eine erhebliche Wirkung auf die Entstehung und Stärke von Temperaturinversionen im Grazer Becken hat. Die Abnahme der Häufigkeit von dieser Wetterlage von September bis Dezember steht im Zusammenhang mit dem festgestellten Rückgang der Anzahl der Inversionsereignisse in den letzten 60 Jahren. Darüber hinaus zeigen die Aufzeichnungen einen stärkeren Erwärmungstrend im Winter an Inversionstagen im Vergleich zu Nicht-Inversionstagen, mit einem zusätzlichen Erwärmungstrend für die Minimumstemperaturen von 0.1 K pro Jahrzehnt und für die Höchsttemperaturen von 0.2 K pro Jahrzehnt. Multiple lineare Regressionsanalysen zeigen, dass die Stärke der Inversionen signifikant zum Erwärmungstrend der lokalen Temperatur an Inversionstagen beiträgt. Für die saisonalen Höchsttemperaturen trägt die erhöhte Sonnenscheindauer zusätzlich signifikant zum Erwärmungstrend an Inversionstagen bei. Diese Erkenntnisse unterstreichen die kritische Notwendigkeit einer genauen Darstellung von Temperaturinversionen in RCMs für verlässliche lokale Klimabewertungen und zukünftige Klimaprojektionen. Um die Fähigkeit von CCLM bei der Darstellung von Subsidenztemperaturinversionen zu bewerten, werden konvektionserlaubende Simulationen mit einer Gitterweite von 3 km×3 km eines starken Inversionsereignisses im Januar 2009 durchgeführt. Die Ergebnisse zeigen, dass CCLM das Vorhandensein der Inversion gut erfasst, jedoch die Stärke der Inversionen unterschätzt und die Höhe der Inversionsschicht fälschlicherweise zu niedrig ansetzt, was zu erheblichen Verzerrungen in den modellierten Temperatur- und Strahlungsfeldern führt, wobei diese Abweichungen bis zu 8 K für minimums Temperaturen und 4 K für maximums Temperaturen erreichen. Eine vorläufige Analyse der Evaluationsläufe des CORDEX-FPSCONV-Ensembles zeigt, dass eine korrekte Darstellung der Subsidenzinversion auch für moderne konvektionserlaubende Modelle eine Herausforderung bleibt.

Acknowledgements

I would like to begin my thesis with a heartfelt expression of gratitude to all those who have supported me throughout my academic journey. I am deeply grateful to my supervisor, Dr. Heimo Truhetz, for his invaluable guidance throughout the duration of my thesis. Dr. Truhetz consistently made time to discuss my ideas and findings, granting me the freedom to explore my academic interests fully. His knack for making complex concepts readily understandable and ensuring that I left every meeting with enhanced knowledge has truly made him the ideal supervisor for me.

I would also like to express my gratitude to the `Grazer Wechselseite` for supporting the thesis financially. Additionally I want to thank the Vienna Scientific Cluster (VSC) for providing the computational resources for my thesis, as well as the `Geosphere Austria` and Ulrich Voggenberger for providing several datasets for my research. The CCLM community has also been a great help in providing me with the necessary tools and resources for this thesis.

I also thank my family, whose unwavering support and financial backing were crucial in my pursuit of higher education. Their encouragement has been a cornerstone of my academic journey.

Special thanks go to my girlfriend, Kathi, who has patiently listened to my extended discussions on my thesis topic for over a year.

I owe a particular debt of gratitude to Gerald Brunner, the man with the question, leading to this thesis: *"Why does it seem that a few years back I always had fog outside of my office in Stattegg, whereas now the winter months seem to be primary sunny"*.

I would also like to thank my friend Peter, who has significantly enhanced my coding skills and his readiness to assist with any question or task has been invaluable. Lastly, I am thankful to my fellow students, Peter and Laurenz, for their insightful discussions on the topic and their meticulous proofreading of my thesis results. Their contributions were immensely helpful in refining my final manuscript.

Contents

1 Introduction **1**

2 Theory and Basics **4**

2.1 The Climate System and Meteorological Basics 4

2.1.1 The Earth's Atmosphere 6

2.1.2 Temperature Inversion 8

2.2 Regional Climate Modelling 14

3 Data and Methods **16**

3.1 Data 16

3.1.1 SPARTACUS 16

3.1.2 SNOWGRID 17

3.1.3 APOLIS 17

3.1.4 Station Data 17

3.1.5 ERA5 17

3.1.6 Radio Sonde Data 18

3.1.7 RCM Model Ensemble 18

3.2 CCLM Simulations 19

3.3 Study Domain 23

3.4 Statistical Methods 24

3.4.1 Linear Regression 24

3.4.2 Generalized Linear Models and Log-Model 26

3.4.3 Theil-Sen Estimator 28

3.4.4 Box-Cox Transformation 28

3.5 Analysis Methods 29

3.5.1 Temperature profiles and Inversion Parameters 29

3.5.2 Classification of Weather Types 31

3.5.3 Definition of Inversion Events 34

3.5.4 Regression Analyses of Temperature and Sunshine Data 36

3.5.5 Spatial Bias plots and Conservative Remapping 39

4 Results and Discussion **40**

4.1 Observation Based Analysis - Temperature Inversions in Graz from 1961 to 2021 . . . 40

4.1.1 Inversion parameters . . . 40

4.1.2 Inversion Events . . . 45

4.1.3 Modelling Temperature Station Data . . . 53

4.1.4 Sunshine Duration . . . 60

4.2 Inversion Event 2009 . . . 64

4.2.1 Synoptic Conditions . . . 64

4.2.2 Representation in CCLM . . . 72

4.2.3 Temperature Profiles in the CORDEX-FPSCONV ensemble . . . 78

4.3 Reliability of the Study . . . 81

5 Summary and Conclusion **83**

Acronyms **85**

List of Figures **87**

List of Tables **89**

Bibliography **90**

6 Appendix **98**

1 Introduction

Climate change is one of the most pressing challenges of our time, with its impacts already noticeable on a global scale. Understanding the underlying processes and mechanisms on regional and local scales is crucial for developing effective adaptation and mitigation strategies. The Alpine region, being particularly vulnerable to climate change due to altitude-dependent warming, underscores the need to understand mountain temperature trends (Pepin et al. 2015).

In this context, the city of Graz, located in the southeast of Austria, serves as a case study to investigate the local climate and its interactions with the surrounding topography. The city is situated in a valley basin, surrounded by hills and mountains, which can lead to the formation of temperature inversions, i.e., the reversal of the otherwise typical temperature decrease with altitude within the planetary boundary layer (Gohm et al. 2009).

Due to their wide-ranging impacts on atmospheric variables and processes, temperature inversions have attracted considerable attention in climate research. Notably, the relationship between decreasing temperatures and increasing relative humidity, coupled with the formation of low stratus clouds and fog, affects incoming short-wave radiation while reducing outgoing long-wave radiation fluxes. Cities like Graz, prominent for experiencing temperature inversions during the winter months with very little sunshine, face significant implications for the local climate and urban environment. The investigation of possible future changes is thus of great interest. The inherent stability during temperature inversions suppresses convection, resulting in limited vertical moisture movement and potential implications for precipitation patterns. Strong inversions may also lead to the accumulation of air pollutants, particularly in valley-based cities like Graz (Gohm et al. 2009; Almbauer et al. 2000).

Additionally, temperature inversions can lead to late frost events, which can have severe impacts on agriculture and vegetation (Tadić et al. 2023).

Various mechanisms can lead to the formation of temperature inversions, such as radiative cooling, which most often occurs during clear nights with light winds and low humidity, allowing the surface too cool rapidly. Another mechanism is the subsidence of air masses, which can occur when a widespread layer of descending air meets a relatively weak temperature lapse rate and is heated by adiabatic compression. The advection of air masses can

also lead to the formation of a temperature inversion, when warm air advects over a cooler air mass or when a cold air mass undercuts a warm air mass (Schnelle Jr and Brown 2016).

While the general mechanisms of temperature inversions are well understood, their spatial and temporal variability and the interactions with the local topography are still subjects of ongoing research (Hiebl and Schöner 2018).

With the limited availability of long-lasting vertical temperature measurements in mountainous regions, the study of these phenomena becomes particularly challenging. In this context, grid-based reanalysis datasets like the Spatiotemporal Reanalysis Dataset for Climate in Austria (SPARTACUS) can be used to investigate the local phenomena as shown in Hiebl and Schöner (2018). The SPARTACUS dataset provides a high spatial resolution of $1\,\mathrm{km} \times 1\,\mathrm{km}$ and a daily temporal resolution of minimum temperature, making it well suited to investigate the local nature of the inversion phenomena in the Basin of Graz.

Other than exploring the local past climate based on observational data, Regional Climate Models (RCMs) can give valuable insights into the dynamics of phenomena and provide a tool to not only investigate the past but also future climate. The necessity of having local phenomena correctly represented in RCMs is crucial for the development of effective future climate scenarios. Having phenomena like temperature inversions not accurately represented in RCMs can lead to a biased future climate, especially if the phenomena are expected to change in the future.

While the confidence of climate change when it comes to global patterns of surface temperature is high, which is primarily controlled by the thermodynamics. The confidence in the atmospheric circulation aspect of climate change, which is primarily controlled by the dynamics and exert a strong control on regional climate, is lower (Shepherd 2014). It is stated in Davini and D'Andrea (2016) that recent Global Climate Models (GCMs) still exhibit biases in midlatitude atmospheric blocking and the associated atmospheric circulation patterns. These biases in the circulation patterns can propagate from the large-scale circulation to the regional scale in RCMs (Maraun et al. 2021; Jury et al. 2019). When it comes to temperature inversions, the large-scale weather type can have a significant impact on the formation and strength of temperature inversions (Li et al. 2015; Kassomenos et al. 2014). For these reason this study examines the influence of synoptic weather types on inversion periods, i.e., periods with consecutive days of temperature

inversions.

This study also investigate the occurrence of temperature inversions in the Basin of Graz and their changes over time by comparing the climate reference period of 1961-1990 to the recent period of 1991-2020. In order to understand the impact of temperature inversions on the local climate, the influence of the mean seasonal inversion magnitude on minimum and maximum temperatures in Graz is investigated Additionally, the research seeks to understand the variations in sunshine duration between inversion days and non-inversion days, aiming to illuminate how these atmospheric phenomena contribute to local climatic differences. In order to explore the performance of RCMs in representing temperature inversions, a particularly strong inversion event in January 2009 is simulated with the COSMO model in CLimate Mode (CCLM) (Böhm et al. 2006). For this, two simulations are conducted, using ECMWF Reanalysis v5 (ERA5) (Hersbach et al. 2020) as driving data. The first simulation (CCLM-3km) directly downscales ERA5 to a 0.0275° grid, which has a resolution of 3 km×3 km. The second simulation (CCLM-3km-nested) first downscales to a 0.22° grid (≈ 25 km) and then to the 0.0275° grid. This two-step nesting approach, common in RCMs and broadly accepted in the Coordinated Regional Climate Downscaling Experiment (CORDEX) (Giorgi et al. 2009).

The thesis is structured as follows: chapter 2 provides an overview of the basics of the climate system as well as a description of two most common types of temperature inversions: radiative inversions and subsidence inversions. The basics of regional climate modeling is introduced in section 2.2. chapter 3 describes the data used in this study and gives details about the two Consortium for Small-scale Modeling (COSMO) simulations conducted with the model CCLM. Additionally all methods necessary for the analysis as well as the statistical methods used are described.

The results are presented in chapter 4. chapter 5 provides a summary of the results of the study.

2 Theory and Basics

This chapter gives an overview of the basic concepts and theories that are relevant to the work presented in this thesis. It provides the reader with background information about the meteorological concepts as well as the basics of Regional Climate Modelling.

2.1 The Climate System and Meteorological Basics

The climate system is a complex and dynamic entity, described by Gettelman and Rood (2016) as follows: The earth's climate system is driven by the sun. The atmosphere mediates the flow of energy between the sun and the earth, through the action of clouds and greenhouse gases. Commonly, the climate system is divided into subsystems, or so-called spheres. These include the liquid hydrosphere, which encompasses water in all its liquid forms, such as oceans, rivers, lakes, and water in the atmosphere. The solid cryosphere contains all forms of solid water, including glaciers, ice caps, and snow. The biosphere, together with the anthroposphere, encloses all living organisms and their interactions with the environment, as well as human-made structures and systems. The lithosphere is the solid part of the Earth, often referred as land, comprising the crust and the upper mantle. Lastly, the atmosphere is the gaseous envelope surrounding the Earth. With its small heat capacity and consequently fast response time, the atmosphere is the most dynamic part of the climate system and its where weather phenomena occur.

The climate system represents more than just the sum of its parts. These individual systems are coupled together and interact with each other through cycles and feedback mechanisms. Additionally, the climate system is influenced by external factors such as volcanic eruptions, and human activities, all of which can alter the Earth's energy balance and trigger changes in the climate system. A schematic sketch of the components of the climate system is shown in Figure 2.1.

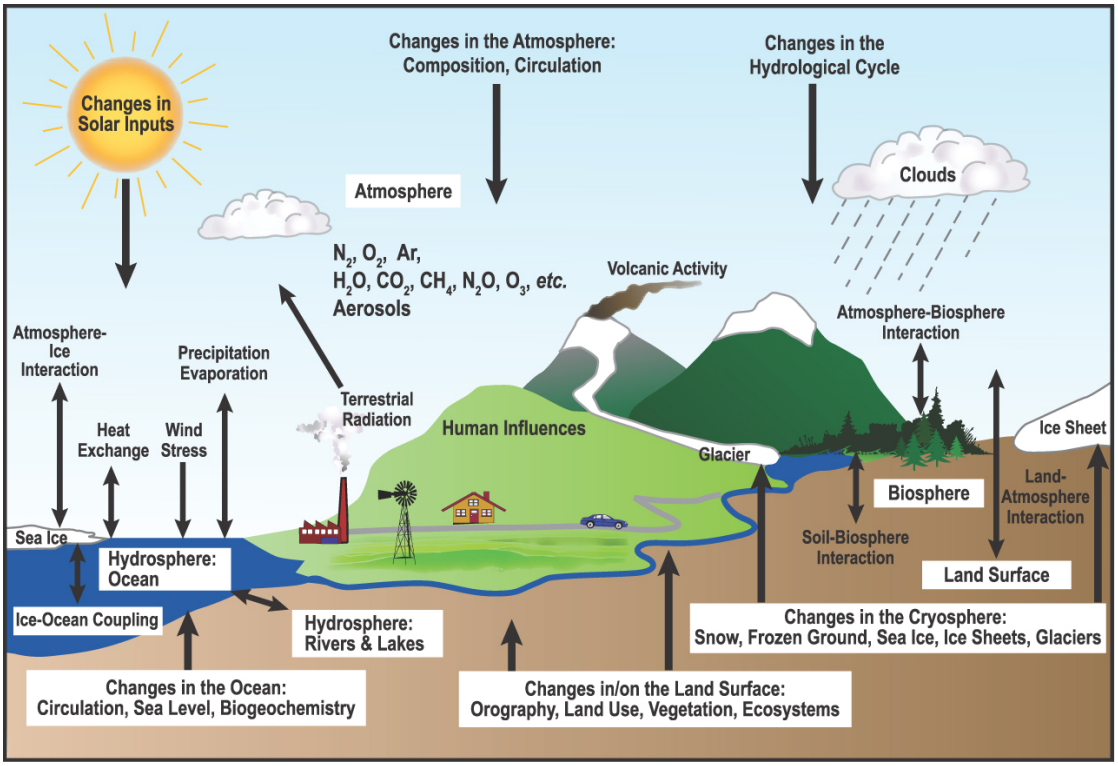


Figure 2.1: Schematic sketch of the components of the climate system. The figure also shows important processes and interactions in the climate system. (Treut et al. 2007)

2.1.1 The Earth's Atmosphere

In Caballero (2014) the atmosphere is described as a thin layer of gases that surrounds the Earth and is retained by the Earth's gravity. It is composed of 78 % nitrogen, 21 % oxygen, 0.9 % argon, and trace amounts of other gases such as carbon dioxide, neon, helium, and hydrogen. Because of the long residence time of these gases in the atmosphere, their number fraction is essentially constant in space and time. This fictitious mixture of gases is called dry air. Water vapor is the most important variable component of the atmosphere and is the only atmospheric constituent that can exist in all three phases at the typical pressures and temperatures found in the Earth's atmosphere. In condensed form it is responsible for the formation of clouds and can precipitate out as rain. It can evaporate from the surface and form cloud and rain droplets. Since these processes happen at a short timescale, the residence time of water vapor in the atmosphere is very short, the concentration of water vapor in the atmosphere is highly variable in space and time. It can vary from anything between 0 % in the stratosphere to 5 % of the total volume in the tropics. The annual global average pressure of water vapor can be seen in Figure 2.2 (a). For that reason the approximation of considering the atmosphere of a two component gas, made up of dry air and water vapor, is reasonable.

A common classification of the atmospheric layers is based on the vertical temperature profile. The troposphere is the lowest layer of the atmosphere and is characterized by a decrease in temperature with height. This is the layer where most of the weather phenomena occur. It reaches up to a mean height of 8 km to 15 km, where a stable layer called the tropopause separates it from the stratosphere. The stratosphere is characterized by an increase in temperature with height, mostly caused by the absorption of ultraviolet radiation by the ozone layer. The stratosphere reaches up to a mean height of 50 km, where the stratopause separates it from the mesosphere. The mesosphere is again characterized by a decrease in temperature with height and reaches up to a mean height of 85 km, where the mesopause separates it from the thermosphere. The annual-mean temperature profile of the atmosphere is shown in Figure 2.2 (b).
In atmospheric science, the troposphere is of particular interest, as it is the layer where most of the weather phenomena occur. The vertical temperature gradient inside the troposphere is called the lapse rate and is on average about $6\,^{\circ}\mathrm{C\,km^{-1}}$ (Caballero 2014).

Depending on the lapse rate, the atmosphere can be locally stable, conditionally stable or unstable. In Figure 2.3 (a) the environmental lapse rate is illustrated, whereas below the condensation level the dry adiabatic lapse rate is shown in red and above the

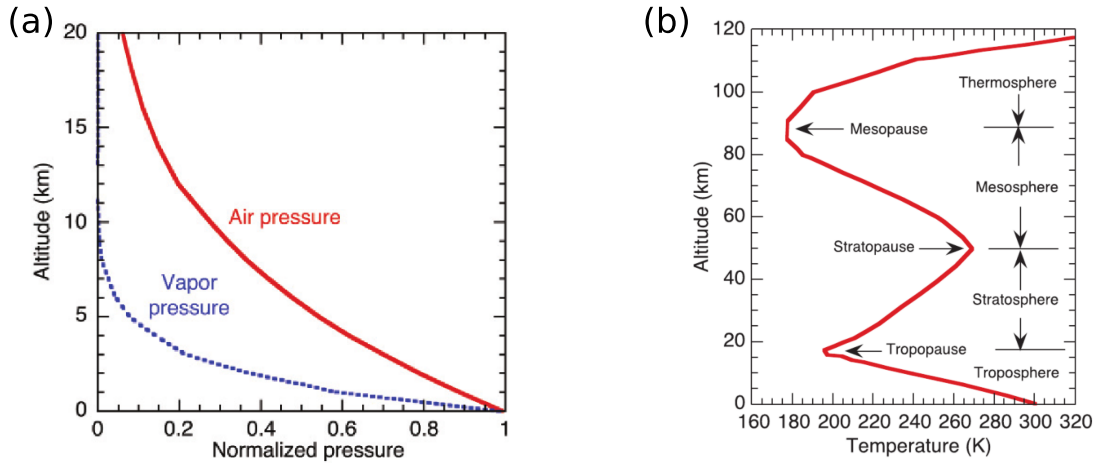


Figure 2.2: (a) Vertical profiles of air pressure and partial pressure of water vapor for globally and annually averaged conditions. (b) The main zones of the atmosphere defined according to the temperature profile of the standard atmosphere at 15°N for annual-mean conditions. (Hartmann 2016)

condensation level the moist adiabatic lapse rate is shown in blue. If an air parcel is lifted adiabatically, it will cool with the dry adiabatic lapse rate below the condensation level and with the moist adiabatic lapse rate above the condensation level. The temperature where condensation sets in is called the dew point. If the air parcel finds itself cooler, hence denser, than its surroundings it will sink back to its original position. This is called absolute stability, as illustrated in Figure 2.3 (b).

If the environmental lapse rate is between the dry adiabatic lapse rate and the moist adiabatic lapse rate, the atmosphere is considered to be conditionally stable (Figure 2.3 (b)). In this case, the atmosphere is stable as long as the air parcel is saturated, but unstable if it is unsaturated. The atmosphere is instable1 if the lifted air parcel is warmer, hence less dense, than its surroundings and will continue to rise. This is illustrated in Figure 2.3 (c).

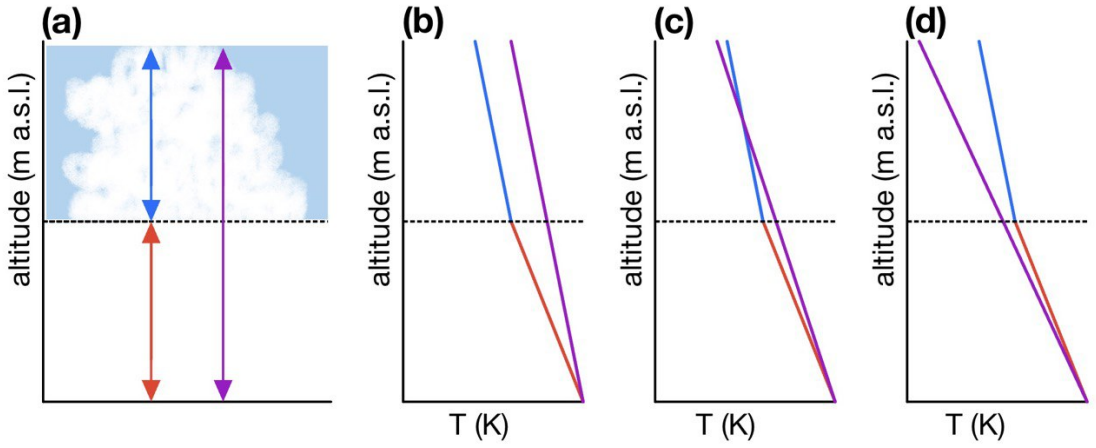


Figure 2.3: The environmental lapse rate is shown in purple, the dry adiabatic lapse rate in red and the moist adiabatic lapse rate in blue. The black dashed line marks the condensation level. (b) absolute stability, (c) conditional instability (d) absolute instability

2.1.2 Temperature Inversion

As noted previously, temperature generally decreases with altitude in the troposphere. However, when temperature increases with altitude, this phenomenon is known as a temperature inversion. Temperature inversions reverse the typical temperature gradient, creating a stable atmospheric layer where the cooler air below is trapped by warmer air above. This stability inhibits vertical air mixing and can significantly influence atmospheric conditions. For instance, within an inversion layer, the cooler temperatures can lead to increased relative humidity as the capacity of air to hold water vapor diminishes with dropping temperatures, consistent with the Clausius-Clapeyron relation (see Equation 2.1). The lower temperatures can drop below the dew point, which can lead to the formation of low stratus clouds and fog. These on the one hand block incoming short-wave radiation, but on the other hand reduce the outgoing long-wave radiation flux. The very stable stratification during temperature inversions, reduces the process of convection, resulting in less vertical movement of moisture and less precipitation. Strong inversions can even lead to accumulation of air pollutants, especially in valley based cities such as Graz (Gohm et al. 2009; Almbauer et al. 2000). Inversions can emerge from different processes and can be classified accordingly. In the following, the two most common types for the Alpine Region are described.

Radiation Inversion

In fair weather conditions, without any disturbance by clouds or background flow, the temperature inside the basin undergoes a diurnal cycle, which evolves similarly every day. This process is described by Zardi and Whiteman (2013) and illustrated in Figure 2.4 as follows: During the day, the ground is heated by the incoming solar radiation and the air becomes well mixed, resulting in a neutral temperature profile. In the late afternoon, as shadows cast over the sidewalls, the net long-wave radiation loss exceeds the net solar shortwave radiation. This reverses the net radiation energy flux, resulting in downward turbulent sensible heat flux removing heat from a shallow air layer above the slopes as shown in Figure 2.4 (a). As the shadows on the basin sidewalls moves further and takes up a larger area, hence removing the local energy budget, downslope airflows begin as cold air layers form over the slopes. During this downslope flow the air is on the one hand adiabatically warmed, but on the other hand it get's cooled from the ground (Figure 2.4 (b)). As the cooling effect of the ground is dominant a cold air layer starts to form on the basin floor. The air layers that come afterwards no longer have enough temperature deficit to reach all the way to the basin floor, hence they converge near the top of the growing inversion layer (Figure 2.4 (c)). Observations show that much of the cooling in a basin takes place continuously throughout the basin's full depth, and this cooling continues throughout the night, even after the downslope flows slow and die as the ambient stability builds up within the basin. As the sun rises, its rays start warming the basin's floor and sidewalls, introducing convective currents into the previously stable, stratified air mass. This warming effect is not uniform; it varies across different parts of the basin due to the angle of solar incidence, terrain features, and the existing atmospheric conditions. This differential heating of the basin floor and sidewalls generates convective turbulence, which in turn starts to mix the cold air near the surface with the warmer air above (Figure 2.4 (d)). The process is further facilitated by the development of upslope flows. As the sidewalls warm, the air in contact with these slopes becomes buoyant and begins to rise, which draws more air from the basin's interior. This movement contributes to the vertical mixing of air masses, further eroding the inversion layer. The strength of these upslope flows, and consequently their effectiveness in breaking up the inversion, can vary with the basin's size and shape. Wider basins may experience slower inversion breakup due to weaker subsiding motions. Those temperature inversions or cold-air pools can even last for multiple days. Multi-day temperature inversions typically occur during winter months and arise when the daytime incoming energy is not enough to disperse the cold air that has accumulated in the basin or valley. This accumulation of cold air could

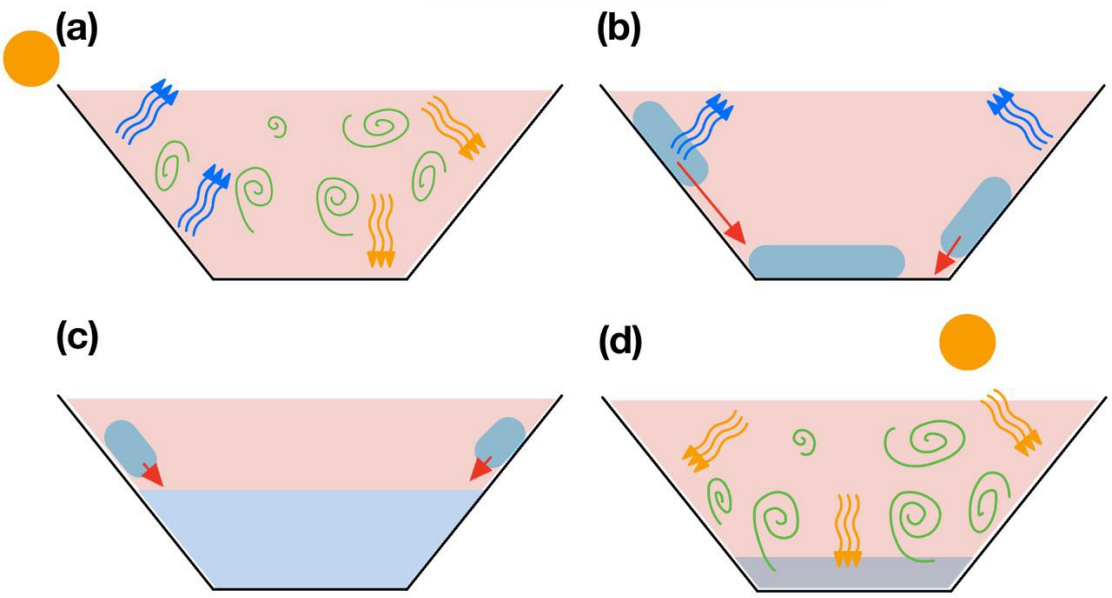


Figure 2.4: A simplified diurnal cycle in basins; Green curls illustrate vertical mixing of air, orange arrows show the solar radiation that heats the basin floor and sidewalls, blue arrows show the radiative cooling of the basin floor and sidewalls. The red arrows show the downslope flow of cold air, which adiabatically warms the air as it descends. (a) Late afternoon as the shadows cast over the basins sidewalls and radiative cooling starts. (b) Downslope flows start as the radiative cooling of the basin floor and sidewalls is dominant. (c) A cold layer of air forms on the basin floor and the air layers that come afterwards converge near the top of the growing inversion layer. (d) The sun rises and starts to warm the basin floor and sidewalls, introducing convective currents into the previously stable air mass.

be a result of the standard processes that form nocturnal inversions or could remain after a cold front has passed through low-lying areas. At any stage of their development, inversions can either intensify through differential advection if relatively warm air moves over the basin, or weaken if cold air is moved over it. The reduced daylight hours of winter, the sun's lower trajectory, and snow coverage commonly lead to alterations in the surface energy budget at the basin's floor, diminishing the daytime turbulent sensible heat flux and convection needed to dissipate the inversion. Moreover, the formation of fog or stratus clouds within the cold-air pool can further decrease solar radiation and sensible heat flux at the base of the cold pool.

Subsidence Inversion and Frontal Inversion

In contrast to radiation inversions, subsidence inversions are commonly observed aloft, although they can also be observed at the surface (Kim et al. 2010). They are caused by the sinking of air in the atmosphere as follows: When a high pressure system is present, the air in the center of the high pressure system is starting to sink widespread (Figure 2.5 (a)). During this sinking process, the air warms adiabatically. As the air sinks, it's also compressed and the vertical distance between the air parcels is reduced. Therefore a parcel starting from higher altitude, does move further in vertical direction compared to a parcel starting from lower altitude. Hence it is warmed more, which leads to the formation of an inversion layer as illustrated in Figure 2.5 (b). When additionally enough moisture is present in the air, the formation of clouds is possible. The resulting vertical temperature profile with the formation of clouds below the inversion layer bottom is shown in Figure 2.5 (c). This is the case if the air below the inversion layer cools down to the dew point temperature and the relative humidity reaches 100 %. (Ahrens and Henson 2021; Lutgens and Tarbuck 2013; Moran et al. 1997; Glickman and Society 2000)

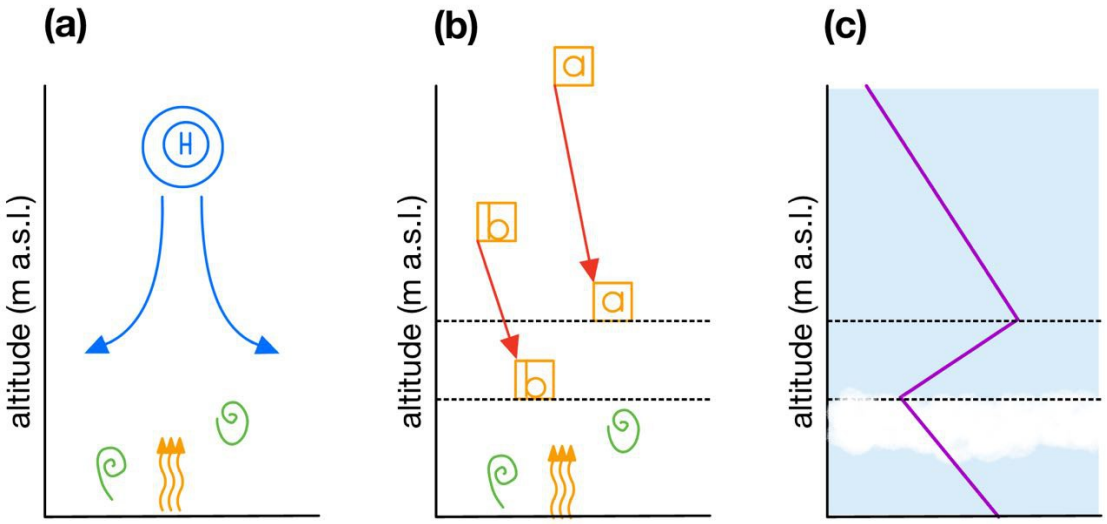


Figure 2.5: (a, b) Illustration of the process of subsidence inversion. Two air parcels are shown: one starting from higher altitude and one from lower altitude. The air parcels are compressed as they sink, leading to a warming of the air parcels. Blue arrows show the sinking air, red arrows show the warming of the air parcels.
(c) The vertical temperature profile is shown in purple. Dashed lines mark the inversion layer bottom and layer top.

Frontal inversions are caused by large-scale advection and occur when a warm air mass overruns a cold air mass (warm front) or when a cold air mass undercuts a warm air mass (cold front) (Hiebl and Schöner 2018). Although subsidence inversions and frontal inversions both can be found aloft and might show similar temperature profiles, they can be distinguished when comparing the specific humidity profiles inside the inversion layer (Namias 1935). Due to that reason the difference in dew point temperature (ΔT_d) can be used as an indicator for distinction between those two types. Anticyclonic subsidence inversions present a gradual decrease of the dew point with height, whereas the dew point of frontal activity inversions usually increases with height (Kassomenos and Koletsis 2005). This can be explained as follows: Subsidence inversions are characterized by air sinking and warming, leading to a decrease in relative humidity and a gradual decrease of the dew point with height. As air descends and warms adiabatically during a subsidence inversion, its capacity to hold moisture increases (Equation 2.1), leading to a reduction in relative humidity RH (Equation 2.2) and a consequent decrease in the dew point with height. The Clausius-Clapeyron equation describes the relationship between the saturation vapor pressure of water and temperature, looks as follows

$$\frac{\mathrm{d}p_s}{\mathrm{d}T} = \frac{L}{T\Delta v}, \tag{2.1}$$

where p_s is the saturation vapor pressure, T is the temperature of water, L is the latent heat of vaporization, and v is the specific volume of water vapor. Since

$$\mathrm{RH} = \left(\frac{e}{p_s}\right) \times 100\%, \tag{2.2}$$

where e represents the actual water vapor pressure in the air, and p_s is the maximum water vapor pressure air can hold at a particular temperature, indicating saturation.

In contrast, frontal activity inversions, associated with frontal systems, can trap moist air near the surface or bring moist air aloft, often resulting in an increase of the dew point with height. This is indicated by an increase in moisture content in the atmosphere at higher altitudes.

2.2 Regional Climate Modelling

The attempt to comprehend the Earth's climate system's vast complexity and the long temporal and spatial scales and simply the the common definition of the climate normal as the average of 30 years (Arguez and Vose 2011) makes it impossible to conduct experiments in the laboratories. Performing controlled experiments would require regulated settings and the possibility to repeat the experiments under the same conditions. Since this is simply not possible with the Earth's climate system, climate models emerge as essential instruments for simulating and predicting climate dynamics (Edwards 2010).

The genesis of climate modelling can be traced back to simple Energy Balance Model (EBM)s aimed at understanding the Earth's radiation budget. This quest expanded with the pioneering work of Manabe and Wetherald (1967) in the mid-20th century, who developed the first atmospheric models that coupled radiative transfer with hydrological cycles and formed the basis for modern three-dimensional climate modelling. Further advancements were propelled by Hasselmann (1976), who included the development of models that account for the stochastic nature of the climate system. Thereby integrated the weather's chaotic behavior into climate predictions (Hasselmann, 1976). The complexity of climate models saw significant advancements with the introduction of Global Climate Models (GCMs), which simulate the global circulation of the atmosphere and oceans. GCMs marked a paradigm shift by incorporating dynamic components of the Earth system, allowing for a comprehensive understanding of climate processes. Those models are based on the coupled differential equations called the primitive equations, which describe the conservation of mass, momentum, and energy in the atmosphere and oceans (Edwards 2010). Although based on physical equations, their are still many processes that are just not resolved by the coarse grid of the GCMs, which is about $100\,\mathrm{km} \times 100\,\mathrm{km}$ (Fox-Rabinovitz et al. 2006).

The relatively coarse resolution of GCMs, while effective for global-scale processes, often falls short in capturing the finer details required for regional climate analysis. One of the primary sources of uncertainty in course resolution models are the used parameterization schemes, especially for physical processes that are not resolved by the model grid, like moist convection (Severijns and Hazeleger 2005). This is where Regional Climate Models (RCMs) come into play, originating from the work of Giorgi and Bates (1989).

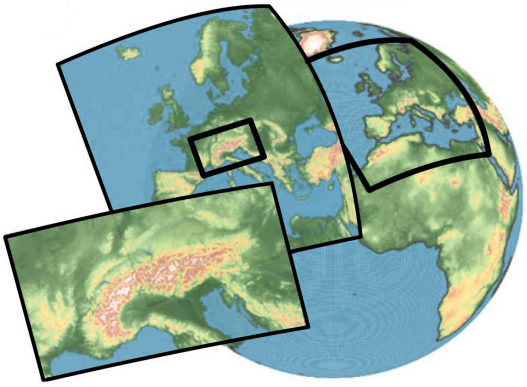


Figure 2.6: Visualization of limited-area modelling. The skematic shows how small scale RCMs are embedded in large resolution GCMs or reanalysis data. The skematic figure shows a two step nesting: first nesting step to the EURO-CORDEX domain and the second nesting step downsales to the Alpine Region (Prein et al. 2015).

To address this limitation, RCMs focus on a defined geographical area, providing high-resolution climate data within this domain. This approach allows for detailed studies of regional climate patterns and phenomena without the prohibitive computational demands that a similar increase in the resolution in GCMs would entail. RCMs work by integrating into the broader framework provided by GCMs, other RCMs or for hindcast simulations even reanalysis datasets. This nested structure enables RCMs to utilize detailed discretization steps, thereby offering resolutions up to less than 3 km. In Figure 2.6 such a nested structure is illustrated. Such a high resolution is essential for accurately representing small-scale processes, like convection and orographic effects, that are otherwise simplified or omitted in GCMs due to their coarse grids. Similar to GCMs the numerical algorithms employed in RCMs solve physical equations through discretization, a process that translates continuous variables into a finite set of discrete points, enabling the simulation of complex climate dynamics on a regional scale.

Advances in modelling have led to the development of convection-permitting models, which significantly refine grid resolutions (e.g., to 1 km×1 km) to directly simulate deep convection without the need for parametrization. These models offer improved representations of surface features and atmospheric processes but require substantial data storage and high-resolution reference datasets for model evaluations (Jacob et al. 2014; Prein et al. 2015; Suklitsch et al. 2011b; Prein and Gobiet 2011; Suklitsch et al. 2011a).

3 Data and Methods

In this chapter the used data as well as some key methods used for the analysis are presented. The chapter is divided into two main sections, the first section 3.1 presents the used data and the second section 3.5 presents the methods used for creating the temperature profiles and the inversion parameters, as well as all further methods used in the analysis.

3.1 Data

3.1.1 SPARTACUS

The Spatiotemporal Reanalysis Dataset for Climate in Austria (SPARTACUS) (Johann Hiebl 2016; Johann Hiebl 2017) is a gridded dataset with a spatial resolution of 1 km×1 km and covers whole of Austria from 1960 until the present. SPARTACUS is provided by the Austrian climate service `Geosphere`. To account for the complex and highly variable thermal distributions in mountainous regions, SPARTACUS has been developed using a novel interpolation method that estimates nonlinear temperature profiles with altitude and accounts for the non-Euclidean spatial representativity of station measurements (Johann Hiebl 2016). The spatial analysis builds upon 150 station series in and around Austria (homogenised where available), all of which extend over or were gap-filled to cover the entire study period. As shown in Hiebl and Schöner (2018) the SPARTACUS dataset is able to capture the temperature inversions quite accurately and it also covers a long time period, which is crucial for the analysis of long term trends. Since radio sonde data is not available for the whole study period in this study, the SPARTACUS dataset is used to create the vertical temperature profiles for the inversion analysis.

3.1.2 SNOWGRID

SNOWGRID Klima v2.1 (Olefs et al. 2020) is a gridded dataset of the Austrian climate service `Geosphere` and provides daily snow depth and snow water equivalent on a 1 km×1 km grid. It is a snow cover model that is coupled to the Geosphere now casting system INCA (Haiden et al. 2011). The model simulates the temporal development of snow depth and snow water equivalent across all of Austria in 15 minute intervals (input data: INCA fields and topographic data). The model is being developed in parallel with resolutions of 1 km×1 km and 100 m×100 m for the entire country of Austria. Independent verification and an update of the model are conducted using satellite data on snow cover. With this gridded dataset snowcover biases in the COSMO model in CLimate Mode (CCLM) simulations are detected.

3.1.3 APOLIS

APOLIS (Olefs and Schoener 2012) is a gridded dataset of the austrian climate service `Geosphere` with a spatial resolution of 100 m×100 m. The daily data gives information about the ground level radiation and is based on satellite observations.

The data is used to investigate the radiation and cloud cover conditions of the CCLM simulations, with the use of daily sum of direct solar radiation on the horizontal surface.

3.1.4 Station Data

All station data used in this study is provided by `Geosphere Austria` via its data portal: https://data.hub.geosphere.at/group/stationsdaten. The following data is used for the study of the influence of inversions on seasonal trends of the winter months from 1960-2020: daily maximum and minimum temperature, daily sunshine duration duration. The station used is Graz University, if not stated otherwise.

3.1.5 ERA5

ECMWF Reanalysis v5 (ERA5) (Hersbach et al. 2020) is the fifth generation of European Centre for Medium-Range Weather Forecasts (ECMWF) atmospheric

reanalysis of the global climate covering the period from January 1940 to present. ERA5 is distributed by the Copernicus Climate Change Service at ECMWF. It provides hourly estimates of a large number of atmospheric, land and oceanic climate variables. The data covers the Earth on a 25 km grid and resolves the atmosphere using 137 levels from the surface up to a height of 80 km. Moreover, ERA5 also includes information about uncertainties of all of its variables at reduced spatial and temporal resolutions. In this study ERA5 is used for the analysis of the large scale atmospheric circulation patterns (subsection 3.5.2) and as driving data for the CCLM simulations.

3.1.6 Radio Sonde Data

The Radio Sonde Data, provided by Ulrich Voggenberger, Institute of Meteorology at University Vienna, includes the real path balloon drift estimates presented in Voggenberger et al. (2023). It contains vertical measurements of air temperature, eastward and northward wind components, geopotential height, and relative humidity along the estimated path of the radiosonde balloon. For better comparability the data is brought from the pressure levels to height h by using the geopotential ϕ

$$h = \frac{\phi}{g_0},$$

with $g_0 = 9.806\,65\,\mathrm{m\,s^{-1}}$. Since only the lowest 3000 m are used, this approximation is valid. The dataset covers four different stations: Graz (Austria), Ljubljana (Slovenia), Zagreb (Croatia), and Udine (Italy), in the period of January 2009. The data is used to validate the temperature profiles created from the SPARTACUS and to investigate the horizontal scale of the subsidence temperature inversion event in January 2009.

3.1.7 RCM Model Ensemble

Coppola et al. (2020) presents the first multi-model ensemble of regional climate simulations[1] at kilometer-scale horizontal grid spacing of about 3 km×3 km, CORDEX-FPSCONV. The ensemble contains 23 simulations, driven by ERA-Interim reanalysis, and performed by 22 European research groups. The individual ensemble members are used in this study to investigate the representation of a strong temperature inversion

[1] https://link.springer.com/article/10.1007/s00382-021-05708-w/tables/1

event in January 2009 in broadly accepted Regional Climate Models (RCMs). For that 2 m temperature as well as the according orography data is used.

3.2 CCLM Simulations

The model of the Consortium for Small-scale Modeling (COSMO), CCLM (Böhm et al. 2006; Rockel et al. 2008), is a non-hydrostatic limited-area atmospheric prediction model designed for operational numerical weather prediction and climate simulations. Originally developed at the Deutscher Wetterdienst and known as Lokal Modell (LM), it evolved into Consortium for Small-scale Modeling (COSMO) through contributions from several European weather services. The model, operates on a rotated geographical grid and a terrain-following height coordinate system, utilizing a 2 time-level Runge-Kutta time-split scheme for dynamic simulations. The CCLM employs a non-hydrostatic approach to solve the thermo-hydrodynamic equations of compressible flow in a moist atmosphere, allowing for highly resolved simulations (grid spacing < 10 km) particularly effective in complex terrain. It includes prognostic variables such as the three wind components, pressure and temperature perturbations, specific humidity, cloud water, ice, rain, snow, and graupel content, along with turbulent kinetic energy. Parameterization schemes handle sub-grid scale processes like radiation, convection, or turbulence. Operating over confined geographic areas, CCLM supports grid spacings ranging from 3 km to 50 km and has been successfully applied in climate research initiatives such as CORDEX-FPSCONV [2] (Coppola et al. 2020; Ban et al. 2021) and EURO-CORDEX [3] (Jacob et al. 2014; Jacob et al. 2020), optimizing both grid spacing and time stepping to manage computing time constraints effectively.

For the model experiment CCLM is used. As initial and lateral boundary conditions the ERA5 reanalysis data, with a horizontal grid resolution of 0.25° and a temporal resolution of 1 hour, is used. The preprocessing and interpolation of the ERA5 data is done using the tool that comes with CCLM, the INT2LM (version 2.0.9). For the starting point of the simulation, the 01 October 2008 is chosen, although the inversion event in January 2009 is of interest. This allows for a spin-up time of three months, which assures that the accumulation of snow as well as the soil moisture is in a realistic state. For the simulations two different approaches are used:

[2] https://www.hymex.org/cordexfps-convection/wiki/doku.php
[3] www.euro-cordex.eu

(1) The first simulation is directly nested in the ERA5 data to a 0.0275° grid (CCLM version 5.0.14), which is approximately 3 km×3 km resolution. This simulation is in the following referred to as CCLM-3km.
The model configuration and parameterisations of CCLM-3km are shown in Table 3.1.

Table 3.1: Model configuration and parameterisations of CCLM-3km

Model version	5.0.14
Horizontal grid spacing	0.0275° (∼ 3 km)
Time step [seconds]	25
No. grid cells	522 × 490
No. vertical atmospheric levels	50
Output interval [hour]	1
Lateral sponge zone	20 grid cells
Radiation scheme	(Ritter and Geleyn 1992)
Convection scheme	(Tiedtke 1989) for shallow convection, only
Microphysics scheme	One-moment scheme including graupel (Doms and Baldauf 2013)
Planetary boundary layer scheme	Prognostic turbulent kinetic energy scheme with 2.5 order closure (Mellor and Yamada 1982)
Land surface scheme	TERRA_ML (Rockel et al. 2008) with 10 soil layers
Lower boundary of soil layers [m b. g. l.]	0.005, 0.025, 0.07, 0.16, 0.34, 0.7, 1.42, 2.86, 5.74, 11.5
Land use data	GLC2000 (Bartholomé and Belward 2005)
Soil data	Digital Soil Map of the World (FAO-Unesco 1981)

(2) The second setup is used to mimic the CORDEX-FPSCONV configuration of the Karlsruhe Institute of Technology (KIT). A two step nesting approach is used, where the 0.25° grid of ERA5 is downscaled first to a 0.22° grid (CCLM version 5.0.10) and then this data is used as driving data for the 0.0275° simulation (CCLM version 5.0.14). This simulation is in the following referred to as CCLM-nested-3km. The model configuration and parameterisations of both nests of CCLM-nested-3km are shown in Table 3.2.

In Raffa et al. (2021) it is shown for CCLM that the one-step nesting or direct nesting experiment tendentially outperforms the two-step nesting approach. The results of precipitation data at different spatial and temporal scales, were better in line with the other existing reanalysis products. Although it is stated that these results can be highly model and event dependent. The domains of the simulations are shown in Figure 3.1

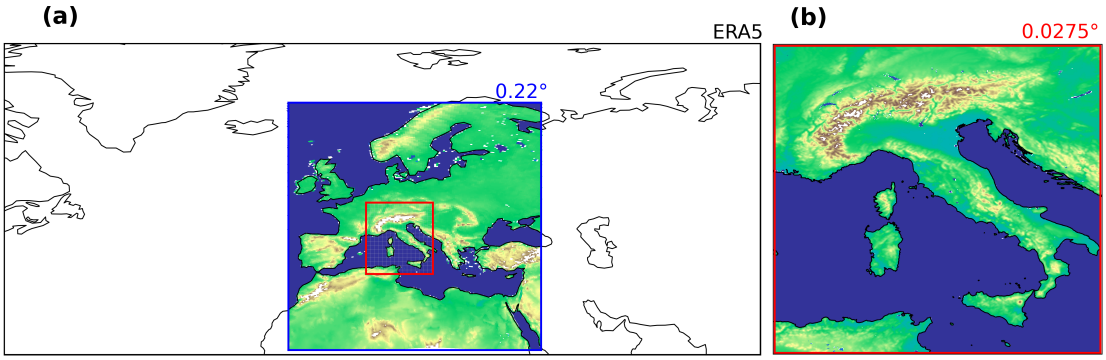


Figure 3.1: Model domains of the CCLM simulations and the model's orography
(a) The domain of the first nesting of CCLM-nested-3km (0.22°) marked with a blue box and the domain of the 0.0275° grid marked with a red box.
(b) 0.0275° domain

All the simulations where computed at the Vienna Scientific Cluster (VSC-5) [4].

[4] https://vsc.ac.at/

Table 3.2: Model configuration and parameterisations of CCLM-nested-3km. $*$ denotes that the parameterisation is the same as in the first nest.

Simulation	CCLM-nested-3km first nest	CCLM-nested-3km second nest
Model version	5.0.10	5.0.14
Horizontal grid spacing	0.22° ($\sim$ 25 km)	0.0275° ($\sim$ 3 km)
Time step [seconds]	150	25
No. grid cells	232×226	522×490
No. vertical atmospheric levels	40	50
Output interval [hour]	1	1
Radiation scheme	(Ritter and Geleyn 1992)	$*$
Convection scheme	(Tiedtke 1989) for shallow convection, only	$*$
Microphysics scheme	One-moment scheme including graupel (Doms and Baldauf 2013)	$*$
Planetary boundary layer scheme	Prognostic turbulent kinetic energy scheme with 2.5 order closure (Mellor and Yamada 1982)	$*$
Land surface scheme	TERRA_ML (Rockel et al. 2008) with 10 soil layers	$*$
Lower boundary of soil layers [m b. g. l.]	0.005, 0.025, 0.07, 0.16, 0.34, 0.7, 1.42, 2.86, 5.74, 11.5	$*$
Land use data	GLC2000 (Bartholomé and Belward 2005)	$*$
Soil data	Digital Soil Map of the World (FAO-Unesco 1981)	$*$

3.3 Study Domain

For the analysis of temperature inversions of the past decades, the Basin of Graz in Austria is chosen as the study domain (see Figure 3.2). The Basin of Graz, located in southeastern Austria, is a part of the larger Styrian Basin within the Eastern Alpine foreland. This intermontane basin is characterized by a relatively flat and open valley floor surrounded by higher mountain ranges, including the Central Eastern Alps to the north and the Slovenian border to the south. The Mur, flowing from northwest to southeast, is the primary watercourse traversing the basin, contributing to its alluvial plains. Elevation within the Graz Basin varies, with the valley floor at approximately $300-500$ m above sea level. The crests of the mountains bordering at the north are about 400 m higher (Ernst Stadlober 2008). The basin's open topography towards the southeast allows for the movement of air masses, whereas the encircling mountains can act as barriers, leading to the development of temperature inversions (Almbauer et al. 2000). For the study domain the Koralpe, with its highest peak: the Großer Speikkogel with 2140 m above sea level, is included in order to get enough data points of larger vertical extend, to capture most inversion tops.

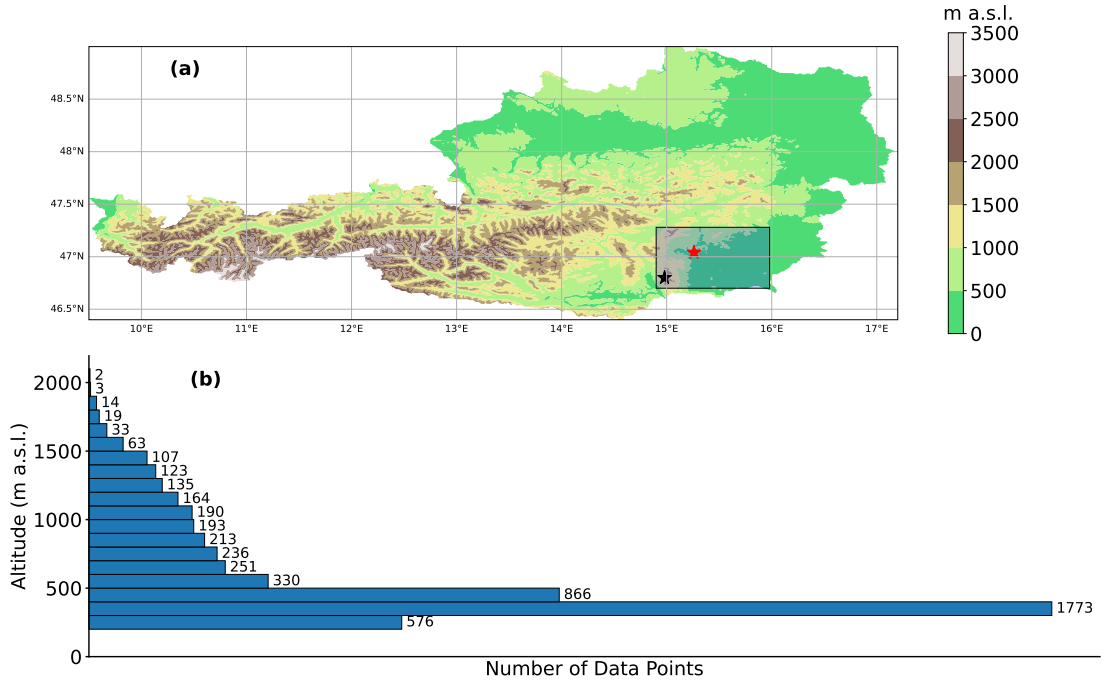


Figure 3.2: (a) Topography of the SPARTACUS surface altitudes in its 1 km×1 km grid. The study domain of the Basin of Graz, Austria is marked with a black box. The Koralpe, the highest mountain in the study domain, is marked with a black star. The city of Graz is marked with a red star.
(b) Vertical distribution of SPARTACUS surface altitudes binned to 100 m intervals.

3.4 Statistical Methods

3.4.1 Linear Regression

The following statistical methods are standard tools used in regression analysis and can be read in James et al. (2013).

Linear regression is a fundamental statistical tool for understanding the relationship between a dependent variable and one or more independent variables. At its core, simple linear regression facilitates the investigation of a linear relationship between a dependent variable, denoted as Y, and a single independent variable, X. This relationship is typically modeled by the equation

$$Y = \beta_0 + \beta_1 X + \eta, \tag{3.1}$$

where β_0 represents the intercept of the regression line, β_1 denotes the slope of the regression line (indicating the expected change in Y for a one-unit change in X), and η encapsulates the residuals, accounting for the deviation of the observed values from the line defined by the linear model.

In the analysis of more complex phenomena, however, the methodological approach extends beyond simple linear regression to encompass multiple linear regression. This extension allows for the inclusion of multiple predictors, thereby providing a more nuanced understanding of the factors. The general form of the multiple linear regression model is given by

$$Y = \beta_0 + \beta_1 X_1 + \beta_2 X_2 + \cdots + \beta_n X_n + \eta, \tag{3.2}$$

where $X_1, X_2, \ldots, X_n$ represent the independent variables, and $\beta_1, \beta_2, \ldots, \beta_n$ are the coefficients associated with each predictor. The model is then estimated using Ordinary Least Squares (OLS), which seeks to minimize the sum of the squared residuals, yielding the optimal values for the coefficients.

The assessment of model fit, particularly through the examination of the R-squared statistic, provides insight into the proportion of variance in the dependent variable that can be explained by the independent variables

$$R^2 = 1 - \frac{\sum_{i=1}^{n}(Y_i - \hat{Y}_i)^2}{\sum_{i=1}^{n}(Y_i - \bar{Y})^2}. \tag{3.3}$$

However, the interpretation of this metric, along with the model's coefficients, necessitates careful consideration of potential issues such as multicollinearity. This phenomenon, where predictors exhibit high correlations with one another, can significantly impact the reliability of the regression coefficients. Techniques such as the calculation of Variance Inflation Factors (VIF) are thus implemented to detect and address multicollinearity, ensuring the robustness of the model's findings. Additionally the Condition Number can give valuable insights into the stability of the regression model and might indicate multicollinearity. It should be noted that a high condition number can occur in models with an intercept, since the intercept is very sensitive to small movements in the data points, hence the Variance Inflation Factors, without the intercept should be used to detect multicollinearity. In order to have numerical stability the condition number should be well below the reciprocal of the machine precision, which is about 10^{16}

for double precision floating point numbers (Haidar et al. 2020).

Furthermore, the Adjusted R-squared statistic provides a more adjusted measure of the goodness of fit, accounting for the number of predictors in the model, thereby offering a more conservative estimate than the R-squared statistic. This is crucial in models with multiple predictors, as it adjusts for the model's complexity.

The F-statistic and its corresponding p value assess the overall significance of the regression model. Specifically, the F-statistic tests the null hypothesis that all regression coefficients are equal to zero versus the alternative that at least one is not. A low probability value indicates that the model provides a better fit than an intercept-only model.

Akaike Information Criterion (AIC) and Bayesian Information Criterion (BIC) are measures used to compare models. Both consider the likelihood of the model and the number of parameters, with BIC providing a stricter penalty for models with more parameters. Lower values of AIC and BIC suggest a better-fitting model. These two methods are used to find the inversion parameters that are most suitable for the regression analysis. This is done by comparing the AIC and BIC values of the models with different inversion parameters.

Log-Likelihood indicates the log of the likelihood function, which measures the goodness of fit of a model. Higher values indicate a better fit.

The analysis of regression models is conducted using the Python module `statsmodels` (Seabold and Perktold 2010). This module provides a comprehensive suite of tools for the estimation and interpretation of linear regression models, facilitating a deep understanding of the dynamics influencing the dependent variable.

The descriptions and interpretations of the parameters mentioned are based on the documentation and functionalities provided by `statsmodels`.

3.4.2 Generalized Linear Models and Log-Model

Generalized Linear Models (GLMs) extend the linear modeling framework presented in subsection 3.4.1 to accommodate non-normal response distributions, as detailed in James et al. (2013). This flexibility allows GLMs to be applied to a wider range of data types, including binary, count, and categorical data.

At the core of GLMs is the relationship between the dependent variable Y and one or more independent variables X. Unlike linear regression, which assumes a normally distributed response variable, GLMs assume that the response variable belongs to the exponential family of distributions, such as Gaussian, Binomial, Poisson, or Gamma distributions.

GLMs consists of three components:

1. **Random Component**: Specifies the probability distribution of the response variable Y. For instance, in the context of count data, a Poisson distribution is often used.

2. **Systematic Component**: Represents the linear predictor η, defined as a linear combination of the independent variables.

3. **Link Function**: Connects the mean of the response variable μ to the linear predictor η. The link function $g(\cdot)$ transforms the expected value of Y to the scale of the linear predictor.

The general form of GLMs can be expressed as:

$$E(Y) = \mu = g^{-1}\left(\beta_0 + \beta_1 X_1 + \beta_2 X_2 + \cdots + \beta_n X_n\right) = g^{-1}\eta, \tag{3.4}$$

where $E(Y) = \mu$ is the expected value of Y, η is the linear predictor, $X_1, X_2, \ldots, X_n$ are the independent variables, and $\beta_0, \beta_1, \ldots, \beta_n$ are the regression coefficients.

Log-Model

One common application of GLMs is the Log-Model, particularly useful for modeling count data or positive-valued responses. In this model, the link function is the logarithm, making it appropriate for Poisson-distributed response variables. The Log-Model is given by:

$$P\left(y = 1|Z\right) = \frac{1}{1 + e^{-z}}, \tag{3.5}$$

where $z = \gamma_0 + \gamma_1 X_1 + \ldots \gamma_n X_n$.

The coefficients $\beta_0, \beta_1, \ldots, \beta_n$ are estimated using Maximum Likelihood Estimation, which finds the parameter values that maximize the likelihood function. The likelihood

function represents the probability of observing the given data under the model.

The analysis of the GLMs, with logistic link functions is conducted using the Python module `statsmodels` (Seabold and Perktold 2010).

3.4.3 Theil-Sen Estimator

The Theil-Sen estimator, also known as the median slope estimator, presents an alternative to the OLS method for linear regression, particularly valued for its robustness to outliers (Sen 1968). Unlike OLS, which minimizes the sum of squared vertical deviations between the observed and predicted values, the Theil-Sen estimator is based on the median of the slopes computed between all pairs of sample points. This approach renders it less sensitive to unusual data points, thus providing a more resilient measure of the central tendency in the presence of non-normal error distributions or outliers.

Mathematically, for a set of observations (x_i, y_i), the slope $\hat{\beta}_1$ is estimated as

$$\hat{\beta}_1 = \text{median}\left(\frac{y_j - y_i}{x_j - x_i}\right), \tag{3.6}$$

for all $i < j$, where $x_j \neq x_i$. The intercept β_0 is then usually calculated as the median of $\{y_i - \hat{\beta}_1 x_i\}$, ensuring consistency with the robust nature of the slope estimation.

3.4.4 Box-Cox Transformation

The Box-Cox transformation (Box and Cox 1964) is a family of power transformations designed to stabilize variance and make data more closely conform to the normal distribution, thereby satisfying key assumptions of linear regression and other parametric statistical models. Given a dependent variable Y and a parameter λ, the Box-Cox transformation is defined as

$$Y^{(\lambda)} = \begin{cases} \frac{Y^\lambda - 1}{\lambda} & \text{if } \lambda \neq 0, \\ \ln(Y) & \text{if } \lambda = 0. \end{cases} \tag{3.7}$$

The optimal value of λ is typically determined through maximum likelihood estimation, seeking to maximize the log-likelihood function under the transformed model.

It should be noted that the Box-Cox transformation is only applicable to positive data. By applying Box-Cox transformations, the issue of not normally distributed residuals is addressed, facilitating a more accurate and efficient estimation of regression coefficients through the OLS.

Moreover, the transformation aids in linearizing the relationships between variables, enhancing the interpretability of linear models.

3.5 Analysis Methods

3.5.1 Temperature profiles and Inversion Parameters

For this analysis, the vertical temperature profiles are created using SPARTACUS minimum temperature data. This has on the one hand the advantage that the data is available for the whole study period from 1961 to 2020 and on the other hand in Hiebl and Schöner (2018) it is shown that the SPARTACUS dataset is able to capture the temperature inversions accurately. Although their study was conducted for the whole of Austria, it makes validation and comparison of the temperature profiles created with SPARTACUS possible. Additionally the use of gridded data for the temperature profiles has the advantage that allocation of model biases on the grid is possible. It should be noted that the actual temperature profiles from the free valley atmosphere can often significantly differ from the one on the slopes (Dreiseitl 1988; Pepin and Norris 2005). The accurate representation of the vertical structure of the atmospheric temperature can only be done using direction free air measurements such as radiosonde data, which are not available for the whole study period. Hence the temperature profiles are referred to as Pseudo Temperature Profiles (PTP) in the following [5].

Using the daily minimum temperature instead of the daily mean has the effect that inversion layers are displayed in a larger number and to greater extend. The vertical profiles are created for the study domain shown in Figure 3.2. The PTP are created using the 2 m temperature daily minimum values from SPARTACUS.

For the PTP, the 2 m temperatures over the orography (see Figure 3.3 (a) blue dots) in the study domain are binned to altitudinal zones of 100 m thickness and then the

[5] In this thesis sometimes the terms PTP and temperature profile are used interchangeable

mean of all data points inside each zone is calculated. The vertical position of this value is located at the center of the according altitude zone. These profiles of 100 m means (see Figure 3.3 (a) orange dots/ lines) are then used to find inversion layers. Only altitude bins consisting of at least 10 grid points are used for the inversion detection (compare with Figure 3.2). Inversion layers are searched using local temperature maxima and minima of these altitude zones means. The minimum thickness (difference in altitude between local maxima and minima) was set to 400 m, which is equal to four altitude bins. This should make the algorithm more robust against fluctuations in the temperature profile and assure that the found inversions layers where likely prominent. An additional constraint for an inversion layer to be detected is that the temperature difference between the local maximum and minimum has to be bigger than the combined standard deviation of the local minima and local maxima grid points. This should avoid detecting inversions in profiles with very low temperature gradients, which are likely not representative. With this temperature profiles the following inversion parameters are calculated (Figure 3.3 (b)):

- **Thickness:** The thickness of the inversion layer is the difference between the altitudes of a local temperature maximum and of the lower-level temperature minimum.
- **Intensity:** The intensity of the inversion is given by the gradient (in K per 100 m) of a linear regression line fitted to the temperature profile within the inversion layer.
- **Magnitude:** The magnitude is the temperature difference produced by the inversion.
- **Frequency:** Inversion days per time period in percent. All days with detected inversions contribute to the frequency.

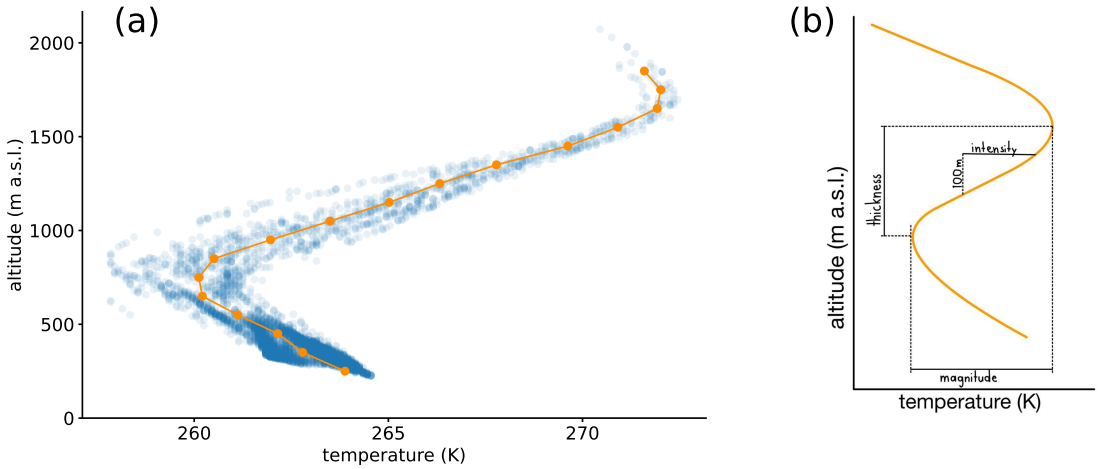


Figure 3.3: (a) Example of a temperature profile with an inversion layer. Blue dots are all grid points of the temperature profile. orange dots are the binned altitude means. The orange line marks the PTP. (b) Definition of inversion parameters: The *thickness* of the inversion layer is the difference between the altitudes of a local temperature maximum and of the lower-level temperature minimum. The *intensity* of the inversion is given by the gradient (in K per 100 m) of a linear regression line fitted to the temperature profile within the inversion layer. The *magnitude* is the temperature difference produced by the inversion. All days with detected inversions contribute to $frequency$.

3.5.2 Classification of Weather Types

In this thesis the classification of the weather types is used to investigate, which weather types favour the occurrence of temperature inversions. For this classification the Jenkinson-Collison weather typing scheme (Jenkinson and Collison 1977) is used. The Jenkinson–Collison weather typing scheme is an automated method used to classify regional sea-level pressure into a reduced number of typical recurrent patterns. Allowing to classify the large scale weather situation into 27 different weather types (Lamb Weather Types (Lamb 1972)), based on direction and vorticity of the flow. The analysis is based on ERA5 daily mean sea-level pressure (SLP) data.

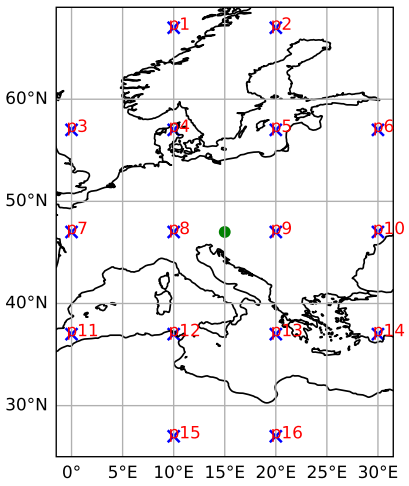


Figure 3.4: The green dot marks the location of interest: Graz. Blue crosses mark the grid points used for the classification of the weather types. The red numbers refer to the SLP grid points p_i used in Equation 3.8 to Equation 3.12

.

The following atmospheric parameters are calculated as described in Fernandez-Granja et al. (2023) with the SLP points shown in Figure 3.4:

$$\text{Westerly flow } W = (p_{12} + p_{13})/2 - (p_4 + p_4)/2 \tag{3.8}$$

$$\text{Southerly flow } S = s \cdot \left(\frac{p_5 + 2p_9 + p_{13}}{4} - \frac{p_4 + 2p_8 + p_{12}}{4}\right) \tag{3.9}$$

$$\text{Resulant flow } F = \sqrt{W^2 + S^2} \tag{3.10}$$

$$\begin{aligned}\text{Westerly shear vorticity } Z_w = z_w^- \cdot \left(\frac{p_{15} + p_{16}}{2} - \frac{p_8 + p_9}{2}\right) \\ - z_w^+ \cdot \left(\frac{p_8 + p_9}{2} - \frac{p_1 + p_2}{2}\right)\end{aligned} \tag{3.11}$$

$$\begin{aligned}\text{Shouterly shear vorticity } Z_s = z_s \cdot \left(\frac{p_6 + 2p_{10} + p_{14}}{4} - \frac{p_5 + 2p_9 + p_{13}}{4}\right. \\ \left. - \frac{p_4 + 2p_8 + p_{12}}{4} + \frac{p_3 + 2p_7 + p_{11}}{4}\right)\end{aligned} \tag{3.12}$$

$$\text{Total shear vorticity (TSV)} Z = Z_w + Z_s \tag{3.13}$$

with $s = \frac{1}{\cos(\psi)}$, $z_w^- = \frac{\sin(\psi)}{\sin(\psi - 5°)}$, $z_w^+ = \frac{\sin(\psi)}{\sin(\psi + 5°)}$ and $z_s = \frac{1}{2\cos^2(\psi)}$, where ψ is the latitude of the location of interest and p_i are the daily mean SLP-values at the grid points shown in Figure 3.4.

The method described in Grimalt-Gelabert et al. (2013) is used to classify the weather situations into Cyclonic C, Anticyclonic A, Hybrid and Advective, based on the criteria:

- Pure directional type (advective): $|Z| < F$
- Cyclonic: $|Z| > 2 \cdot F$
- Anticyclonic: $|Z| > 2 \cdot F$

- Hybrid type: $F < |Z| < 2 \cdot F$
- Undetermined type: $F < 6$ and $|Z| < 6$.

3.5.3 Definition of Inversion Events

For the study of the duration and occurrence of inversion events the following is defined as an inversion event: An inversion event should consist of at least three consecutive inversion days, based on the PTP of subsection 3.5.1. PTP are based on minimal temperatures which usually occur at morning just before the sunrise. For that reason the Total Shear Vorticity (TSV) based on daily mean SLP is included to the inversion event as the first day. For the same reason the last day of an inversion event, the day of the inversion event destruction, is also counted. The weather type on the last day of an inversion event most likely contributes to the destruction of the inversion event. This can give valuable insights on the influence of changes in weather types on the destruction of inversion events. Since this is applied equally to the whole time of the analysis (1961-2020) it does not influence the changes between the climate reference period 1961-1990 and the recent climate period 1991-2020.

For the study of the influence of the weather type on the inversion magnitude, the TSV Equation 3.13 is used as a predictor in a simple linear regression model (Equation 3.1). Both the mean and the maximum TSV of an inversion event, are used to predict mean and maximum magnitude of an inversion event via the linear regression.

Regression Analysis of the Inversion Events

Since periods of long-lasting inversions events are of particular interest, due to their severe impacts on air quality and human health (Jans et al. 2018), their changes over time are analyzed. Inversion events are defined as described in subsection 3.5.3. To analyze the influence of changes in weather types on the occurrence of inversion events, a generalized linear model with a logistic link function as described in subsection 3.4.2 is used. The reason for using a logistic regression model is that, the independent variable is the number of inversion events per month in each climate period (1961-1990 and 1991-2020), which is a positive discrete count of events for each period. In order to model the changes in inversion events, first the inversion events are grouped into the months

of the year and the sum of inversion events per month is calculated for each climate period. The dependent variable is the number of inversion events per month in the recent climate period 1991-2020, $Y_{\text{1991-2020}}$. For the independent variable, the relative change (change between 1961-1990 and 1991-2020) in the number of Anticyclonic weather types per month, A, is used together with the number of inversion events per month in the reference climate period 1961-1990, $Y_{\text{1961-1990}}$. The regression model looks as follows:

$$E(Y_{\text{1991-2020}}) = \mu = g^{-1}\left(\beta_0 \cdot Y_{\text{1991-2020}} + \beta_1 \cdot A\right), \tag{3.14}$$

The link function is the logistic function as described in Equation 3.5, with

$$z = \beta_0 \cdot Y_{\text{1991-2020}} + \beta_1 \cdot A. \tag{3.15}$$

The generalized linear model is then fitted using the Python module `statsmodels` (Seabold and Perktold 2010).

3.5.4 Regression Analyses of Temperature and Sunshine Data

The inversion parameters based on the SPARTACUS PTP as described in subsection 3.5.1 make it possible to separate the temperature data into days with and without inversions. This can be done for atmospheric variables such as: minimum temperature, maximum temperature, and sunshine duration. With possible trends in the inversion parameters, the influence of these changes on temperature and sunshine data can be analyzed. This can not only give insights of the influence of inversion parameters on local atmospheric variables, but also highlight the importance of the inversion parameters for local climate change.

To investigate the influence of temperature inversion parameters on temperature anomalies in station data, a linear regression model is developed as follows: From the time series temperature data from 1961-2020 three different time series are created: (1) The full time series from 1961-2020 denoted as temperature on all days (T_{all}), (2) temperature on days with an inversion (T_{inv}), and (3) temperature on days where no inversion occurred ($T_{\text{non-inv}}$). For every time series T_{i} the seasonal mean ($T_{\text{i, seasonal}}$) is calculated. After that the temperature anomalies are calculated for all three time series using the mean climate reference period 1961-1990.

$$\tilde{T}_{\text{i, seasonal}} = T_{\text{i, seasonal}} - \text{mean}_{1961-1990}(T_{\text{i, seasonal}}), \tag{3.16}$$

with $\text{i} = \text{all}, \text{inv}, \text{non-inv}$. The temperature trend of the whole time series is calculated using a simple linear regression model (Equation 3.1)

$$\tilde{T}_{\text{all, seasonal}} = \alpha_0 + \alpha_1 \cdot \text{time}. \tag{3.17}$$

The trend of the whole time series ($\tilde{T}_{\text{all, seasonal}}$) is then removed from the temperature data of the inversion days (i = inv) and the non-inversion days (i = non-inv)

$$\tilde{T}_{\text{i, detrended}} = T_{\text{i, seasonal}} - \tilde{T}_{\text{all, seasonal}}. \tag{3.18}$$

Since the seasonal mean inversion magnitude M_{seasonal} is not normally distributed, but is all positive, the data is transformed using the Box-Cox transformation described in subsection 3.4.4. With the transformed inversion magnitude the inversion magnitude anomaly $\tilde{M}$ is calculated as the difference between the transformed inversion magnitude

and the associated mean of the climate reference period 1961-1990

$$\tilde{M} = M_{\text{seasonal}} - \text{mean}_{1961-1990}(M_{\text{seasonal}}). \tag{3.19}$$

For the influence on the minimum temperatures, the detrended temperature anomaly on non-inversion days $\tilde{Tn}_{\text{non-inv, detrended}}$ is used as the dependent variable together with the Box-Cox transformed inversion magnitude anomaly $\tilde{M}$ in the regression model

$$\tilde{Tn}_{\text{inv, detrended}} = \beta_0 + \beta_1 \cdot \tilde{M} + \beta_2 \cdot \tilde{Tn}_{\text{non-inv, detrended}} + \eta, \tag{3.20}$$

with the normally distributed residuals of the regression model η. This should give insights on the influence of inversion magnitude on minimum temperatures.

To model of the seasonal maximum temperatures, the same method is used, but additionally the seasonal mean sunshine duration so_h_{seasonal} is added as a predictor.

For modelling the sunshine duration the same method is used as for the temperature data. First the time series of the sunshine duration is created for all days, inversion days and non-inversion days. The seasonal mean $so_h_{\text{i, seasonal}}$ is calculated for all three time series. Since sunshine duration is not normally distributed, but is all positive, the data is transformed via the Box-Cox transformation described in subsection 3.4.4. The sunshine duration anomaly $\tilde{so_h}$ is calculated as the difference between the transformed sunshine duration and the associated mean of the climate reference period 1961-1990

$$\tilde{so_h} = so_h - \text{mean}_{1961-1990}(so_h). \tag{3.21}$$

The influence of the temperature inversions on the trend in sunshine duration is investigated. Therefore the trend of the sunshine duration of all days is calculated using a simple linear regression model (Equation 3.1)

$$\tilde{so_h}_{\text{all, seasonal}} = \gamma_0 + \gamma_1 \cdot \text{time}. \tag{3.22}$$

This trend is afterwards removed from the sunshine duration data of the inversion days (i = inv) and the non-inversion days (i = non-inv)

$$\tilde{so_h}_{\text{i, detrended}} = so_h_{\text{i, seasonal}} - \tilde{so_h}_{\text{all, seasonal}}. \tag{3.23}$$

The regression model looks as follows

$$\tilde{so_h}_{\text{inv, detrended}} = \lambda_0 + \lambda_1 \cdot \tilde{M} + \lambda_2 \cdot \tilde{so_h}_{\text{non-inv, detrended}} + \epsilon, \tag{3.24}$$

with the normally distributed residuals of the regression model ϵ.

3.5.5 Spatial Bias plots and Conservative Remapping

The bias of the regional climate model is defined as

$$T_{\text{Bias}} = T_{\text{Model}} - T_{\text{ref}}, \tag{3.25}$$

where in this case the T_{ref} is the data of SPARTACUS.
In order to match the grids of the reference data SPARTACUS and the rotated pole 3 km×3 km grid from the CCLM simulation, a first order conservative remapping is used. Conservative remapping is a numerical technique used to interpolate data between different grid systems while ensuring the conservation of integral properties such as mass or energy across the grids (Jones 1999).
Climate Data Operators (CDO)[6] are used for remapping the data. Although both datasets are on the same grid after remapping, the individual grid points might still be located at different elevations. Hence an additional bias due to altitude difference of the two datasets may occur. To reduce this effect, the SPARTACUS data is vertically adjusted to the CCLM orography. To estimate the temperature T_c at the height of a certain grid point (x, y) at the height of the CCLM grid h_c, linear interpolation is used to estimate the grid point temperature of SPARTACUS at h_c. For that the temperature difference ΔT between h_c and the grid point height of SPARTACUS h_s, is estimated. This method requires temperatures T_i and T_j at the nearest known heights, h_i and h_j of the vertical temperature profile (subsection 3.5.1) of SPARTACUS, which respectively are the closest heights below and above h_c. The linear interpolated temperature T_c at (x, y) is then calculated as follows

$$T_c = T_s + \frac{(T_j - T_i)(h_c - h_i)}{h_j - h_i} = T_s + \Delta T, \tag{3.26}$$

where T_s is the temperature of SPARTACUS at (x, y).

[6] https://code.mpimet.mpg.de/projects/cdo/wiki

4 Results and Discussion

4.1 Observation Based Analysis - Temperature Inversions in Graz from 1961 to 2021

Prior to the investigation of the representation of subsidence inversion in Regional Climate Models (RCMs), the overall occurrence and other characteristics of temperature inversions in Graz are analyzed. This analysis should not only provide a better understanding of the local climate and enhance the importance of the phenomena itself, it is also used as a validation of the applied methods based on and extending the study by Hiebl and Schöner (2018).

4.1.1 Inversion parameters

To better understand the general occurrence of temperature inversions in Graz, the seasonal cycle of the inversion parameters (Figure 3.3) are shown in the form of boxplots. For that the monthly means from 1961 to 2020 are grouped into the different months of the years.

As expected all four inversion parameter in Figure 4.1 show a clear seasonal cycle, with the highest values in mid-winter and the lowest values in mid-summer. The highest mean monthly inversion frequency is observed in January and December with almost 40 % of the days showing an inversion. The mean inversion magnitude ranges from 4.1 K in January to 1.5 K in July. The overall strongest detected inversion in the Basin of Graz was detected on 15 January 1982 with an inversion magnitude of 16 K. The mean monthly inversion thickness ranges from 800 m in January to 400 m in July. Interestingly the mean monthly inversion thickness is already increased in the autumn months October and November with values of almost 800 m. Considering the seasonality of the inversion parameter, it is concluded that the main inversion season in Graz is from October to February. This is consistent with the results of Hiebl and Schöner (2018) for the whole of Austria.

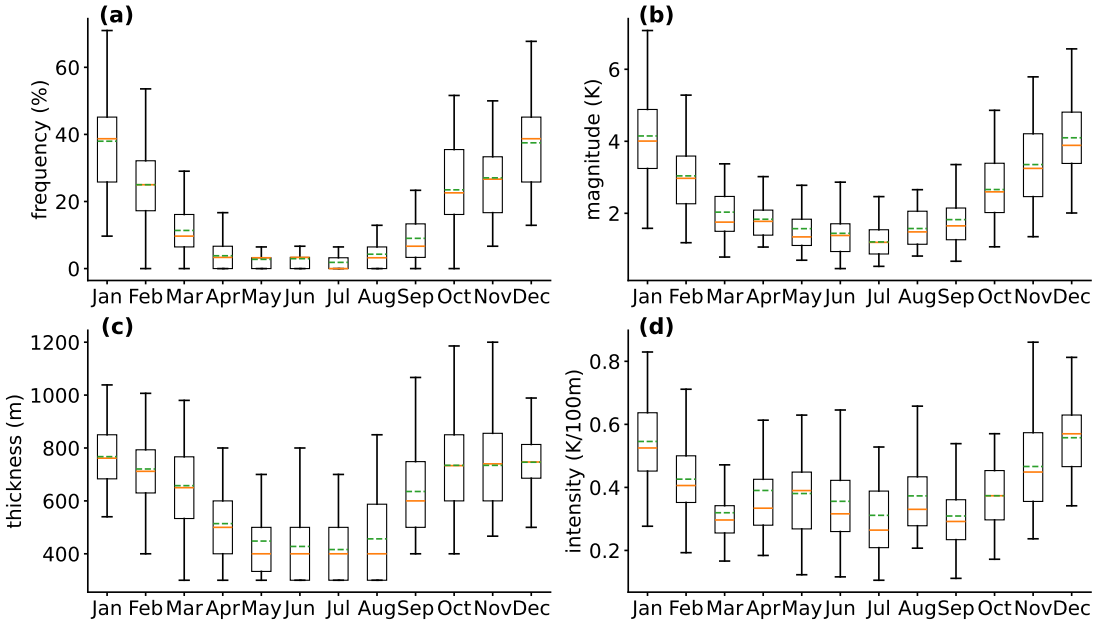


Figure 4.1: Mean seasonal courses of inversion frequency (a), magnitude (b), thickness (c) and intensity (d) in Graz for the period 1961–2020. Boxplots indicate the statistical distribution (median (orange),mean (green), interquartile range, 95 % confidence interval of the median)

In order to get a better understanding of the long-term development of the inversion parameters, the changes of the inversion parameters are investigated over the 60 year period from 1961 to 2020. The results are shown in Table 4.1.

Although not significant in terms of the Mann-Kendall test, still an overall slight decrease in inversion frequency and magnitude can be observed. The inversion frequency shows an overall yearly odds ratio of 0.98, implying a 2 % decrease in the inversion frequency per year. Although in the yearly mean there is not much trend in the inversion frequency, the month of January shows a decrease in inversion frequency of 12 % over the 60 year study period. The inversion magnitude shows an overall yearly reduction of −0.4 K. The strongest decrease over the 60 year period is observed in January with a decrease of −1.2 K. This is probably due to the overall higher values in January. The biggest relative decrease in magnitude is found in July with a significant decrease of −0.6 K (note the overall low values in July Figure 3.3). The thickness of the inversion layers shows a slight increase, while the intensity shows also a slight decrease. It should be mentioned here that, since the maximum height that can be captured by the Pseudo

Table 4.1: Changes of inversion frequency, intensity, magnitude and thickness in Graz during the period 1961–2020. Frequency changes are expressed as odds ratios. Intensity, magnitude and thickness changes are absolute changes over 60 years determined from Theil-Sen linear trend slopes. Trend significance of the area means at the 5 % (1 %) level is denoted by one asterisk (two asterisks).

month	frequency	intensity (K/ 100 m)	magnitude (K)	thickness (m)
Jan	0.88	-0.18**	-1.2	84.0
Feb	1.02	-0.1*	0.1	120.0*
Mar	1.0	-0.0	0.3	127.0
Apr	1.0	-0.16*	-0.0	256.0**
May	1.0	-0.18	-0.4	0.0
Jun	1.0	-0.07	-0.2	0.0
Jul	1.0	-0.13	-0.6*	0.0
Aug	1.0	0.06	-0.0	0.0
Sep	0.96	-0.0	-0.5	-121.0
Oct	0.93	0.04	-0.8	-176.0*
Nov	1.0	-0.12	-1.0	-73.0
Dec	1.0	-0.06	-0.5	18.0
year	0.98	-0.08	-0.39	19.59

Temperature Profiles (PTP) is limited (Figure 3.2), the thickness of the inversion layers might be slightly underestimated on some days, making the changes in the thickness and thus also the intensity parameter less reliable.

For the main inversion season in Graz, which is from October to February, the inversion parameters are compared for the two climate periods 1961-1990 and 1991-2020 in Figure 4.2. A significant decrease in mean inversion frequency (see Figure 4.2 (a)) between the two climate periods is observed in January and October. For the inversion magnitude the decrease is most noteable in October, November and January (see Figure 4.2 (b)). While the thickness of the inversion layers shows a slight increase in January it shows a sudden decrease in October and November as shown in Figure 4.2 (c). The intensity of the inversions show a decrease in the months of January, February and November. The inversion layer bottom (see Figure 4.2 (e)) shows a significant decrease in February (p-value = 0.006, T-test) and a slight decrease in January, with no notable change in November and December. Interestingly the inversion layer bottom shows a huge variance for the recent climate period in October. The inversion layer top (see Figure 4.2 (f)) shows a slight decrease in October, November and December and a slight

increase in January and February. This results should be taken with caution, since the inversion layer top is not always well captured by the PTP.

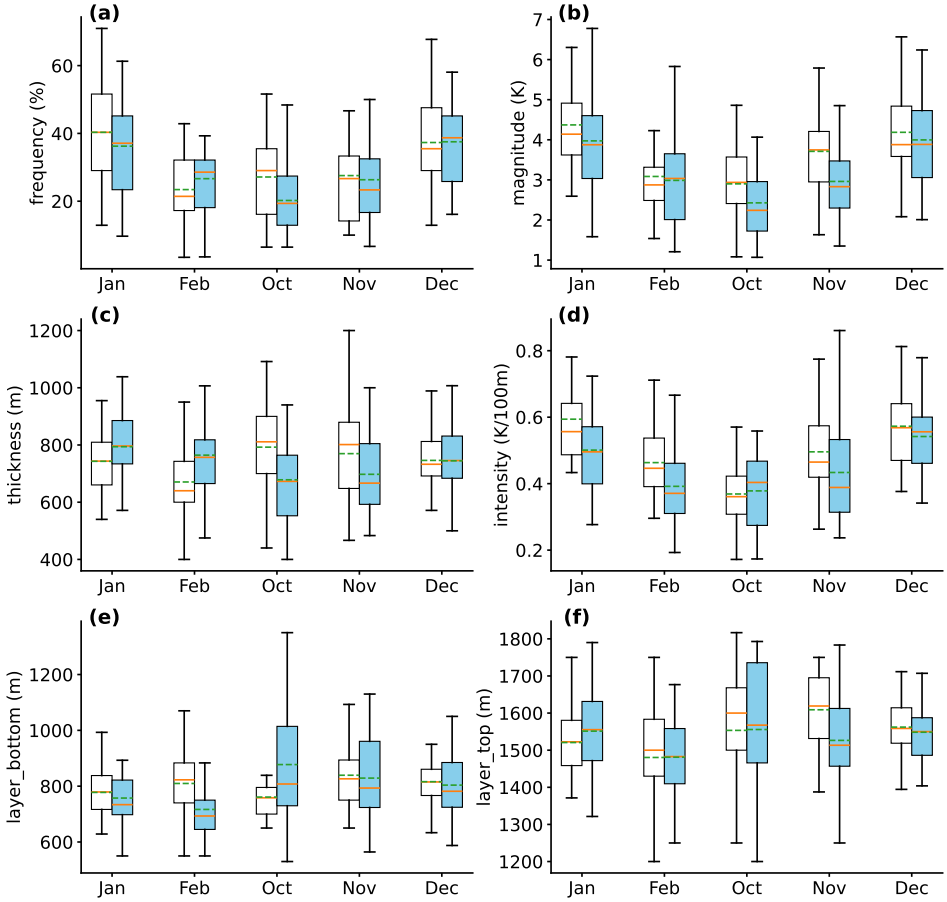


Figure 4.2: Comparison of reference climate period 1961-1990 (white) and 1991-2020 period (blue) of inversion frequency (a), magnitude (b), thickness (c), intensity (d), layer bottom (e) and layer top (f) in Graz. Boxplots indicate the statistical distribution (median (orange),mean (green), interquartile range, 95 % confidence interval of the median)

4.1.2 Inversion Events

Since periods of long-lasting inversions can have a significant impact on the accumulation of air pollutants and the associated health effects (Jans et al. 2018), in the following changes in inversion events between the two climate periods 1961-1990 and 1991-2020 are investigated. For this inversion events are defined as described in subsection 3.5.3.

The average inversion event lasts for about eight days in the climate reference period, with the longest inversion event lasting for 27 days in winter 1989/1990. In the recent climate period, the longest inversion event lasted for over 40 days in winter 2015/2016.

When comparing the average duration lengths of the two climate periods (Figure 4.3 (a)) there is no significant change ($p = 0.63$ according to the Mann-Whitney U test). With an average duration of 8.3 days for the reference climate period and 9.7 days for the recent climate period. On the other hand when looking at the total number of inversion events (Figure 4.3 (b)), a strong decrease from 120 inversion events in the reference climate period (1961-1990) to 93 inversion events in the recent climate period (1991-2020) can be observed. In Figure 4.3 (c) the total number of inversion events for the individual months of the year is shown. It can be seen that the biggest decrease in the total number of inversion events is observed in the months of October and November. This is also in line with the results shown in Figure 4.2 (a), where the inversion frequency shows a significant decrease in January and October. It should be noted at this point that the results from Table 4.1 and Figure 4.2 should not be confused with the results shown in Figure 4.3 (c). Since in Table 4.1 and Figure 4.2 the trends are calculated for all inversion days, while in Figure 4.3 (c) only inversion events are counted. At some point a strong decrease in Table 4.1 can be an indicator for a decrease in inversion events, but it is not necessarily the case. It could also be that the inversion days stay similar in terms of frequency, but the inversion events are shorter. Although Figure 4.3 (a) shows no significant change in the average duration of inversion events, this has not necessarily to be the case for the individual months.

Although the month of September has an overall low number of inversion events, it shows a decrease of 75 % in the recent climate period. The month of March shows the strongest increase in the total number of inversion events with an increase of 500 %.

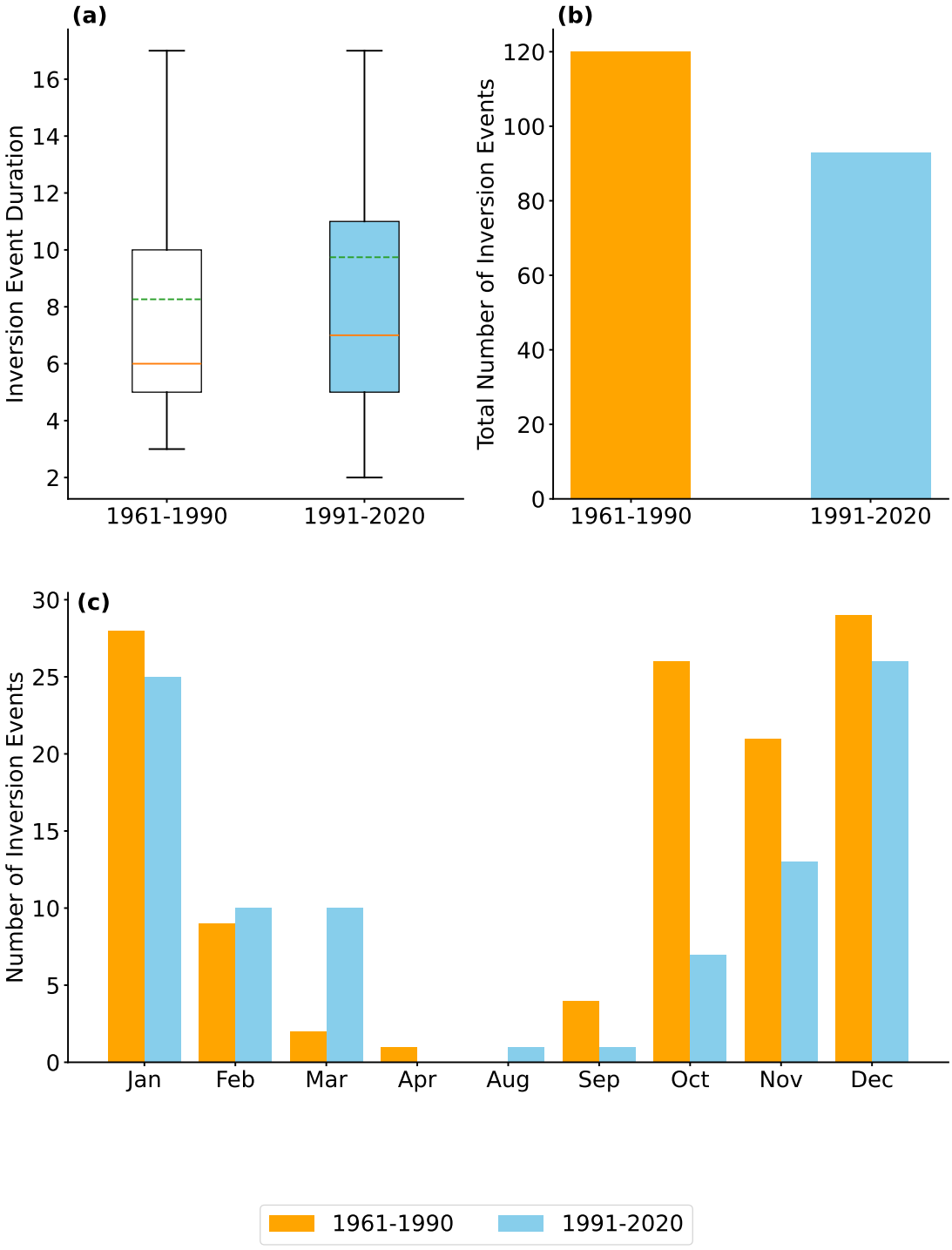


Figure 4.3: (a) Comparison of the inversion event duration, defined as periods with at least three consecutive days with detected inversions, in Graz of the periods 1961–1990 and 1991–2020. Boxplots indicate the statistical distribution (median (orange),mean (green), interquartile range, 95 % confidence interval of the median) (b) Total number of inversion events in Graz of the periods 1961–1990 and 1991–2020. (c) Total number of inversion events for the individual months of the year for the periods 1961–1990 (orange) and 1991–2020 (blue). Months with no inversion events are not shown.

The presence of large scale weather types, such as long lasting Anticyclonic conditions, can have a significant impact on the persistence of temperature inversions (Wei et al. 2013). To see if the changes in the number of inversion events in the Basin of Graz can be attributed to changes in the synoptic weather situation, first the weather types are classified as described in subsection 3.5.2. The results of the amount of certain weather types during inversion events and the termination of inversion events are shown in for both climate periods in Table 4.2.

As expected the most common weather type on inversion days during an inversion event, is the Anticyclonic condition with almost 50 % of all inversion days. The second most common weather type is the pure directional (advective) weather type. Additionally the strongest inversion events, with an average magnitude of 5.1 K, are associated with the Anticyclonic weather type. It should be noted that the average inversion magnitude can only be compared relative between the different weather types, since the day before the inversion event does reduce the average inversion magnitude. Since the inversions are detected using the daily minimum temperatures, which usually occur at night, the day of the termination of an inversion event is still counted as an inversion day. Hence the inversion event ending day, can give an insight on how often an inversion event is terminated by a specific weather type. The most common weather type for the termination of an inversion is the Cyclonic weather condition. It seems that in the recent climate period from 1991 to 2020, the termination of an inversion event is more often associated with advection of air masses. The direction is not investigated in this work, but the method presented in subsection 3.5.2 can be used to investigate this further. Leading to the conclusion that the termination of an inversion event is often associated with a change in the weather pattern, from Anticyclonic to Cyclonic conditions or by advection from air masses. The findings of the weather type on temperature inversions are consistent with the results of Li et al. (2015) and Kassomenos et al. (2014). The found decrease in the total number of inversion events between the two climate periods (Figure 4.3(b)) and the large presence of the Anticyclonic weather type on inversion days, as well as the Cyclonic weather type on the termination of inversion events, might be an indication of a change in the synoptic weather situation over the last 60 years.

Table 4.2: Inversion characteristics for different weather types in Graz during the period 1961-1990 and 1991-2020. Values for the period 1991-2020 are shown in round brackets.
WT: weather type; NoD: number of days in percent of the total number of inversion event days; Mean Mag.: mean magnitude of the inversion (K); Std. Mag.: standard deviation of the magnitude of the inversion (K); IED: inversion event ending days (%).

WT	NoD (%)	Mean Mag. (K)	Std. Mag. (K)	IED (%)
Cyclonic	2.6 (2.1)	3.0 (3.1)	2.0 (2.2)	31.8 (20.0)
Anticyclonic	46.9 (45.7)	5.1 (5.1)	2.9 (2.9)	5.0 (3.6)
Hybrid	23.3 (27.7)	4.6 (4.5)	2.6 (2.6)	11.2 (9.5)
Advective	27.3 (24.5)	3.8 (3.5)	2.1 (2.2)	19.9 (23.0)

To investigate this further, the weather types are grouped into the months for the periods 1961–1990 and 1991–2020 and the fractions of the weather types are shown in Figure 4.4. The results indicate a slight decrease in the Anticyclonic weather type, especially for the months from September to November. Additionally the fractions of the Cyclonic weather type, responsible for many terminations of inversion events, show a slight increase from August to November. These results can be an indication of a slight change in the synoptic weather situation, which might result in the decrease in the total number of inversion events over the last 60 years shown in Figure 4.3 (b). Since the overall proportion of the weather types is often very low, the relative changes in the weather types between the two climate periods are shown in Figure 4.4 (b). The relative changes are defined by the difference in the fractions of the weather types between the two climate periods in percent. When looking at the Anticyclonic weather type, the biggest relative decrease is observed in the months of September to November, whereas the a relative increase from February to April is observed. The Cyclonic weather type shows a relative decrease in January to May and a relative increase in the months from July to December. The opposing relative changes in the Anticyclonic and the Cyclonic weather types in the months from September to November, might give a possible explanation for the decrease in the total number of inversion events in the recent climate period (see Figure 4.3 (c)). Because the Advective weather type is responsible for both persistence and termination of inversion events (see Table 4.2), the relative changes can not give a clear indication of the explainable changes in the total number of inversion events over the last 60 years.

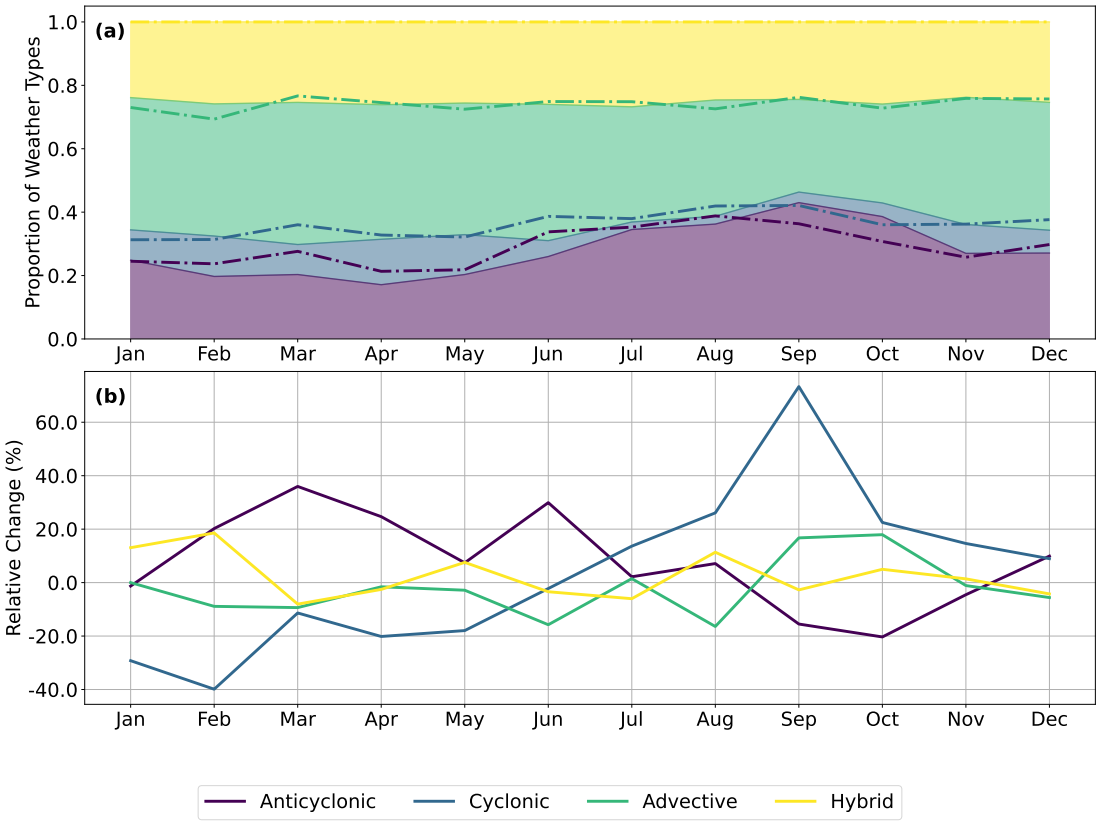


Figure 4.4: (a) Weather types fractions grouped into the months for the periods 1961–1990 and 1991–2020. The colored areas show the period from 1961 to 1990.
The dashed lines show the period from 1991 to 2020.
(b) Shows the relative changes between the two climate periods. Positive values denote an increase and negative values denote a drecrease in inversion events relative to the period from 1961 to 1990.

With the change in the weather types and the mentioned biases in the midlatitude blocking and the associated atmospheric circulation patterns in RCMs (Maraun et al. 2021; Jury et al. 2019), this might be a potential source of bias for temperature inversion changes in future climate projections. If the changes in inversion events can be attributed to changes in the synoptic weather situation and the correct representation of the synoptic weather situation in RCMs is crucial for the correct representation of temperature inversions as shown in Table 4.2 and many other studies (Li et al. 2015; Kassomenos et al. 2014), another potential source of bias of temperature inversions in RCMs might be the representation of the wrongly simulated weather types. To investigate the influence of the Anticyclonic weather type on the total number of inversion events, a regression model is conducted as described in subsubsection 3.5.3. In Figure 4.5 the results of the regression model are shown. Figure Figure 4.5 (a) shows the number of inversion events for every month as already shown in Figure 4.3 (c). The model should just be used to see if the changes in the Anticyclonic weather type A have a significant influence on the total number of inversion events. As the model is based on a low number of data points, the results should be taken with caution. But still this is considered more meaningful than just looking at the correlation of the relative changes in the weather types and the inversion events. The model is able to give the total number of inversion events for the recent climate period. It is also able to show the strong reduction in the number of inversion events in the months from September to November, which is consistent with the presumption based on the results shown in Figure 4.4 (b).

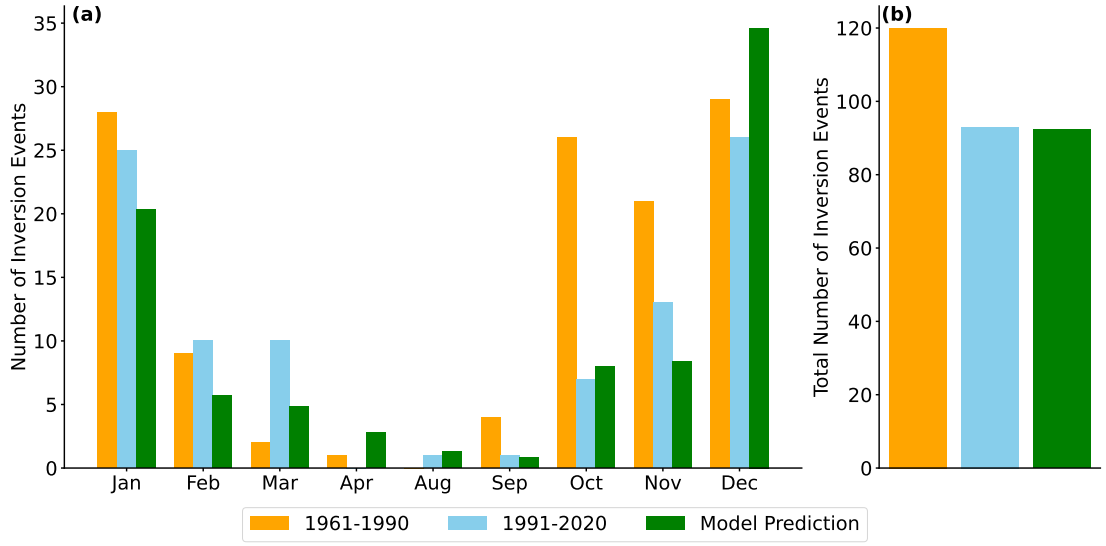


Figure 4.5: Regression Analysis of Weather Type Changes. A generalized linear model, with a logistic link function, is used to predict the number of inversion events per month $Y_{\text{1961-1990}}$, based on the number of inversion events per month $Y_{\text{1961-1990}}$ and the relative changes in the Anticyclonic weather type A. (a) Show bar plots of number of inversion events for every month for the climate reference period (orange), the recent climate period (blue) and the model prediction of the recent climate period (green).
(b) Shows the total number of inversion events for the climate reference period (orange), the recent climate period (blue). Compare with Figure 4.3

The model is able to explain almost 99 % of the variance in the number of inversion events for the climate reference period. This is probability partly attributed to the low number of data points. Nevertheless the model summary suggests that the predictors have a significant effect on the number of inversion events. This result shows that the changes in the Anticyclonic weather type have a significant influence on the total number of inversion events. This confirms the suppositions based on the results of Figure 4.3 (c) and Figure 4.4 (b). All the other weather types, which are not included in the model, are not significant predictors for the number of inversion events. The model parameter and the model summary is shown in Table 4.3.

Table 4.3: Model Summary for $Y_{1991\text{-}2020}$ from the regression model as described in 3.5.3. The model summary is based on the output from the `statsmodels` Python package.

Dep. Variable:	$Y_{1991\text{-}2020}$	**No. Observations:**	12
Model:	GLM	**Link Function:**	Log
Model Family:	Poisson	**Pseudo R-squ. (CS):**	0.99

	coef	**std err**	**z**	**P> |z|**
$Y_{\mathbf{1961\text{-}1990}}$	0.110	0.004	25.177	0.001
A	0.039	0.007	5.308	0.001

To investigate the influence of the most common weather type associated with inversions, which is the Anticyclonic weather type-defined as having a high negative TSV, the TSV is compared to the inversion magnitude of inversion events. For that the mean and the maximum TSV of the inversion events are compared to the mean and maximum inversion magnitude of the inversion events. The results are shown in Figure 4.6 (a). Both show a weak negative correlation, showing the that there is a slight increase in inversion magnitude with decreasing TSV. But it also shows that the TSV alone, is not a good predictor for the inversion magnitude, which emphasizes the local character of the inversion phenomena. In Figure 4.6 (b) and (c) the boxplots show the mean and maximum inversion magnitude of the inversion events with the lowest 50 % and highest 50 % of TSV. The results show that the inversion magnitude is slightly higher for inversion events with lower TSV. Both the mean and the maximum inversion magnitude show a significant difference between the two groups ($p < 0.01$ according to the Mann-Whitney U test).

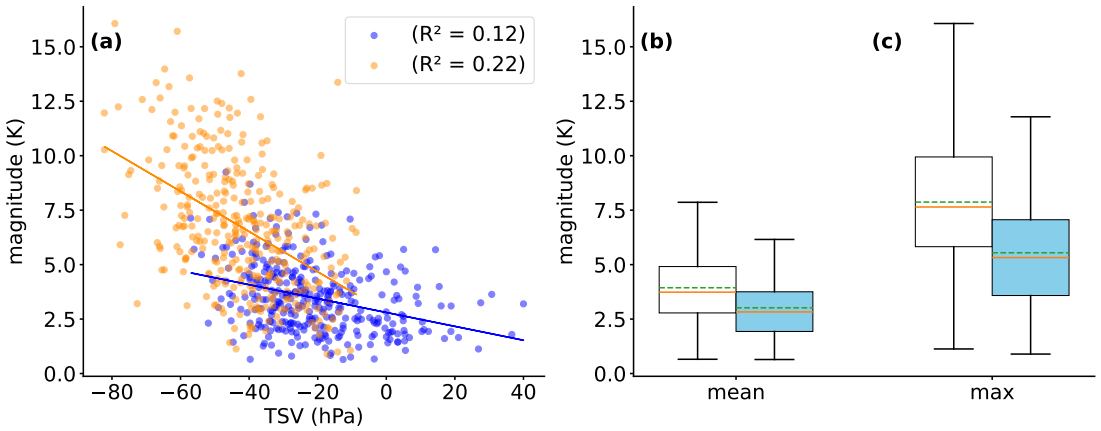


Figure 4.6: (a) Correlation of the Total Shear Vorticity (TSV) and inversion magnitude of inversion events. Mean (blue) and maximum (orange) of TSV and mean and maximum inversion magnitude of inversion events of at least three days.
(b) Boxplot of the mean inversion magnitude of inversion events with TSV. Lowest 50 % (blue) and highest 50 % (white).
(c) Boxplot of the maximum inversion magnitude of inversion events with maximum TSV. Lowest 50 % (blue) and highest 50 % (white).

4.1.3 Modelling Temperature Station Data

The method for the regression model is described in subsection 3.5.4. With the ability to detect inversions accurately, it is possible to look at station data temperature trends for days with inversions and days without inversions separately. For this the temperature data of the station Graz University is used. Although it was found in subsection 4.1.1 that the main inversion season in the Basin of Graz lasts from October until February, the following analysis is only conducted for the winter months December, January and February. This is only done to stay consistent with the analysis of most climate studies, which usually focus on individual seasons, where winter is defined as December, January and February (DJF). The overall result of the analysis should not be affected by this decision.

In Figure 4.7 (a) the daily minimum temperature anomalies for all days, days without inversions and days with inversions are shown, with their trend calculated as described in subsection 3.5.4.

It can be seen that the trend of the detrended temperature anomaly on non-inversion days ($\tilde{Tn}_{\text{non-inv, detrended}}$, black dashed line) is close to zero, which means that it's similar to the trend of all days. The trend of the inversion days ($\tilde{Tn}_{\text{inv, detrended}}$, blue dashed line) in contrast is slightly stronger, with additional 0.1 K per decade. Inversion days show an overall additional warming of 0.55 K over the whole 60 year period from 1961 to 2020. To see if this additional trend in the temperature data can be explained by temperature inversions, a regression model is conducted as described in subsection 3.5.4. The linear regression model for the minimum temperature anomalies is based on the inversion magnitude and the minimum temperature on non-inversion days. The results of the regression model are shown in Figure 4.7 (b).

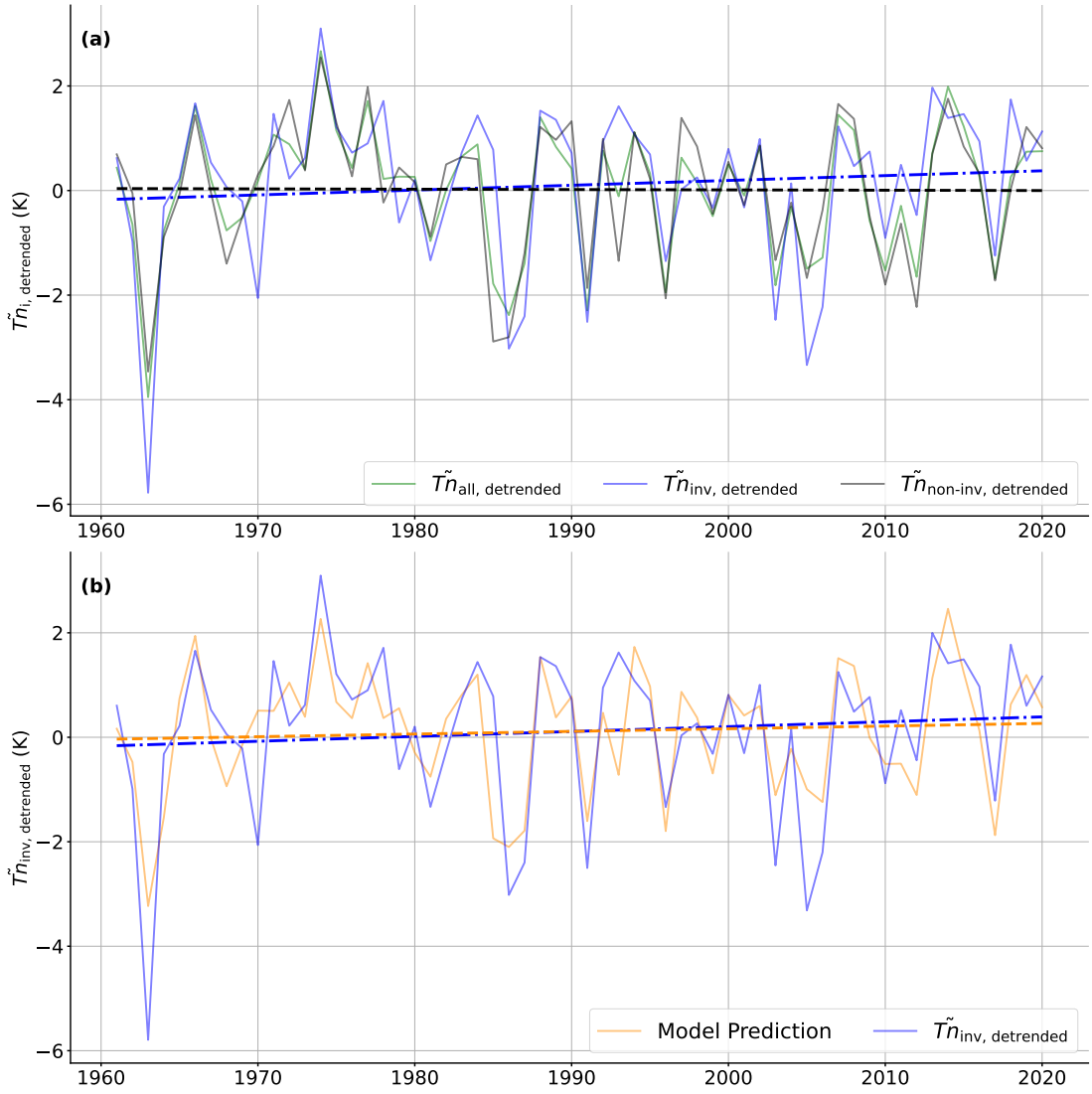


Figure 4.7: Seasonal minimum temperature anomaly at station Graz University (Tn) for all days (green), days without inversions (black) and days with inversions (blue) for DJF from 1961-2020. The trend of the temperature anomalies of all days is removed from the data. The linear regression model is based on the predictors: Inversion magnitude anomaly ($\tilde{M}$), detrended minimum temperature anomaly on non-inversion days ($\tilde{Tn}_{\text{non-inv, detrended}}$).
(a) Mean DJF minimum temperature anomaly for: all days (green), non-inversion days (blue) and inversion days (black). The blue dashed line shows the trend of $\tilde{Tn}_{\text{non-inv, detrended}}$ and black dashed line shows the trend of $\tilde{Tn}_{\text{inv, detrended}}$. (b) Detrended Temperature anomalies ($\tilde{Tn}_{\text{inv, detrended}}$) (blue) and the model data (orange).

The model is able to explain almost 59 % of the variance in the temperature anomalies of the inversion days and also shows the increased trend. The model's overall significance is strong with an F-statistic of 40.35 and a p-value of 1.2×10^{-11}, confirming that the model predictors collectively have a statistically significant effect on the temperature during inversion conditions. With an expected negative coefficient for the inversion magnitude of -0.66 (p-value < 0.01) and a positive coefficient for the minimum temperature on non-inversion days of 0.8 (p-value < 0.01). The model diagnostics suggest that the predictors are not highly collinear, with variance inflation factors (VIFs) ranging from 1.02 to 1.17 for the predictors, which indicates a minimal risk of multicollinearity. Based on the skewness and the kurtosis of the residuals, the Jarque Bera test shows that the residuals are normally distributed. Although from visually inspecting the residuals, it can be seen that the residuals are deviating from the normal distribution, at both ends of the distribution. The model parameter and the model summary is shown in Table 4.4.

Table 4.4: Model Summary for Tn. The regression model is described in 3.5.4. The model summary is based on the output from the `statsmodels` Python package.

Table 4.5: Model Summary for Tn

Dep. Variable:	$\tilde{Tn}_{\text{inv, detrended}}$	**R-squared:**	0.586
Model:	OLS	**Adj. R-squared:**	0.572
Cond. Nr.	22.6	**F-statistic:**	40.35
AIC:	174.4	**Prob (F-statistic):**	1.21e-11
BIC:	180.8	**Log-Likelihood:**	-84.242
Jarque-Bera (JB):	2.948	**Prob(JB):**	0.289

	coef	**std err**	**t**	**P> |t|**	VIF
const	2.600	0.720	3.610	0.001	-
$\tilde{M}$	-0.663	0.188	-3.533	0.001	1
$\tilde{Tn}_{\textbf{non-inv, detrended}}$	0.797	0.100	7.988	0.000	1

Since not only minimum temperature can be affected by temperature inversions, a similar analysis is also conducted for the season maximum temperature of Graz University. Before that, the temporal trend of the seasonal averaged DJF maximum temperature data for the station Graz University is analyzed for the period 1961-2020. In Figure 4.8 (a) the detrended temperature anomalies for all days, days without inversions and days with

inversions, as described in subsection 3.5.4, are shown. It can be seen that the trend of the detrended temperature anomaly on non-inversion days ($\tilde{Tx}_{\text{non-inv, detrended}}$, black dashed line) is slightly negative, which. In contrast the trend of the maximum temperature data on inversion days in the winter months ($\tilde{Tx}_{\text{inv, detrended}}$, blue dashed line), shows a stronger trend than the trend of all days and the trend of the non-inversion days. With an additional 0.2 K per decade. This gives an overall additional warming of 1.2 K over the whole 60 year period from 1961 to 2020. To see if this additional trend in the temperature data can be explained by temperature inversions, a regression model is conducted as described in subsection 3.5.4. It was found that inversion magnitude anomaly, is a significant predictor for the maximum temperature anomalies of the inversion days. In addition the seasonal mean sunshine duration is used as a predictor, since it is known that the sunshine duration has increased in Graz over the last 60 years (Figure 4.9). To get the overall mean winter maximum temperature for each year, the detrended temperature anomaly on non-inversion days is added as a predictor.

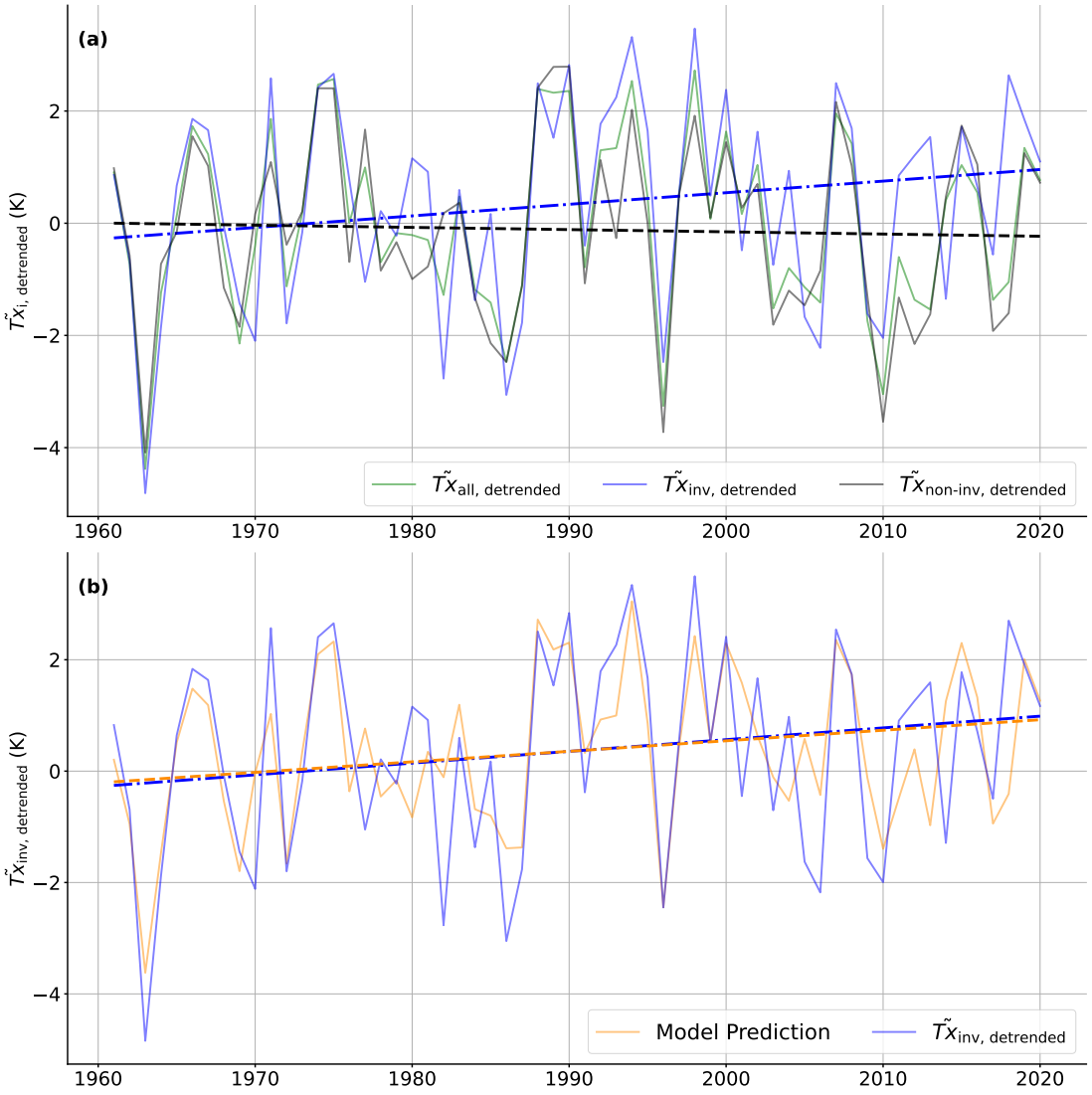


Figure 4.8: Seasonal maximum temperature at station Graz University (Tx) for all days (green), days without inversions (black) and days with inversions (blue) for DJF from 1961-2020. The trend of the temperature anomalies of all days is removed from the data. The linear regression model is based on the predictors: Inversion magnitude anomaly ($\tilde{M}$), detrended minimum temperature anomaly on non-inversion days ($\tilde{Tx}_{\text{non-inv, detrended}}$) and sunshine duration so_h.
(a) Mean DJF maximum temperature anomaly for: days (green), non-inversion days (blue) and inversion days (black). The blue dashed line shows the trend of $\tilde{Tx}_{\text{non-inv, detrended}}$ and black dashed line shows the trend of $\tilde{Tx}_{\text{inv, detrended}}$. (b) Detrended Temperature anomalies ($\tilde{Tx}_{\text{inv, detrended}}$) (blue) and the model data (orange).

The results of the regression model are shown in Figure 4.8 (b). The model is able to explain 59 % of the variance, as indicated by the R-squared value, in the temperature anomalies of the inversion days and it gets the trend of the inversion days. The model's overall fit is strong with an F-statistic of 27 and a p-value of 5.9×10^{-11}, confirming that the model predictors collectively have a statistically significant effect on the temperature during inversion conditions. The model has an expected negative coefficient for the inversion magnitude of -0.68 (p-value < 0.01) and a positive coefficient for the maximum temperature on non-inversion days of 0.64 (p-value < 0.01). The statistic significant contribution of the sunshine duration is also shown with a coefficient of 0.71 (p-value < 0.01), highlighting the importance of the sunshine duration for the maximum temperature anomalies. With a variance inflation factor (VIF) close to 1 for both predictors, the model diagnostics suggest that the predictors are not highly collinear, which indicates a minimal risk of multicollinearity. Based on the skewness and the kurtosis of the residuals, the Jarque Bera test shows that the residuals are normally distributed. Although from visually inspecting the residuals, it can be seen that the residuals are deviating from the normal distribution, at both ends of the distribution. The model parameter and the model summary is shown in Table 4.6.

Table 4.6: Model Summary for Tx. The regression model is described in 3.5.4. The model summary is based on the output from the `statsmodels` Python package.

Dep. Variable:	$\tilde{Tx}_{\text{inv, detrended}}$	**R-squared:**	0.591
Model:	OLS	**Adj. R-squared:**	0.570
Cond. No.	34.1	**F-statistic:**	27.03
AIC:	195.6	**Prob (F-statistic):**	5.90e-11
BIC:	203.9	**Log-Likelihood:**	-93.744
Jarque-Bera (JB):	0.489	**Prob(JB):**	0.783

	coef	**std err**	**t**	**P> |t|**	**VIF**
const	0.732	1.014	0.722	0.473	-
$\tilde{M}$	-0.675	0.224	-3.015	0.004	1.02
$\tilde{Tx}_{\textbf{non-inv, detrended}}$	0.642	0.100	6.447	0.000	1.14
so_h	0.710	0.211	3.356	0.001	1.17

These findings highlight the importance of inversion magnitude and sunshine duration for the maximum temperature anomalies in Graz during the winter months.

4.1.4 Sunshine Duration

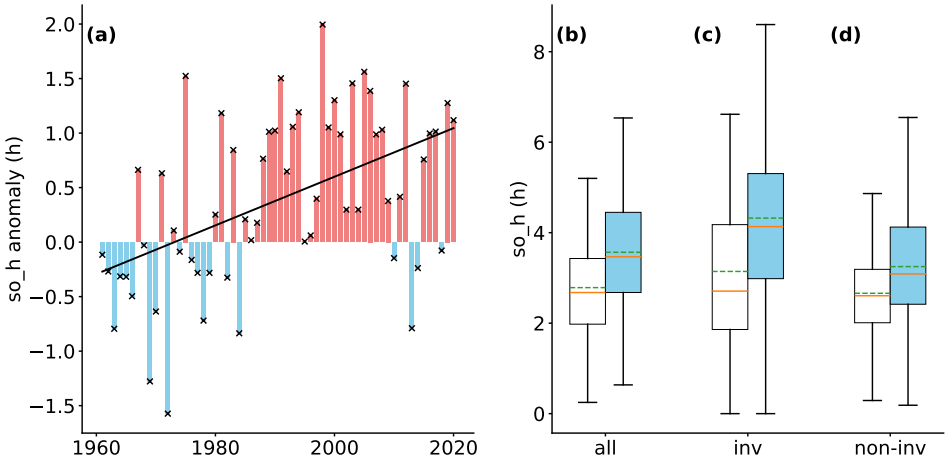


Figure 4.9: (a) DJF sunshine duration anomaly at station Graz University marked in black. Blue bars mark years with below average (climate reference period 1961-1990) and red bars mark above average years. The black line give the linear regression estimate.
Boxplots indicate the statistical distribution (median (orange),mean (green), interquartile range, 95 % confidence interval of the median), for the period 1961-1990 (white) and 1991-2020 (blue). DJF sunshine durations for (b) all days, (c) inversion days and (d) days without an inversion.

In Figure 4.9 (a) the seasonal sunshine duration anomaly at station Graz University is shown. The sunshine duration strongly increased over the last 60 years with a trend of $0.22\,\mathrm{h\,d^{-1}}$ per decade. The sunshine duration on inversion days (mean $so_h = 6.7\,\mathrm{h\,d^{-1}}$) is on average $2\,\mathrm{h\,d^{-1}}$ higher than on non-inversion days. Since inversions are often associated with clear sky conditions and many inversions terminate during the day, this is not surprising.

The sunshine duration is also compared for the two climate periods 1961-1990 and 1991-2020. There is no significant change in the mean in the sunshine duration for all days compared to the sunshine duration on non-inversion days ($p = 0.2$). But there is a change in the mean between the all days and the inversion days as well as for the difference in mean between the inversion days and the non-inversion days ($p < 0.01$). Additionally there is a change in mean for all three groups between the two climate

periods ($p < 0.01$), which can also be seen in the trend of the sunshine duration over the last 60 years in Figure 4.9 (a).

To see the influence of inversions on the sunshine duration, the sunshine duration anomalies are analyzed for the winter from 1961 to 2020, for station data of the University of Graz. The timeseries is split into all days, days with inversions and days without inversions. Again the trend of all days is removed from the data as described in subsection 3.5.4. As shown in Figure 4.10 (a) the trend of the sunshine duration anomalies on non-inversion days (black dashed line) is decreasing, whereas the trend of the inversion days (blue dashed line) is increasing. To see if changes in the sunshine duration anomalies on inversion days can be explained by the sunshine duration anomalies on non-inversion days and the inversion magnitude, a regression model is conducted as described in subsection 3.5.4.

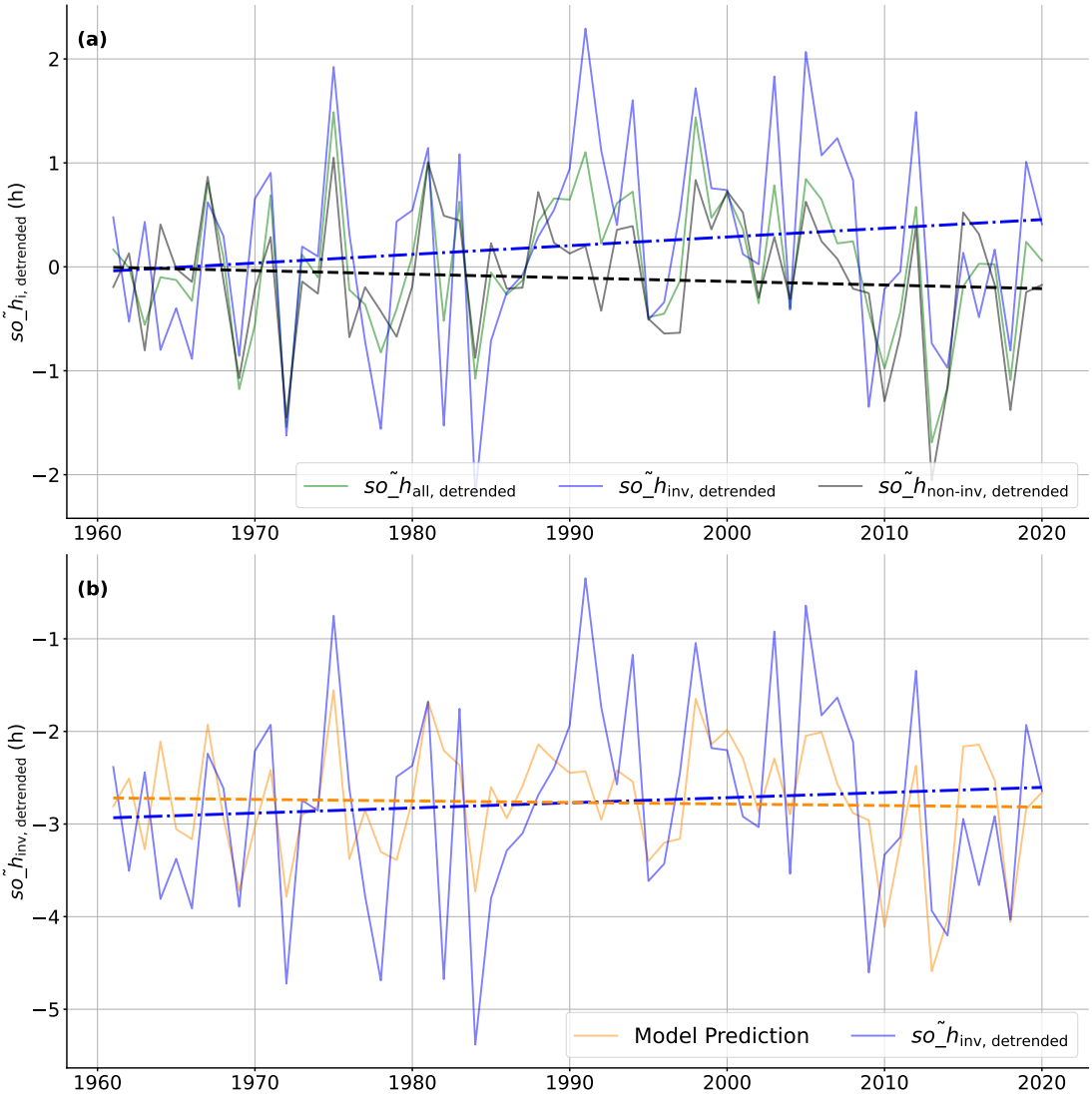


Figure 4.10: Seasonal sunshine duration at station Graz University (so_h) for inversion days in DJF from 1961-2020. The linear regression model is based on the predictors: Sunshine duration in non-inversion days ($so\tilde{_}h_{\text{non-inv, detrended}}$) and inversion magnitude anomaly ($\tilde{M}$). Note the different y-axis scales because of the Box-Cox transformation.
(a) Detrended sunshine anomalies ($so\tilde{_}h_{\text{detrended}}$). All DJF days (green), non-inversion days (black) and inversion days (blue). The trends of the data a marked by the dashed lines.
(b) Sunshine Anomaly with removed trend from days with inversions (blue) and the model data (orange).

The model is able to explain 33.8 % of the variance, indicated by the R-squared value, in the sunshine duration anomalies of the inversion days and is not able to explain the full differences in the trends in the sunshine duration anomalies between the inversion days and the non-inversion days. Although the model is still able to get an overall positive trend in the sunshine duration anomalies of inversion days, with the predictor ($\tilde{so_h}_{\text{no-inv, detrended}}$) having a negative trend. With the inversion magnitude having a negative coefficient of -0.77 and a p-value $= 0.2$, indicating that the inversion magnitude does not have a significant effect on the sunshine duration anomalies. Based on the skewness and the kurtosis of the residuals, the Jarque Bera test shows that the residuals are normally distributed. Although from visually inspecting the residuals, it can be seen that the residuals are deviating from the normal distribution, at both ends of the distribution. The model parameter and the model summary is shown in Table 4.7.

Table 4.7: Model Summary for *so_h*. The regression model is described in 3.5.4. The model summary is based on the output from the `statsmodels` Python package.

Dep. Variable:	$\tilde{so_h}_{\text{inv, detrended}}$	**R-squared:**	0.338
Model:	OLS	**Adj. R-squared:**	0.315
Cond. Nr.	30.3	**F-statistic:**	14.57
AIC:	162.5	**Prob (F-statistic):**	7.76e-06
BIC:	168.8	**Log-Likelihood:**	-78.271
Jarque-Bera (JB):	1.188	**Prob(JB):**	0.553

	coef	**std err**	**t**	**P> |t|**	VIF
const	-2.217	0.942	-2.352	0.022	-
$\tilde{so_h}_{\textbf{non-inv, detrended}}$	0.124	4.917	0.000	0.000	1.03
$\tilde{M}$	0.77	0.598	1.301	0.199	1.03

Although an overall increase in sunshine duration in Austria is known (Olefs et al. 2021; Dobesch 1992; Hadzimustafic et al. 2013), the results show that part of the increasing sunshine durations in the Basin of Graz can be attributed to changes in the inversion magnitude. The result of the overall stronger trend in the sunshine duration on inversion days, compared to the trend of the sunshine duration on non-inversion days, gives some speculations: It was shown that the inversion magnitude anomaly can explain part of the trend difference. Since inversions are often associated with clear sky conditions, the increased sunshine duration on inversion days would mean that the cloud cover on inversion days has decreased over the last 60 years. Some possible explanations

for this are: Decreasing inversion magnitude allow for easier termination of inversions, hence the cloud cover resulting from the inversion is removed earlier in the day. Another possibility could be the influence of aerosols, especially particulate matter on the cloud cover. Temperature inversion layers act as a cap, trapping particulate matter close to the ground, which increases their concentration. The lower the inversion layer, the greater the capacity for particulate matter accumulation (Yang et al. 2016). Additionally particulate matter can act as cloud condensation nuclei (first indirect aerosol effect (Twomey 1974)), which can lead to an increase in cloud cover additional the accumulation of aerosols can increase the albedo of the clouds (direct aerosol effect (Charlson et al. 1992)), which can lead to a decrease in the direct solar radiation reaching the surface (Yang et al. 2016; Forkel et al. 2012). While the effect of temperature inversions on the accumulation of particulate matter is well studied for the city of Graz (Hörmann et al. 2005), the effect of particulate matter on the persistence of temperature inversions in Graz is not found in the literature. Behrens et al. (2018) highlights the downward trend in particulate matter concentrations in Graz from 2002 to 2016. This downward trend, beginning from the early 2000s, could possibly be attributed to the beginning of consistent air quality monitoring in Graz, starting in 2003 on behalf of the `Umweltamt Graz` and associated measures to reduce particulate matter emissions.

This downward trend in aerosols can be enhanced by the overall decreasing trend in temperature inversions (see Figure 4.2) and especially the reduction in the number of inversion events (see Figure 4.3), which would reduce the accumulation in the Basin of Graz. This can lead to a decrease in the cloud cover and an increase in the direct solar radiation, which would lead to earlier termination of inversions, hence the increased sunshine duration on inversion days.

4.2 Inversion Event 2009

4.2.1 Synoptic Conditions

January 2009 started with very cold temperatures in the first half throughout Austria, with temperatures becoming milder from January 15 onward, when a low-pressure system from the south brought precipitation to western and eastern Styria [1]. The event under

[1] https://www.zamg.ac.at/fix/klima/wiewars01-09.pdf

investigation is a subsidence inversion event that occurred in the first half of January 2009. It commenced during the night from January 9 to January 10 and persisted until January 15. The event reached its maximum inversion magnitude on January 12 and was characterized by a strong high-pressure influence over Austria, resulting in a pronounced subsidence inversion.

On January 10, 2009, the weather map (see Figure 4.11(a)) illustrates a high-pressure system centered over Western Europe, with Austria under its influence. The widely spaced isobars indicate weak winds and stable conditions.

By January 11, 2009 (see Figure 4.11(b)), the high-pressure system remained dominant, with its center shifting slightly eastward. Austria continued to experience stable weather with little change in the overall synoptic pattern.

On January 12, 2009, at 06 UTC (see Figure 4.11(c)), the high-pressure influence reached its maximum values, with the center now slightly eastward of Austria with values of 1040 hPa. Directly over the eastern part of Austria, where the study domain of the Basin of Graz is located, the pressure map shows values of 1030 hPa. The isobars over Austria were broadly spaced, indicating light winds and stable atmospheric conditions.

As the high pressure system moves further eastward, a low-pressure system started to develop over the southwestern parts of Europe on January 13 (Figure 2.5 (d)). This system began to influence the weather in Austria, increasing the pressure gradient and introducing the potential for a weather change. Finally, on January 15, 2009, at 06 UTC (see Figure 2.5 (e)), the weather map shows a significant shift in the synoptic environment. The low-pressure system had moved eastward, bringing a cold front towards Central Europe. This change indicated an impending breakdown of the stable high-pressure system that had dominated the region, leading to increased wind fields and potential precipitation in Austria. On January 15 at 12 UTC (see Figure 2.5 (f)), this front moves into Austria, which brought with it potential for precipitation, leading to the breakdown of the stable high-pressure system that had dominated the region for the past days.

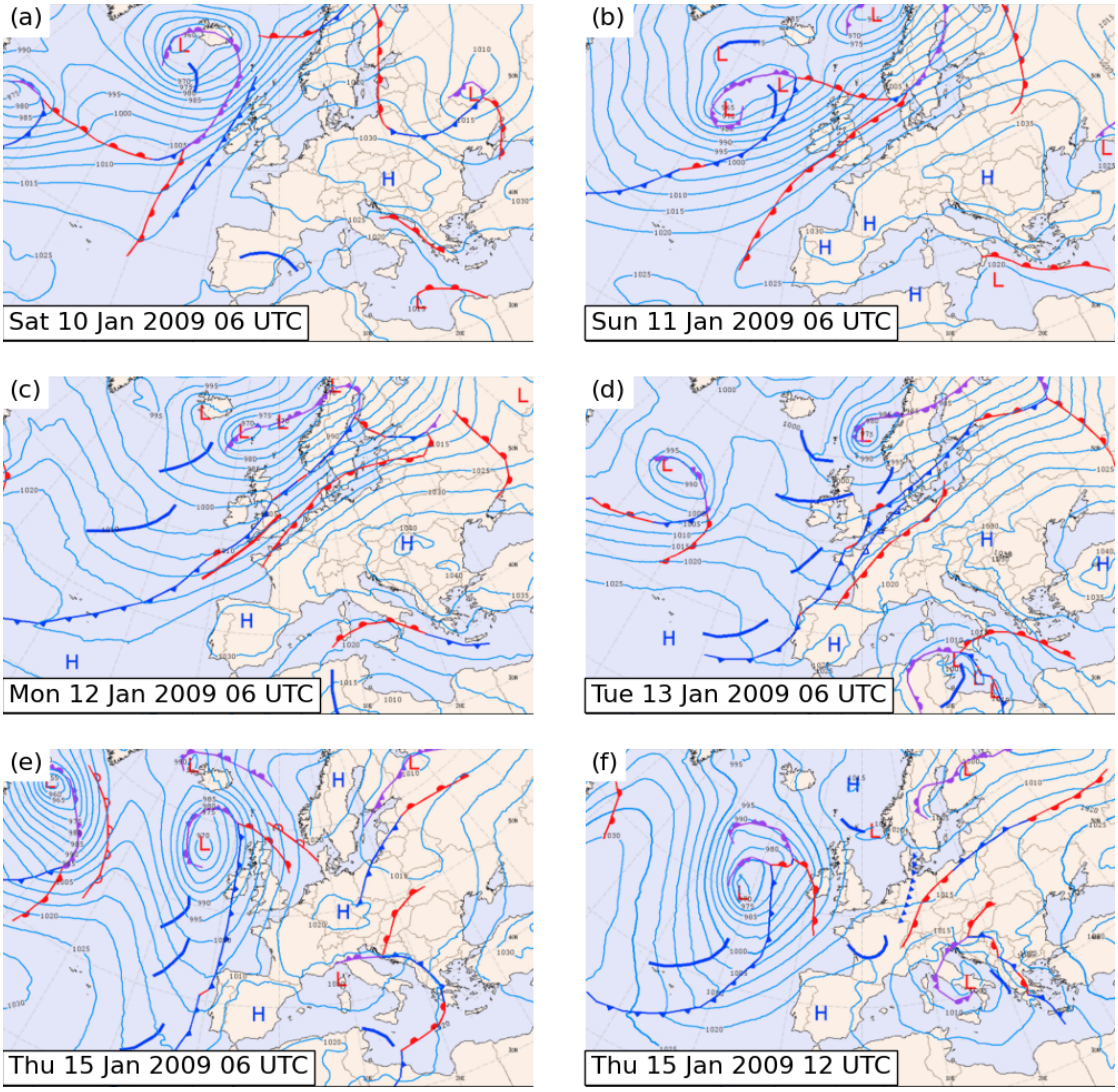


Figure 4.11: Appearance of a strong high-pressure system moving over Austria from (a) to (d) and the formation of a low-pressure system in the south of Austria in (e), which brings a weather change over the region and ends the anticyclonic weather situation as shown in (f).
source: Koninklijk Nederlands Meteorological Instituut (KNMI)

Although temperature inversions are generally a local phenomena (Hiebl and Schöner 2018), it was shown in Figure 4.6 that the synoptic weather situation can have an influence on the inversion magnitude. For the inversion event from January 10 to January 15, 2009, the lowest TSV of the whole study period from 1961 to 2020 was observed (TSV = −82.24 hPa). To investigate the spatial extend of the inversion event in January 2009, radio sonde data from Graz (Austria), Ljubljana (Slovenia), Zagreb (Croatia), and Udine (Italy) are analyzed. For the temperature profile of the radio sonde data the estimated real path of the balloon is used, as described in subsection 4.2.1. Since the weather situation during the event yields calm wind conditions, the balloon path does not deviate significantly from the starting position during the ascent.

In Figure 4.12 the radio sonde temperature profiles of Graz, Ljubljana, Zagreb and Udine are shown for the inversion event from January 10 to January 15. When looking at Figure 4.12(a), it can be seen that the data from Graz and Ljubljana, measured at January 10 03:00 UTC and 04:00 UTC, already start to show a similar behavior, with a strong inversion layer starting from the ground, while the data from Zagreb (measured earlier at 00:00 UTC) is still showing a more mixed profile up to about 900 m. Whereas the data from Udine (measured at 00:00 UTC) shows a more mixed profile up to about 1200 m. From the January 11 to January 14 (Figure 4.12 (b) to (e)) the temperature profiles of Graz and Ljubljana and Zagreb show a similar temperature profile, with the inversion layer bottom at about 800 m and the inversion top at about 1500 m. This leads to an inversion layer thickness of about 700 m, with a maximum magnitude on January 13 of about 18 K. The radio sonde data from Udine shows no distinct inversion layer, but instead a regular temperature profile with a slight decrease in temperature with height. On January 15 (Figure 4.12 (f)) the data from Graz still shows a very slight inversion layer, while the data from Zagreb already shows a neutral profile, with almost no temperature decrease with height.

This results show the large scale of the inversion event, with the inversion layer being present in a similar way in Graz, Ljubljana and Zagreb. And the assumption that the inversion event is driven by the strong high pressure system and the associated subsidence, is supported by the radio sonde data.

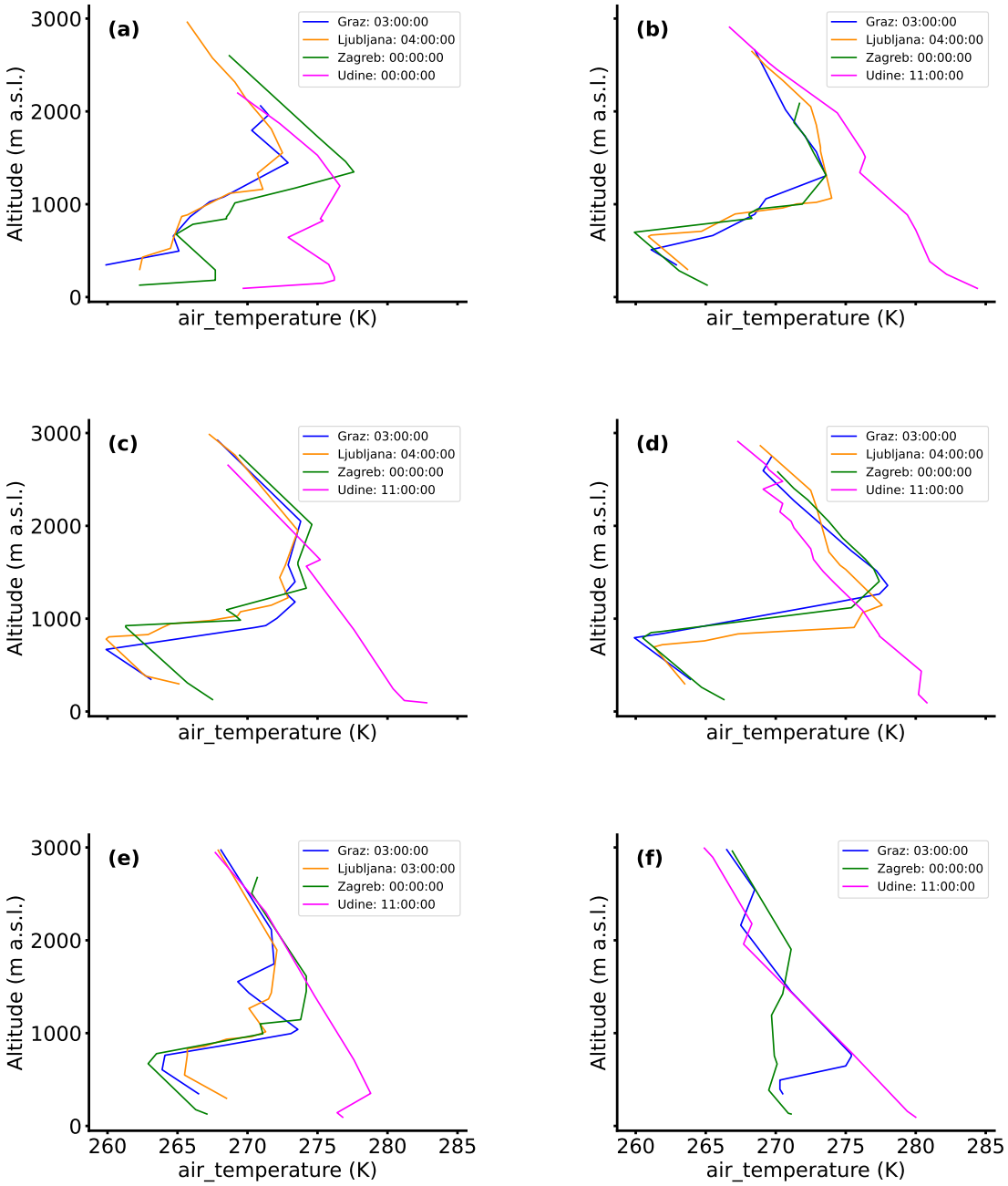


Figure 4.12: Radio Sonde temperature profiles of Graz (Austria), Ljubljana (Slovenia), Zagreb (Croatia), and Udine (Italy) for January 10 (a) to January 15 (f).

Since the inversion event from January 10 to January 15, 2009, seems to be primary driven by the strong high pressure system and the associated subsidence, it is assumed that the COSMO model in CLimate Mode (CCLM) simulations introduced in section 3.2 are able to capture the inversion event.

In Figure 4.13 the PTP of SPARTACUS and the directly nested simulation (CCLM-3km) and the simulation using a two-step nesting approach (CCLM-nested-3km) are shown for the inversion event from January 10 to January 15. It should be mentioned that the PTP of SPARTACUS and the two simulations are created slightly different: Whereas SPARTACUS PTP are created as described in subsection 3.5.1, the PTP of the simulations are created using the lowest three model levels, which are at about 0 m, 20 m and 50 m above ground instead of 2 m temperature only. This assures smoother profiles, with a more prominent inversion layer. Since otherwise on the model grid too little grid points at certain heights lead to a very noisy profile. Whereas SPARTACUS shows a prominent inversion layer for January 10 (Figure 4.13 (a)) starting from 750 m, the two simulations show an inversion layer but with a far lower magnitude and the inversion layer starting already at the ground at about 7 K higher temperatures. As the event progresses the inversion layer of SPARTACUS gets more intense, with a magnitude of almost 12 K on January 12 and January 13 (Figure 4.13 (c), (d)), while the two simulations get the lapse rate inside the inversion layer, they both start from the bottom, leading to a underestimated inversion magnitude. Although this is only speculation, it seems that the two simulations get closer to the SPARTACUS PTP the longer the event persists. When comparing CCLM-3km and CCLM-nested-3km, their is no big difference, although CCLM-3km does have a slightly higher inversion bottom for every day of the event, yet the inversion top is almost the same for both simulations.

Table 4.8: Mean Inversion Parameters of Jan 10 - Jan 15

Mean inversion parameters for the inversion event from Jan 10 to Jan 15, 2009. IB: inversion bottom; IT: inversion top.

source	magnitude (K)	IB (m)	IT (m)	intensity (K/ 100 m)
Radio Sonde	12.1	570	1328	1.8
SPARTACUS	9.1	667	1533	1.0
Simulation-3km	5.6	333	1250	0.6
Simulation-nested-3km	6.8	267	1333	0.6

In Table 4.8 the mean inversion parameters of the inversion event from January 10 to January 15 are shown for the radio sonde data of Graz, SPARTACUS and the two simulations. It should be noted that the values of the radio sonde can not directly be compared to the PTP of the simulations, since the inversions could be different in the free atmosphere than along the orography (Dreiseitl 1988; Pepin and Norris 2005). Additionally the radio sonde data is measured at 03:00 UTC, while the PTP are created using daily minimum temperatures. Again the inversion magnitude of SPARTACUS is closer to the radio sonde data than the two simulations, which both underestimate the inversion magnitude. The inversion layer bottom of the two simulations both are too low, whereas the inversion top is almost the same for all three data sets. The intensity of the inversion layer is also underestimated by the two simulations, which of course comes from the underestimated inversion magnitude. Since the elevation of the inversion layer bottom of a subsidence inversion is often related to the height of the boundary layer (Largeron and Staquet 2016; Stull 2012), the underestimated inversion layer bottom of the two simulations could be related to the underestimated mixed layer height in the simulations. An additional factor contributing to the inversion layer height is the rate of subsidence, basically governed by the strength of the high-pressure system (Namias 1935). Godowitch et al. (1985) state that the boundary layer in urban areas can lift the inversion layer bottom upwards. Since the Basin of Graz has many low elevated non urban areas, it seems that this might not be the case for the inversion event from January 10 to January 15, 2009. Both factors are worth investigating in future studies, to get a better understanding of the underestimated inversion layer height in the CCLM simulations.

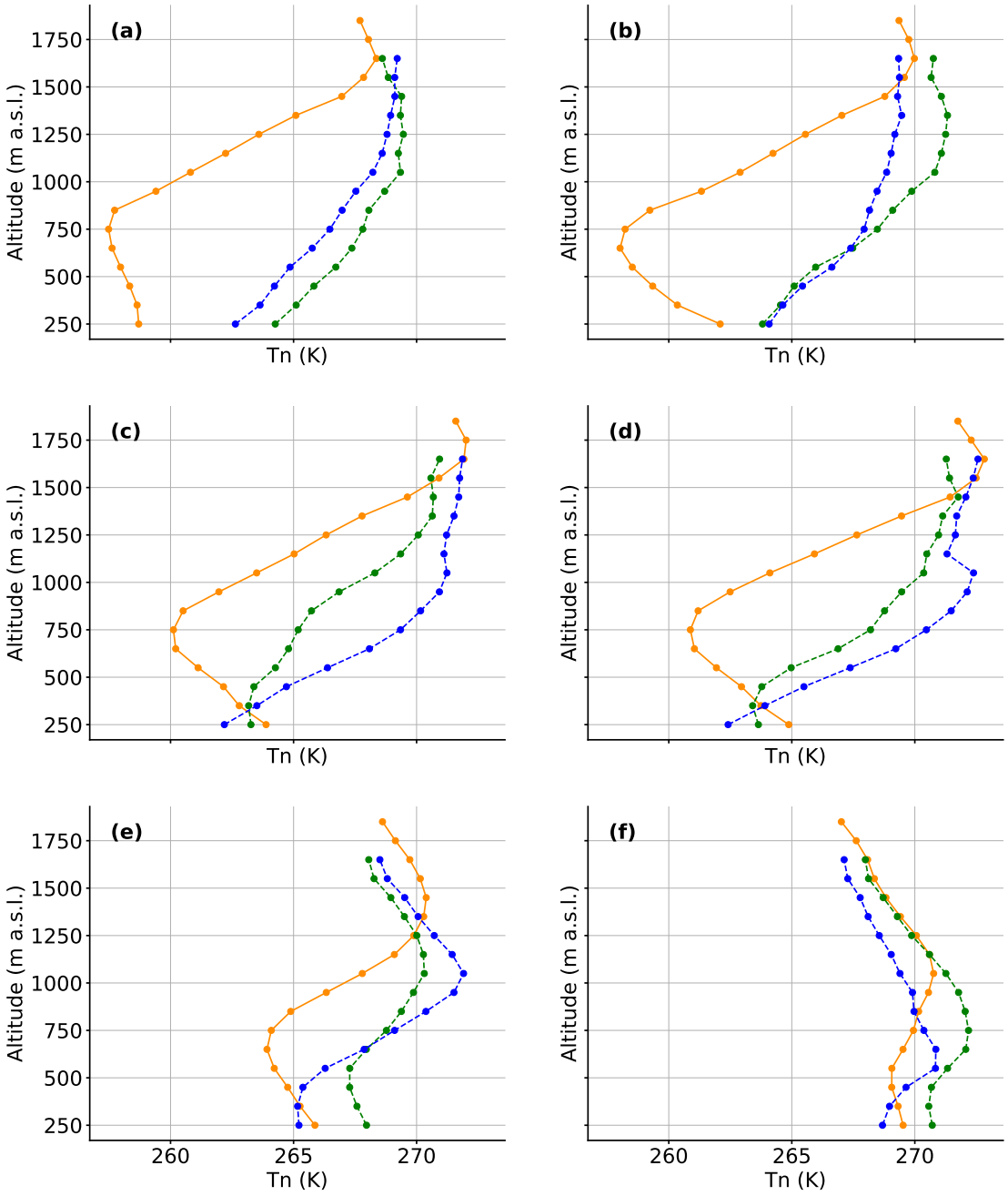


Figure 4.13: Pseudo temperature profiles of Spatiotemporal Reanalysis Dataset for Climate in Austria (SPARTACUS) (orange), CCLM-3km (green) and CCLM-nested-3km (blue) for January 10 (a) to January 15 (f).

4.2.2 Representation in CCLM

Snow Cover and Direct Solar Radiation

It is shown in Billings et al. (2006) that the snow cover can have a significant effect on the build up and persistence of the inversion layer. Therefore the snow cover during the inversion event from January 10 to January 15, 2009, is analyzed.

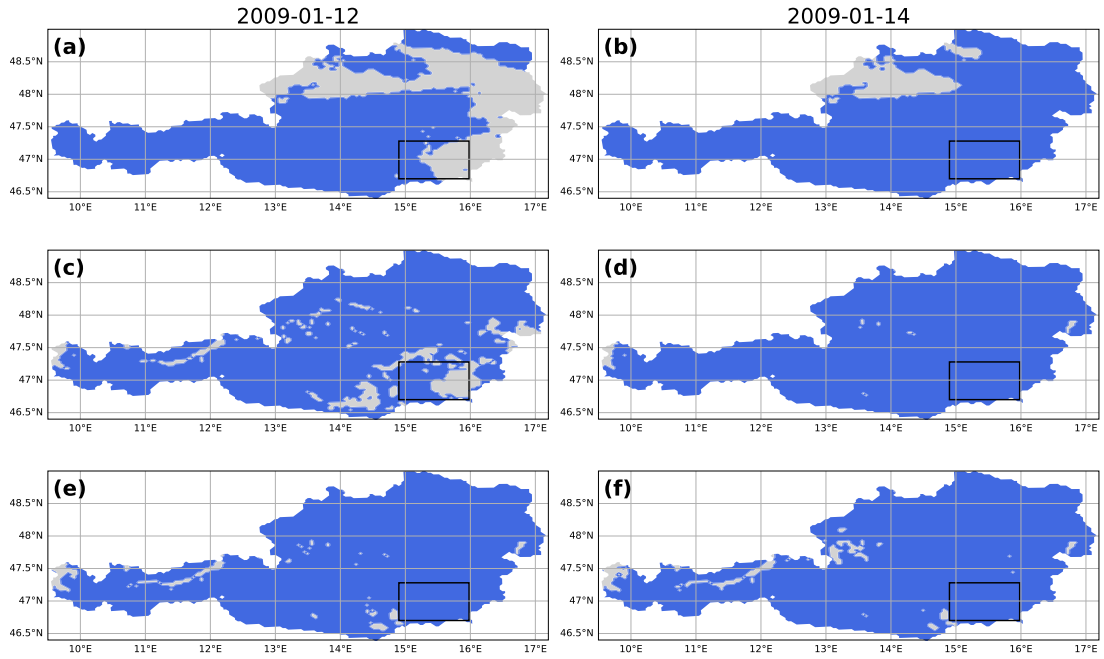


Figure 4.14: Comparison of the snow cover in Austria for January 12 and January 14, 2009. Blue areas denote snow cover. Grey areas denote no snow cover. The left column shows January 12, 2009 and the right column January 14. The study domain is marked by the black box. (a, b) SNOWGRID, (c,d) CCLM-3km, (e,f) CCLM-nested-3km.

Figure 4.14 shows the snow cover in Austria for January 12 and January 14, 2009. The reference snow cover (a, b) is from SNOWGRID, marking all areas with a snow depth of more than 0 cm as snow cover. It can be seen that for January 12, the observational data does not show any snow cover for a big part of the domain. This non covered area is mainly in the east of the domain, with altitudes below 500 m (compare Figure 3.2). The same is true for CCLM-3km, whereas CCLM-nested-3km shows a snow cover for the

whole study domain. For January 14, the observational data shows a snow cover for the whole study domain, which is also still present in both simulations. This amount of snow fall in the area of the city of Graz in the observational data, was probably already due to the weather change leading to the termination of the inversion event the next day.

It is also shown that the snow cover representation in the simulations can be different to the reference data SNOWGRID, which could also have an effect on the temperature profiles, due to a different radiation budget. With CCLM-nested-3km having snow cover in the whole Basin of Graz, during the main part of the inversion event, while the observational data shows no snow cover for the basin up to 500 m. In Billings et al. (2006) it is shown that the snow cover can have a significant effect on build up and persistence of the inversion layer, also highlighting the added value of the model grid size.

Although the study does not investigate in the added value of even higher resolution simulations, findings like the wrongly represented snow cover in the Basin of Graz, could give an indication that higher resolution simulations could lead to a better representation of the local climate conditions, which is also stated in Billings et al. (2006).

In subsection 3.5.4 it was shown that the sunshine duration does have a significant influence on the maximum temperature on inversion days. Additionally it was shown that thethe inversion magnitude has an influence on the sunshine duration on inversion days (see Figure 4.10). In Figure 4.15 the direct solar radiation measured on the horizontal plane, is shown for January 12 and January 14, 2009. When comparing the direct solar radiation for January 12 between the observational data APOLIS (a) and the two simulations (c, e) in Figure 4.15, it can be seen that the observational data shows basically no radiation for the low level areas of the study domain. This is an indicator of a strong cloud cover inside the Basin of Graz. Whereas in the higher elevated areas, like Koralpe and Weinebene, the observational data shows an increased radiation. In both simulations the radiation is increased for the whole study domain, which is probably due to a missing or underrepresented cloud cover in the simulations for the Basin of Graz. Additionally both simulations show no significant difference between the solar radiation in the low level areas and the higher elevated areas (see Figure 4.15 (c, e)).

For January 14, the radiation in the observational data is slightly increased in the low level areas, especially when compared to the high level areas. Although the overall radiation is a lot lower than for January 12 (note that their are different colorbars for (a,

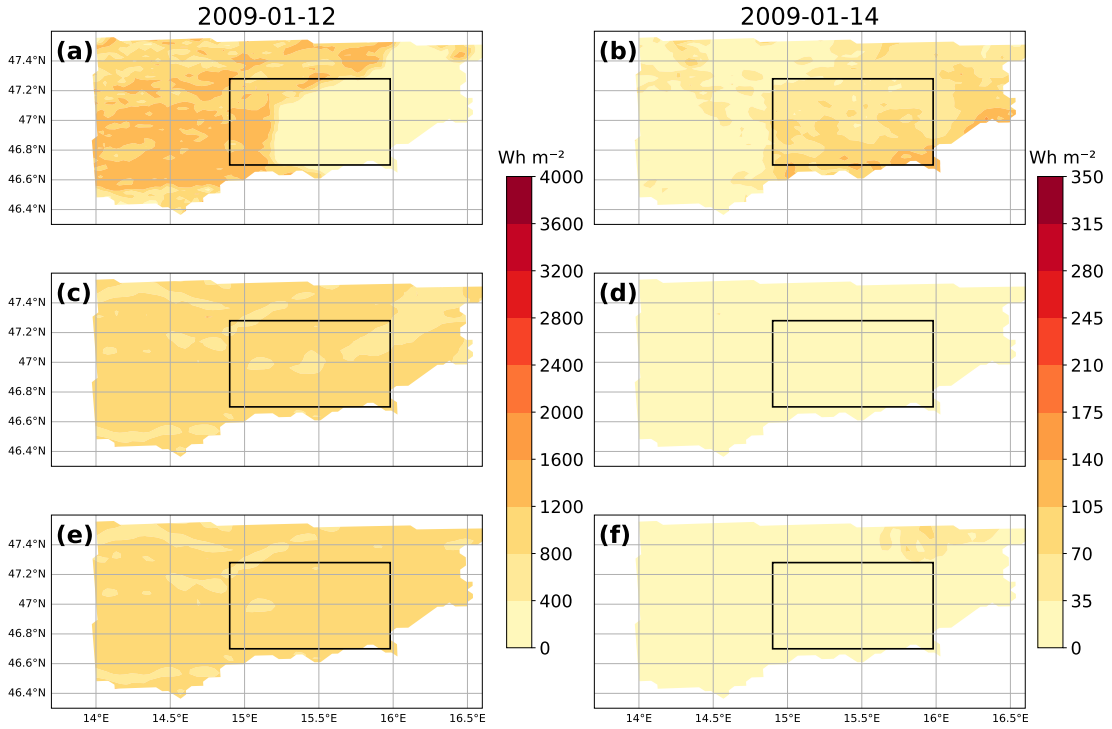


Figure 4.15: Daily sum of direct solar radiation for January 12 and January 14, 2009. The left column shows January 12, 2009 and the right column January 14. The study domain is marked by the black box.
(a, b) APOLIS, (c, d) CCLM-3km, (e, f) CCLM-nested-3km.

c, d) and (b, e, f)). In Figure 4.14 it was shown that snow fall occurred in SNOWGRID in the study domain on January 14. This could explain the overall decreased solar radiation and the missing difference between the low level areas and the higher elevated areas. Interestingly the two simulations both show a very low radiation for the whole study domain, which is an indicator of a strong cloud cover in the simulations.

While both simulations show a temperature inversion during the event, the direct solar radiation indicates an absence of a strong cloud cover in the Basin of Graz, which is prominent in the observational data. Although the direct solar radiation is not a direct indicator of the cloud cover, especially in the winter months the relationship between direct solar radiation and cloud cover is weaker due to the aerosol concentration in the stable atmosphere (Stjern et al. 2009). Not being able to represent the cloud cover (or the accumulation of aerosols) in the simulations can lead to an overestimation of

the radiation, which can lead to too warm temperatures in the basin. This absence of the cloud cover during the inversion event could possibly be attributed to the too low inversion layer bottom in the simulations, which leads to a too warm temperature in the basin, hence the point of condensation is not reached. This can explain the overall too warm temperatures of the simulations during the first days of the event. If the too high radiation in the simulations is due to the absence of the cloud cover or if its attributed to less aerosol accumulation in the lower atmosphere, is not addressed in this study.

Temperature Biases

Since the PTP are created along the orography the differences between the PTP of the simulations and SPARTACUS shown in Figure 4.13 should also be visible along the orography in spatial temperature plots. For this the mean bias of the inversion event from January 10 to January 15 is calculated as described in subsection 3.5.5. In

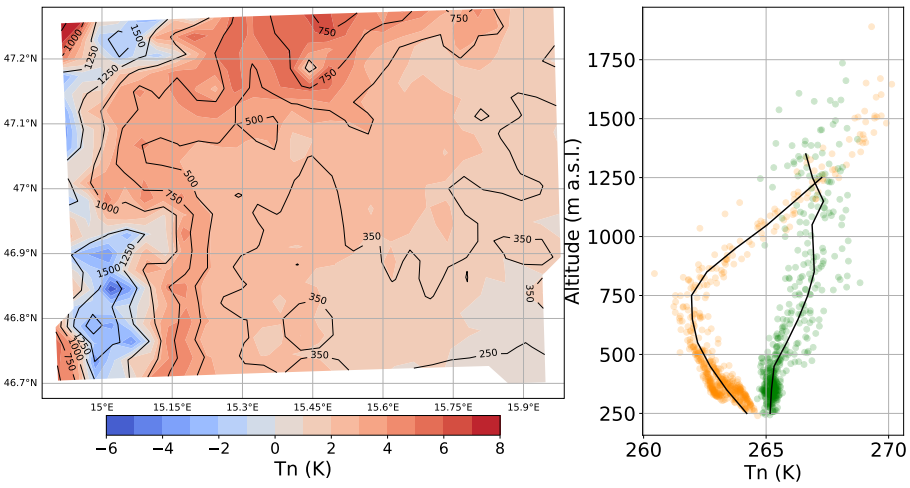


Figure 4.16: Mean bias of minimum temperatures and temperature profile of the inversion event from January 10 to January 15. Spatial bias of CCLM-3km and temperature profile of SPARTACUS (orange) and CCLM-3km (green). Dots show the individual grid points. Black line denotes the 100 m altitude zones mean profile.

Figure 4.16 the mean bias of CCLM-3km is shown for the inversion event from January

10 to January 15. The bias is calculated as described in subsection 3.5.5. Figure 4.16 (b) shows the mean PTP, based on daily minimum temperatures of the 3 km×3 km grid, for the event. Due to the simulation starting the inversion layer at the ground, the bias reaches its maximum at about the height of the inversion layer bottom, with values up to 8 K. This can be seen along the orography at about 500 m to 700 m. Although the mean bias is very low at the ground level, the simulation is too warm all the way up to the inversion layer top, which is at about 1250 m for the simulation. The lower inversion layer top of the simulation compared to SPARTACUS leads to too cold values above the inversion layer top.

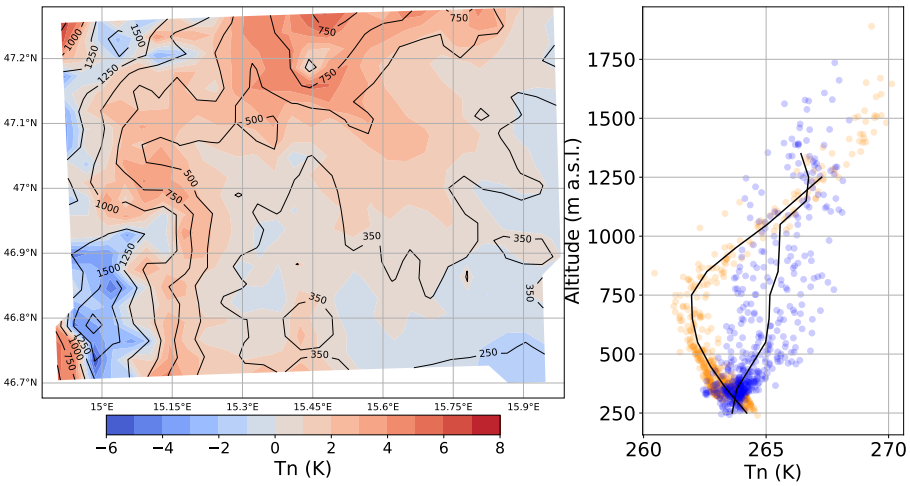


Figure 4.17: Mean bias of minimum temperatures and temperature profile of the inversion event from January 10 to January 15. Spatial bias of CCLM-nested-3km and temperature profile of SPARTACUS (orange) and CCLM-nested-3km (blue). Dots show the individual grid points. Black line denotes the 100 m altitude zones mean profile.

A similar picture can be seen for CCLM-nested-3km in Figure 4.17. Interestingly the variance of the mean PTP CCLM-nested-3km is much higher than for CCLM-3km, leading to locally lower biases (Figure 4.17 (b)). The bias of CCLM-nested-3km is also highest at the height of the inversion layer bottom, with values up to 7 K.

The analysis of the temperature bias for minimum temperatures (Figure 4.16 and Figure 4.17) can also be done for maximum temperatures. Since the maximum temperatures are highly influenced by the amount of direct solar radiation, it is expected that the

spatial bias of the maximum temperatures show even higher biases then the minimum temperatures.

Unfortunately for this analysis the height correction based on the SPARTACUS PTP described in subsection 3.5.5 can not be used. This is due the fact that the maximum temperatures are often reached at different times of the day for various elevations, especially at the presence of cloud cover, which would not lead to reliable PTPs. Therefore for the maximum temperature bias analysis the data is not height corrected. This should not influence the results significantly, since the simulations and the reference data are at the same spatial 3 km×3 km grid.

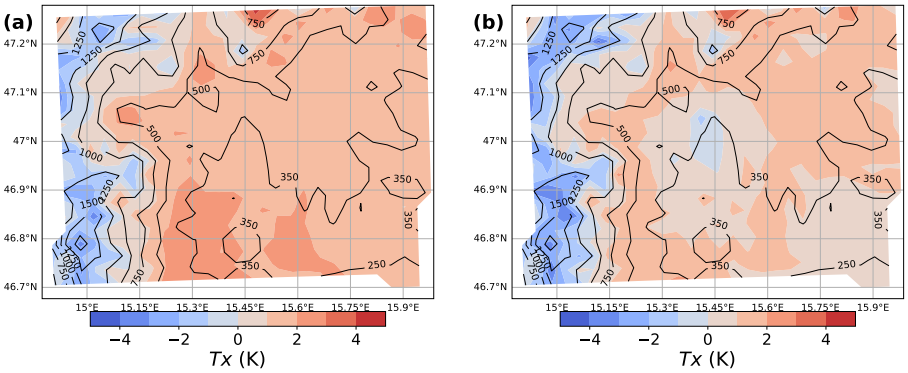


Figure 4.18: Mean bias of maximum temperatures of inversion event from January 10 to January 15 for both simulations. (a) Spatial maximum temperature bias of CCLM-3km.
(b) Spatial maximum temperature bias of CCLM-nested-3km.

The mean spatial bias of the maximum temperatures for the inversion event from January 10 to January 15 is shown for CCLM-3km (Figure 4.18 (a)) and CCLM-nested-3km (Figure 4.18 (b)). Both simulations show too warm temperatures in the low elevated Basin and too cold values for the higher elevated areas. Although the direct solar radiation is a lot higher in the simulations compared to the observational data (see Figure 4.15), the inversion layer also persists during the whole event in the simulations. This can be seen in the relatively low bias compared to the minimum temperature bias (see Figure 4.16 and Figure 4.17). Since the inversion magnitude decreases during the day in the observational data, the bias of the maximum temperatures is not as high as for the minimum temperatures. Nevertheless the bias is still significant, with values up to 4 K for CCLM-3km in the low elevated areas and −4 K for the higher elevated areas.

In Figure 6.4 in section 6 the mean PTP profiles of the inversion event from January 10 to January 15 are shown for SPARTACUS and the two simulations. It can be seen that the inversion layer bottom is a lot lower in the observational data, which leads to the lower temperature bias shown in Figure 4.18.

4.2.3 Temperature Profiles in the CORDEX-FPSCONV ensemble

To assess whether the underestimation of inversion magnitude, attributed to the unaccounted positive lapse rate from the ground to the inversion layer's base, is a common issue across different RCMs, the individual member of the CORDEX-FPSCONV ensemble (see subsection 3.1.7) are examined. The smoothing of orography in these models, with a resolution of 3 km×3 km, caps the maximum altitude for the PTP at 1400 m. Figure 4.19 presents the five-day mean PTP from January 10 to January 15, 2009, comparing it across various simulations, including CCLM-3km and CCLM-nested-3km and the reference data, SPARTACUS. Non of the simulations show the distinct inversion layer bottom at about 700 m as SPARTACUS does, although there are some models (marked by the dot-dashed line) that show a positive lapse rate at the surface.

Although the reason for the underestimation of the inversion magnitude in the simulations is not investigated in this study, potential reasons in the literature can be discussed: An important influence on temperature inversions is governed by the correct representation of the surface wind speeds, which play a crucial role in the formation and persistence of temperature inversions (Xu et al. 2019; Ganbat and Baik 2016). In Molina et al. (2024) the added value of km-scale multimodel ensembles such as the CORDEX-FPSCONV on wind speeds is shown. They highlight that the simulations show a better representation of the wind speeds compared to the reanalysis driving data, but also mentioned that this added value is less pronounced in winter and in higher altitudes. For the higher altitudes, the lower added value could be related to the growing influence of the free atmospheric flow, which is governed by large-scale forcing (Niermann et al. 2019). Nevertheless, some studies show that CCLM with the horizontal grid spacing of 3 km×3 km, and hence too smoothed orography, is not able to represent small-scale wind patterns. In Petrik et al. (2021) it is mentioned that the used CCLM simulations have difficulties to accurately represent the wind and temperature profiles in the boundary layer, especially in conditions with strong stratification in the observational data. All of these findings play a potential role in the found underestimation of the temperature inversions in the RCMs.

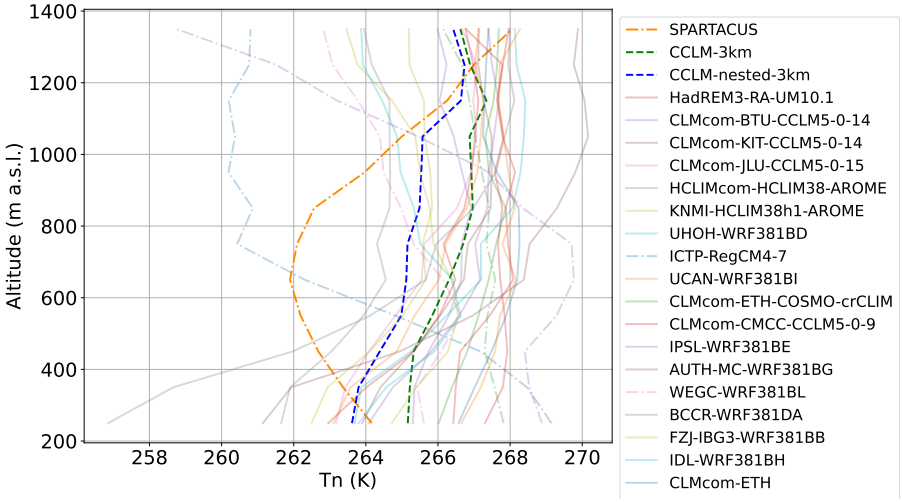


Figure 4.19: Comparison of the mean temperature profile over the curse of the inversion event (January 10 to January 15) for several ERA-Interim driven simulations and SPARTACUS and both CCLM-3km and CCLM-nested-3km. Dot-dashed line denotes models with a positive lapse rate at the surface.

Since it is shown in Figure 4.13 and Figure 4.19 that the two simulations CCLM-3km and CCLM-nested-3km as well as other RCMs have difficulties to represent this phenomenon adequately, the question arises if the long term trends of the local climate conditions are correctly represented in the RCMs. In this study two main issues of the representation of the inversion in the simulations occurred: The first issue is the underestimation of the inversion magnitude, which can lead to local temperature biases as well as possible biases in the long term trends. The second issue is the inversion layer bottom, which is found to be too low in the simulations, while the overall temperature profile on inversion days is too warm. This leads to too warm temperatures, especially at the height of the inversion layer bottom, which can lead to local biases of up to 8 K for minimum temperature and 12 K for maximum temperatures in the spatial bias plots. With the inversion layer top being also slightly too low, the temperature above the inversion layer top is generally found to be too cold during the event. This effect can be seen along the orography in the spatial bias plots. With the average inversion layer bottom at about 800 m and a inversion frequency of about 40 % in the winter months, this can also lead to local biases in seasonal temperature data of RCMs. However this effect could also be averaged out in seasonal means, if the inversion layer elevation is different

for different inversion events. This would imply that RCMs seasonal temperature biases are underestimated. These speculations are not further investigated in this study.

With the findings that the layer bottom has decreased between the two climate periods (see Figure 4.2), it is very likely that this change is not present in RCMs. This would lead to a change in the altitude dependent temperature biases over time in the RCMs.

It is also shown that the mentioned issues are not only present in the two CCLM simulations used in this study, but also in other RCMs such as the CORDEX-FPSCONV ensemble used in Coppola et al. (2020). While altitude dependent temperature biases are often associated with a wrong snow cover representation, this adds the possibility of miss interpretation of the temperature biases, especially in the winter months.

4.3 Reliability of the Study

In order to assess the robustness of the results, the limitations and deficiencies of the study are discussed in this section.

The reliability of the SPARTACUS dataset is crucial for the study, since it is used as a reference data for the PTP. Its performance in terms of represented temperature inversions is discussed in Hiebl and Schöner (2018). Although the method to produce the PTP used in this study is slightly different, the main limitations stay the same. Since the PTP are calculated using the grid points in the study domain (Figure 3.2), the underlaying assumption is that the vertical temperature profile is the same for the whole domain. While this assumption might be valid for temperature inversions with a large spatial extent, it might not be valid for small scale inversions, which are not captured by the PTP. Additionally the study domain includes the city of Graz, which can lead to a bias in the temperature profiles, especially in the situations with heat island effects in the summer months (Godowitch et al. 1985). This effect might be negligible in the winter months, which are the main focus of this study.
Another point of consideration is the maximum vertical extend of the study domain, limiting the PTP. This can lead to an underestimation of the inversion parameters, especially the thickness and intensity. This effect is investigated by looking at the number of inversions with their inversion layer tops at the maximum height of the study domain with at least 10 grid points: About 15% of the total amount of inversions have their calculated inversion tops at the maximum elevation. By looking at individual PTP of these inversions, it can be seen that the lapse rate inside the inversion layer is often already getting more neutral at the top of the study domain, leading to the conclusion that most of the inversions have their inversion layer tops close to the maximum height of the study domain.

An aspect not regarded in this study is that the gridded dataset comprises near-surface temperature, whereas the vertical distribution of the free valley atmosphere often differs significantly from temperatures on slopes (Dreiseitl 1988; Pepin and Norris 2005). A special issue related to the input data arises from the non-contemporaneity in the occurrence of observed daily temperature minima at meteorological stations and, consequently, across the gridded fields. For instance, the minimum temperature at a lower altitude might occur in the morning hours (steered by surface radiation), at a time when warming

might already have started at a higher altitude (steered by advection). This affects the detected daily grid-based profiles and can lead to both under- or overestimations of inversion parameters (Hiebl and Schöner 2018).

The issue with the low amount of grid points at certain elevations, leading to a noisy profile, is also present in the simulations. This is due to the smoothed orography in the simulations and the comparatively large model grid of 3 km×3 km. For this reason the PTP of the simulations are created using the lowest three model levels, which are at about 10 m, 30 m and 50 m above the surface. This assures smoother profiles, with a more prominent inversion layer. While this leads to a better representation of the inversion layer, it also makes comparison to the SPARTACUS PTP more difficult, since the SPARTACUS PTP are created using only the 2 m temperature.

The smoothed orography in the simulations, can lead to certain grid points laying at different elevations in the CCLM grid, compared to the SPARTACUS grid. This can lead to local temperature differences in the spatial bias plots. To minimize this effect the temperatures on the remapped SPARTACUS grid are interpolated to the model grid point elevations with the method described in subsection 3.5.5. The reason for interpolating SPARTACUS on to the CCLM and not the other way around, is that the SPARTACUS PTP are smoother and less noisy than the CCLM PTP. And additionally SPARTACUS with its smaller grid contains processes that are not resolved in CCLM.

It should also be mentioned here that the analysis is only based on the Basin of Graz, hence the results from the section 4.1 can not be generalized to other regions.

5 Summary and Conclusion

The primary goal of this thesis is to analyze temperature inversions and their changes over the last 60 years in the Basin of Graz, as well as to assess the representation of subsidence temperature inversions in state-of-the-art convection-permitting simulations. This includes investigating the seasonal trends, frequency, and magnitude of temperature inversions, and evaluating the accuracy of these phenomena in high-resolution climate models.

By assessing temperature profiles from the gridded dataset Spatiotemporal Reanalysis Dataset for Climate in Austria (SPARTACUS), the influence of temperature inversions on the local climate of Graz is in the period from 1961 to 2020 is examined. The findings reveal that temperature inversions play a significant role in the local climate dynamics of Graz. The primary inversion season spans from October to February, with the most intense inversions occurring in December and January, displaying a mean inversion magnitude of approximately 4 K. Over the last 60 years, there is an 11 % decrease in the frequency of temperature inversions in January. The inversion magnitude decreases by 0.4 K overall, with the most substantial reductions observed in December, January, and July. Comparing the climate periods 1961 to 1990 and 1991 to 2020 reveals a decrease in the mean inversion magnitude for all months from October to February, along with a significant lowering of the inversion layer bottom in winter. Additionally, the number of inversion events, defined as consecutive days with inversions, decreases over the past 60 years.

The study highlights that while synoptic weather conditions significantly influence the persistence of inversion events, they do not fully explain the variance in inversion strength. Changes in monthly weather type fractions indicate a shift towards less frequent anticyclonic and more frequent cyclonic weather types, particularly from August to November, accounting for the decrease in inversion events.

Using temperature station data from Graz University, the impact of temperature inversions on local temperatures is further investigated. The SPARTACUS-based temperature profiles facilitate the classification of inversion and non-inversion days. Results indicate that the mean seasonal temperature trend on inversion days differs significantly

from non-inversion days for both minimum and maximum temperatures. Specifically, the trend for mean winter minimum temperature is 0.1 K per decade higher on inversion days, and for mean winter maximum temperature, it is 0.2 K per decade higher on inversion days.

A multiple linear regression model indicates that the mean seasonal inversion magnitude can explain 59 % of the variance in minimum temperature data. The same model explains 59 % of the variance in maximum temperature data when sunshine duration is included as a predictor. Similar increases in the mean seasonal temperature trend on inversion days are found for sunshine duration data. While part of this trend can be explained by the inversion magnitude, the model accounts for only 33 % of the variance, suggesting other factors influence the sunshine duration trend on inversion days in Graz.

Motivated by the important role of temperature inversions on the observed temperature trend in Graz, the ability of convection permitting regional climate models to capture subsidence inversions is investigated with the COSMO model in CLimate Mode (CCLM). To this end, a particularly strong subsidence inversion event from January 2009 is simulated using ECMWF Reanalysis v5 (ERA5) as driving data. Two convection permitting simulations are conducted: one directly downscaling ERA5 to a 0.0275° grid (CCLM-3km) and the other using a nesting approach (CCLM-nested-3km). Comparisons reveal no significant added value from direct nesting in representing temperature inversions. Both models show strong temperature inversions during the event, but the inversion layer bottom is at lower elevations compared to observational data, and the temperature profiles are generally too warm at lower elevations. The inversion magnitude is underrepresented in the simulations.

These inaccuracies lead to biases in temperature, spatially attributed to locations at the inversion layer bottom's elevation in the observational data. The spatial bias reaches up to 8 K for minimum temperatures and 4 K for maximum temperatures in the Basin of Graz. The simulations also show excessively high values of direct solar radiation within the Basin of Graz during the event, significantly contributing to the spatial temperature bias, particularly for maximum temperatures. In contrast, observational data show reduced direct solar radiation inside the Basin of Graz and higher values at the surrounding mountains due to strong cloud cover during the inversion event.

A preliminary analysis of the evaluation runs of the CORDEX-FPSCONV ensemble show that a correct representation of subsidence inversion is still challenging for state-of-

the-art convection permitting models.

In conclusion, the inversion phenomenon significantly impacts the local climate of Graz. The trends in inversion parameters and their effects on local temperature trends underscore the necessity of accurately representing these phenomena in Regional Climate Modelss (RCMss). While the CCLM simulations show potential in capturing temperature inversions, improvements are needed in accurately representing inversion magnitude and layer bottom.

The current underrepresentation of inversion magnitude and misestimation of the inversion layer bottom leads to biases in temperature and radiation fields, which can significantly affect local climate and future climate projections. Further investigations in RCMs and higher-resolution simulations are warranted. Examining the mixed layer height in CCLM simulations could provide valuable insights into the mechanisms causing the underrepresentation of the inversion layer bottom. Additional analyses could focus on potential biases in local temperature trends in RCMs due to the underrepresentation of temperature inversions. Extending this study to include seasonal and long-term trends in temperature inversions in RCMss simulations would provide valuable insights.

Acronyms

CCLM COSMO model in CLimate Mode.

CDO Climate Data Operators.

CORDEX Coordinated Regional Climate Downscaling Experiment.

COSMO Consortium for Small-scale Modeling.

EBM Energy Balance Model.

ECMWF European Centre for Medium-Range Weather Forecasts.

ERA5 ECMWF Reanalysis v5.

GCMs Global Climate Models.

GLMs Generalized Linear Models.

OLS Ordinary Least Squares.

PTP Pseudo Temperature Profiles.

RCMs Regional Climate Models.

SLP sea-level pressure.

SPARTACUS Spatiotemporal Reanalysis Dataset for Climate in Austria.

TSV Total Shear Vorticity.

VIF Variance Inflation Factors.

VSC Vienna Scientific Cluster.

List of Figures

2.1 Components of the Climate System 5
2.2 Temperature and air- and vapor pressure profile of Earth's Atmosphere . 7
2.3 Atmospheric stability 8
2.4 Diurnal cycle in basins 10
2.5 Illustration of the process of subsidence inversion 12
2.6 Visualization of limited-area modelling 15

3.1 CCLM domains 21
3.2 Study domain 24
3.3 Definition of the inversion parameters 31
3.4 Jenkinson Collison Weather Types grid 32

4.1 Seasonality of inversion parameters 1961-2020 in Graz 41
4.2 Inversion parameter comparison of 1961-1990 against 1991-2020 44
4.3 Total number and duration of inversion events in Graz 46
4.4 Seasonality of weather types for 1961-1990 and 1991-2020 49
4.5 Regression Analysis of Weather Type Changes 51
4.6 Total Shear Vorticity (TSV) on inversion magnitude 53
4.7 Regression model of seasonal minimum temperature at station Graz University 55
4.8 Regression model of seasonal maximum temperature at station Graz University 58
4.9 Sunshine duration anomaly *so_h* at station Graz University 60
4.10 Regression model of seasonal sunshine duration *so_h* at station Graz University 62
4.11 Weather maps of January 2009 inversion event 66
4.12 Radio Sonde air temperature profiles 68
4.13 Simulation temperature profiles 71
4.14 Snow cover 72
4.15 Direct solar radiation 74
4.16 Spatial minimum temperatures bias CCLM-3km 75
4.17 Spatial minimum temperature bias CCLM-nested-3km 76

4.18 Spatial bias of maximum temperatures 77
4.19 Comparison of several ERA-Interim driven simulation temperature profiles 79

6.1 Model performance of seasonal minimum temperatures Tn at station Graz University 98
6.2 Model performance of seasonal maximum temperatures Tx at station Graz University 99
6.3 Regression model of seasonal sunshine duration so_h at station Graz University 100
6.4 Maximum Temperature profiles 101

List of Tables

3.1 Model configuration and parameterisations of CCLM-3km 20
3.2 Model configuration and parameterisations of CCLM-nested-3km 22

4.1 Monthly changes in Inversion Characteristics for Graz 42
4.2 Inversion Characteristics for Different Weather Types 48
4.3 Model Summary for $Y_{1991\text{-}2020}$ 52
4.4 Model Summary for Tn 56
4.5 Model Summary for Tn 56
4.6 Model Summary for Tx 59
4.7 Model Summary for so_h 63
4.8 Mean Inversion Parameters of Jan 10 - Jan 15 69

Bibliography

Ahrens, C. and R. Henson (2021). *Meteorology Today: An Introduction to Weather, Climate, and the Environment*. Cengage Learning. ISBN: 9780357452721.

Almbauer, R. A., M. Piringer, K. Baumann, D. Oettl, and P. J. Sturm (2000). "Analysis of the Daily Variations of Wintertime Air Pollution Concentrations in the City of Graz, Austria". 65, 1: pp. 79–87. DOI: 10.1023/A:1006464225727. URL: https://doi.org/10.1023/A:1006464225727.

Arguez, A. and R. S. Vose (2011). "The Definition of the Standard WMO Climate Normal: The Key to Deriving Alternative Climate Normals". 92, 6: pp. 699–704. DOI: 10.1175/2010BAMS2955.1. URL: https://journals.ametsoc.org/view/journals/bams/92/6/2010bams2955_1.xml.

Ban, N., C. Caillaud, E. Coppola, E. Pichelli, S. Sobolowski, M. Adinolfi, B. Ahrens, A. Alias, I. Anders, S. Bastin, D. Belušić, S. Berthou, E. Brisson, R. Cardoso, S. Chan, O. Christensen, J. Fernández, L. Fita, T. Frisius, and M. Zander (2021). "The first multi-model ensemble of regional climate simulations at kilometer-scale resolution, part I: evaluation of precipitation". 57. DOI: 10.1007/s00382-021-05708-w.

Bartholomé, E. and A. S. Belward (2005). "GLC2000: a new approach to global land cover mapping from Earth observation data". 26: pp. 1959–1977. DOI: https://doi.org/10.1080/01431160412331291297.

Behrens, D., O. Koland, and U. Leopold-Wildburger (2018). "Why local air pollution is more than daily peaks: modelling policies in a city in order to avoid premature deaths". 26. DOI: 10.1007/s10100-018-0534-y.

Billings, B. J., V. Grubišić, and R. D. Borys (2006). "Maintenance of a Mountain Valley Cold Pool: A Numerical Study". 134, 8: pp. 2266–2278. DOI: 10.1175/MWR3180.1. URL: https://journals.ametsoc.org/view/journals/mwre/134/8/mwr3180.1.xml.

Böhm, U., M. Kücken, W. Ahrens, A. Block, D. Hauffe, K. Keuler, B. Rockel, and A. Will (2006). "CLM—the climate version of LM: Brief description and long-term applications". 6: pp. 225–235.

Box, G. E. and D. R. Cox (1964). "An analysis of transformations". 26, 2: pp. 211–243.

Caballero, R. (2014). *Physics of the Atmosphere*. 2053-2563. IOP Publishing. ISBN: 978-0-7503-1052-9. DOI: 10.1088/978-0-7503-1052-9. URL: https://dx.doi.org/10.1088/978-0-7503-1052-9.

Charlson, R. J., S. Schwartz, J. Hales, R. D. Cess, J. Coakley Jr, J. Hansen, and D. Hofmann (1992). "Climate forcing by anthropogenic aerosols". 255, 5043: pp. 423–430.

Coppola, E., S. Sobolowski, E. Pichelli, F. Raffaele, B. Ahrens, I. Anders, N. Ban, S. Bastin, M. Belda, D. Belusic, A. Caldas-Alvarez, R. Cardoso, S. Davolio, A. Dobler, J. Fernández, L. Fita, Q. Fumiere, F. Giorgi, K. Goergen, and K. Warrach-Sagi (2020). "A first-of-its-kind multi-model convection permitting ensemble for investigating convective phenomena over Europe and the Mediterranean". 55. DOI: 10.1007/s00382-018-4521-8.

Davini, P. and F. D'Andrea (2016). "Northern Hemisphere Atmospheric Blocking Representation in Global Climate Models: Twenty Years of Improvements?" 29. DOI: 10.1175/JCLI-D-16-0242.1.

Dobesch, H. (1992). "On the variations of sunshine duration in Austria". 46: pp. 33–38.

Doms, G. and M. Baldauf (2013). *COSMO-Model Version 5.00: A Description of the Nonhydrostatic Regional COSMO-Model—Part I: Dynamics and Numerics*. Tech. rep. DOI: https://doi.org/10.5676/DWD_PUB/NWV/COSMO-DOC_5.00_I.

Dreiseitl (1988). "Slope and free air temperature in the Inn Valley". 39, 1: pp. 25–41.

Edwards, P. N. (2010). *A Vast Machine: Computer Models, Climate Data, and the Politics of Global Warming*. The MIT Press. ISBN: 9780262518635. URL: http://www.jstor.org/stable/j.ctt5hhds1 (visited on 02/12/2024).

Ernst Stadlober Siegfried Hörmann, B. P. (2008). "Quality and performance of a PM10 daily forecasting model". 42, 6: pp. 1098–1109. DOI: https://doi.org/10.1016/j.atmosenv.2007.10.073. URL: https://www.sciencedirect.com/science/article/pii/S1352231007009909.

FAO-Unesco (1981). *Soil map of the world 1:5000000*. Paris: Food and Agriculture Organization of the United Nations. URL: %7Bhttps://www.fao.org/3/as354e/as354e.pdf%7D%20[Accessed%206th%20July%202022].

Fernandez-Granja, J. A., S. Brands, J. Bedia, A. Casanueva, and J. Fernández (2023). "Exploring the limits of the Jenkinson–Collison weather types classification scheme: a global assessment based on various reanalyses". 61: pp. 1–17. DOI: 10.1007/s00382-022-06658-7.

Forkel, R., J. Werhahn, A. B. Hansen, S. McKeen, S. Peckham, G. Grell, and P. Suppan (2012). "Effect of aerosol-radiation feedback on regional air quality–A case study with WRF/Chem". 53: pp. 202–211.

Fox-Rabinovitz, M., J. Côté, B. Dugas, M. Déqué, and J. L. McGregor (2006). "Variable resolution general circulation models: Stretched-grid model intercomparison project (SGMIP)". 111, D16.

Ganbat, G. and J.-J. Baik (2016). "Wintertime winds in and around the Ulaanbaatar metropolitan area in the presence of a temperature inversion". 52: pp. 309–325. DOI: 10.1007/s13143-016-0007-y.

Gettelman, A. and R. B. Rood (2016). "Components of the Climate System". In: *Demystifying Climate Models: A Users Guide to Earth System Models*. Berlin, Heidelberg: Springer Berlin Heidelberg, pp. 13–22. ISBN: 978-3-662-48959-8. DOI: 10.1007/978-3-662-48959-8_2. URL: https://doi.org/10.1007/978-3-662-48959-8_2.

Giorgi, F. and G. T. Bates (1989). "The Climatological Skill of a Regional Model over Complex Terrain". 117, 11: pp. 2325–2347. DOI: 10.1175/1520-0493(1989)117<2325:TCSOAR>2.0.CO;2. URL: https://journals.ametsoc.org/view/journals/mwre/117/11/1520-0493_1989_117_2325_tcsoar_2_0_co_2.xml.

Giorgi, F., C. Jones, G. R. Asrar, et al. (2009). "Addressing climate information needs at the regional level: the CORDEX framework". 58, 3: p. 175.

Glickman, T. and A. M. Society (2000). *Glossary of Meteorology*. American Meteorological Society. ISBN: 9781878220349.

Godowitch, J. M., J. K. S. Ching, and J. F. Clarke (1985). "Evolution of the Nocturnal Inversion Layer at an Urban and Nonurban Location". 24, 8: pp. 791–804. DOI: 10.1175/1520-0450(1985)024<0791:EOTNIL>2.0.CO;2. URL: https://journals.ametsoc.org/view/journals/apme/24/8/1520-0450_1985_024_0791_eotnil_2_0_co_2.xml.

Gohm, A., F. Harnisch, J. Vergeiner, F. Obleitner, R. Schnitzhofer, A. Hansel, A. Fix, B. Neininger, S. Emeis, and K. Schäfer (2009). "Air Pollution Transport in an Alpine Valley: Results From Airborne and Ground-Based Observations". 131, 3: pp. 441–463. DOI: 10.1007/s10546-009-9371-9. URL: https://doi.org/10.1007/s10546-009-9371-9.

Grimalt-Gelabert, M., M. Tomas-Burguera, G. Alomar-Garau, J. Martin-Vide, and M. García (2013). "Determination of the Jenkinson and Collison's weather types for the western Mediterranean basin over the 1948-2009 period: Temporal analysis". 26: pp. 75–94. DOI: 10.1016/S0187-6236(13)71063-4.

Hadzimustafic, J., S. Simic, and M. Fitzka (2013). "UV-radiation in the past: Reconstruction and long-term changes in Austria". In: *AIP Conference Proceedings*. Vol. 1531. 1. American Institute of Physics, pp. 868–871.

Haidar, A., H. Bayraktar, S. Tomov, J. Dongarra, and N. J. Higham (2020). "Mixed-precision iterative refinement using tensor cores on GPUs to accelerate solution of linear systems". 476, 2243: p. 20200110.

Haiden, T., A. Kann, C. Wittmann, G. Pistotnik, B. Bica, and C. Gruber (2011). "The Integrated Nowcasting through Comprehensive Analysis (INCA) System and Its Validation over the Eastern Alpine Region". 26, 2: pp. 166–183. DOI: 10.1175/

2010WAF2222451.1. URL: https://journals.ametsoc.org/view/journals/wefo/26/2/2010waf2222451_1.xml.

"Global Physical Climatology" (2016). In: *Global Physical Climatology (Second Edition)*. Ed. by D. L. Hartmann. Second Edition. Boston: Elsevier, p. iv. ISBN: 978-0-12-328531-7. DOI: https://doi.org/10.1016/B978-0-12-328531-7.00022-0. URL: https://www.sciencedirect.com/science/article/pii/B9780123285317000220.

Hasselmann, K. (1976). "Stochastic climate models, Part I, Theory". 28: p. 473. DOI: 10.3402/tellusa.v28i6.11316.

Hersbach, H. et al. (2020). "The ERA5 global reanalysis". 146, 730: pp. 1999–2049. DOI: https://doi.org/10.1002/qj.3803. eprint: https://rmets.onlinelibrary.wiley.com/doi/pdf/10.1002/qj.3803. URL: https://rmets.onlinelibrary.wiley.com/doi/abs/10.1002/qj.3803.

Hiebl, J. and W. Schöner (2018). "Temperature inversions in Austria in a warming climate changes in space and time". 27. DOI: 10.1127/metz/2018/0899.

Hörmann, S., E. Stadlober, and B. Pfeiler (2005). "Analysis and Prediction of Particulate Matter PM10 for theWinter Season in Graz". 34: pp. 307–326. DOI: 10.17713/ajs.v34i4.420.

Jacob, D., J. Petersen, B. Eggert, A. Alias, O. Christensen, L. Bouwer, A. Braun, A. Colette, M. Déqué, G. Georgievski, E. Georgopoulou, A. Gobiet, L. Menut, G. Nikulin, A. Haensler, N. Hempelmann, C. Jones, K. Keuler, S. Kovats, and P. Yiou (2014). "EURO-CORDEX: New high-resolution climate change projections for European impact research". 14. DOI: 10.1007/s10113-013-0499-2.

Jacob, D., C. Teichmann, S. Sobolowski, ·. Katragkou, I. Anders, M. Belda, R. Benestad, F. Boberg, E. Buonomo, R. Cardoso, A. Casanueva, O. Christensen, J. Christensen, E. Coppola, L. De Cruz, ·. Davin, A. Dobler, M. Domínguez, R. Fealy, and ·. Wulfmeyer (2020). "Regional climate downscaling over Europe: perspectives from the EURO-CORDEX community". 20. DOI: 10.1007/s10113-020-01606-9.

James, G., D. Witten, T. Hastie, R. Tibshirani, et al. (2013). *An introduction to statistical learning*. Vol. 112. Springer.

Jans, J., P. Johansson, and J. P. Nilsson (2018). "Economic status, air quality, and child health: Evidence from inversion episodes". 61: pp. 220–232.

Jenkinson, A. and F. Collison (1977). "An initial climatology of gales over the North Sea". 62: p. 18.

Johann Hiebl, C. F. (2016). "Daily temperature grids for Austria since 1961—concept, creation and applicability". 124: pp. 161–178. URL: https://api.semanticscholar.org/CorpusID:121335904.

Johann Hiebl, C. F. (2017). “Daily precipitation grids for Austria since 1961—development and evaluation of a spatial dataset for hydroclimatic monitoring and modelling”. 132. DOI: 10.1007/s00704-017-2093-x.

Jones, P. W. (1999). “First- and Second-Order Conservative Remapping Schemes for Grids in Spherical Coordinates”. 127, 9: pp. 2204–2210. DOI: 10.1175/1520-0493(1999)127<2204:FASOCR>2.0.CO;2. URL: https://journals.ametsoc.org/view/journals/mwre/127/9/1520-0493_1999_127_2204_fasocr_2.0.co_2.xml.

Jury, M., S. Herrera García, J. Gutiérrez, and D. Barriopedro (2019). “Blocking representation in the ERA-Interim driven EURO-CORDEX RCMs”. 52. DOI: 10.1007/s00382-018-4335-8.

Kassomenos, P., A. Paschalidou, S. Lykoudis, and I. Koletsis (2014). “Temperature inversion characteristics in relation to synoptic circulation above Athens, Greece”. 186. DOI: 10.1007/s10661-014-3632-x.

Kassomenos, P. A. and I. Koletsis (2005). “Seasonal variation of the temperature inversions over Athens, Greece”. 25. URL: https://api.semanticscholar.org/CorpusID:129363808.

Kim, K.-E., H.-Y. Ko, H. Bok-Haeng, and K.-J. Ha (2010). “A Case Study on the Development of an Elevated Subsidence Inversion Over a Surface Low Pressure System”. 31. DOI: 10.5467/JKESS.2010.31.5.531.

Lamb, H. H. (1972). “British isles weather types and a register of the daily sequence of circu lation patterns 1861-1971”.

Largeron, Y. and C. Staquet (2016). “The Atmospheric Boundary Layer during Wintertime Persistent Inversions in the Grenoble Valleys”. 4. DOI: 10.3389/feart.2016.00070.

Li, J., H. Chen, Z. Li, P. Wang, M. Cribb, and X. Fan (2015). “Low-level temperature inversions and their effect on aerosol condensation nuclei concentrations under different large-scale synoptic circulations”. 32: pp. 898–908.

Lutgens, F. and E. Tarbuck (2013). *The Atmosphere: An Introduction to Meteorology*. Pearson. ISBN: 9780321756312.

Manabe, S. and R. T. Wetherald (1967). “Thermal Equilibrium of the Atmosphere with a Given Distribution of Relative Humidity”. 24, 3: pp. 241–259. DOI: 10.1175/1520-0469(1967)024<0241:TEOTAW>2.0.CO;2. URL: https://journals.ametsoc.org/view/journals/atsc/24/3/1520-0469_1967_024_0241_teotaw_2_0_co_2.xml.

Maraun, D., H. Truhetz, and A. Schaffer (2021). “Regional Climate Model Biases, Their Dependence on Synoptic Circulation Biases and the Potential for Bias Adjustment: A Process-Oriented Evaluation of the Austrian Regional Climate Projections”. 126. DOI: 10.1029/2020JD032824.

Mellor, G. and T. Yamada (1982). "Development of a turbulence closure model for geophysical fluid problems". 20: pp. 851–875. DOI: https://doi.org/10.1029/RG020i004p00851.

Molina, M., J. Careto, C. Gutiérrez, E. Sanchez, K. Goergen, S. Sobolowski, E. Coppola, E. Pichelli, N. Ban, D. Belušić, C. Short, C. Caillaud, A. Dobler, Ø. Hodnebrog, S. Kartsios, G. Lenderink, H. de Vries, O. Göktürk, J. Milovac, and P. Soares (May 2024). "The added value of simulated near-surface wind speed over the Alps from a km-scale multimodel ensemble": pp. 1–19. DOI: 10.1007/s00382-024-07257-4.

Moran, J., M. Morgan, and P. Pauley (1997). *Meteorology: The Atmosphere and the Science of Weather*. Prentice Hall. ISBN: 9780132667012.

Namias, J. (1935). "SUBSIDENCE WITHIN THE ATMOSPHERE". 16, 1: pp. 20–21. DOI: 10.1175/1520-0477-16.1.20. URL: https://journals.ametsoc.org/view/journals/bams/16/1/1520-0477-16_1_20.xml.

Niermann, D., M. Borsche, A. Kaiser-Weiss, and F. Kaspar (2019). "Evaluating renewable-energy-relevant parameters of COSMO-REA6 by comparison with satellite data, station observations and other reanalyses". DOI: 10.1127/metz/2019/0945.

Olefs, D. and D. Schoener (2012). "A new solar radiation model for research and applications in Austria". In: *EGU General Assembly Conference Abstracts*. EGU General Assembly Conference Abstracts, p. 9705.

Olefs, M., H. Formayer, A. Gobiet, T. Marke, W. Schöner, and M. Revesz (2021). "Past and future changes of the Austrian climate – Importance for tourism". Editorial: Tourism and Climate Change – an integrated look at the Austrian case. 34: p. 100395. DOI: https://doi.org/10.1016/j.jort.2021.100395. URL: https://www.sciencedirect.com/science/article/pii/S2213078021000311.

Olefs, M., R. Koch, W. Schöner, and T. Marke (2020). "Changes in Snow Depth, Snow Cover Duration, and Potential Snowmaking Conditions in Austria, 1961–2020—A Model Based Approach". 11, 12. DOI: 10.3390/atmos11121330. URL: https://www.mdpi.com/2073-4433/11/12/1330.

Pepin, N. and J. Norris (2005). "An examination of the differences between surface and free-air temperature trend at high-elevation sites: Relationships with cloud cover, snow cover, and wind". 110, D24.

Pepin, N., R. Bradley, H. Diaz, M. Baraer, B. Cáceres, N. Forsythe, H. Fowler, G. Greenwood, M. Hashmi, X. Liu, J. Miller, L. Ning, A. Ohmura, E. Palazzi, I. Rangwala, W. Schöner, I. Severskiy, M. Shahgedanova, M. Wang, and D. Yang (Apr. 2015). "Elevation-dependent warming in mountain regions of the world". 5: pp. 424–430. DOI: 10.1038/nclimate2563.

Petrik, R., B. Geyer, and B. Rockel (2021). "On the diurnal cycle and variability of winds in the lower planetary boundary layer: evaluation of regional reanalyses and hindcasts". 73: pp. 1–28. DOI: 10.1080/16000870.2020.1804294.

Prein, A. and A. Gobiet (2011). *NHCM-1: Non-hydrostatic climate modelling Part I: Defining and Detecting Added Value in Cloud Resolving Climate Simulations*. Tech. rep.

Prein, A. F., W. Langhans, G. Fosser, A. Ferrone, N. Ban, K. Goergen, M. Keller, M. Tölle, O. Gutjahr, F. Feser, E. Brisson, S. Kollet, J. Schmidli, N. P. M. van Lipzig, and R. Leung (2015). "A review on regional convection-permitting climate modeling: Demonstrations, prospects, and challenges". 53, 2: pp. 323–361. DOI: https://doi.org/10.1002/2014RG000475. eprint: https://agupubs.onlinelibrary.wiley.com/doi/pdf/10.1002/2014RG000475. URL: https://agupubs.onlinelibrary.wiley.com/doi/abs/10.1002/2014RG000475.

Raffa, M., A. Reder, M. Adinolfi, and P. Mercogliano (2021). "A Comparison between One-Step and Two-Step Nesting Strategy in the Dynamical Downscaling of Regional Climate Model COSMO-CLM at 2.2 km Driven by ERA5 Reanalysis". 12: p. 260. DOI: 10.3390/atmos12020260.

Ritter, B. and J. F. Geleyn (1992). "A comprehensive radiation scheme for numerical weather prediction models with potential applications in climate simulations". 120: pp. 303–325. URL: https://api.semanticscholar.org/CorpusID:120160324.

Rockel, B., A. Will, and A. Hense (2008). "The regional climate model COSMO-CLM (CCLM)". 17: pp. 347–348. DOI: 10.1127/0941-2948/2008/0309.

Schnelle Jr, K. B. and C. A. Brown (2016). *Air pollution control technology handbook*. CRC press.

Seabold, S. and J. Perktold (2010). "statsmodels: Econometric and statistical modeling with python". In: *9th Python in Science Conference*.

Sen, P. K. (1968). "Estimates of the regression coefficient based on Kendall's tau". 63, 324: pp. 1379–1389.

Severijns, C. and W. Hazeleger (2005). "Optimizing parameters in an atmospheric general circulation model". 18, 17: pp. 3527–3535.

Shepherd, T. (2014). "Atmospheric circulation as a source of uncertainty in climate change projections". 7: pp. 703–708. DOI: 10.1038/NGEO2253.

Stjern, C., E. Jón, J. Kristjánsson, and A. Walløe Hansen (2009). "Global dimming and global brightening: An analysis of surface radiation and cloud cover data in northern Europe". 29. DOI: 10.1002/joc.1735.

Stull, R. (2012). *An Introduction to Boundary Layer Meteorology*. Atmospheric and Oceanographic Sciences Library. Springer Netherlands. ISBN: 9789400930278.

Suklitsch, M., H. Truhetz, A. Prein, and A. Gobiet (2011a). *NHCM-1: Non-hydrostatic climate modelling Part II: Current state of selected cloud resolving regional climate models and their error characteristics*. Tech. rep.

– (2011b). "NHCM-1: Non-hydrostatic climate modelling Part III: Evaluation of the Local Climate Model Intercomparison Project (LocMIP) simulations".

Tadić, V., K. Gligorević, Z. Mileusnić, R. Miodragović, M. Hajmiler, and D. Radočaj (2023). "Agricultural Engineering Technologies in the Control of Frost Damage in Permanent Plantations". 5, 4: pp. 2079–2111. DOI: 10.3390/agriengineering5040128. URL: https://www.mdpi.com/2624-7402/5/4/128.

Tiedtke, M. (1989). "A Comprehensive Mass Flux Scheme for Cumulus Parameterization in Large-Scale Models". 117, 8: pp. 1779–1800. DOI: 10.1175/1520-0493(1989)117<1779:ACMFSF>2.0.CO;2.

Treut, L., R. Somerville, U. Cubasch, Y. Ding, C. Mauritzen, A. Mokssit, T. Peterson, M. Prather, D. Qin, M. Manning, Z. Chen, M. Marquis, K. Averyt, M. Tignor, H. Miller, and S. Solomon (2007). "Historical Overview of Climate Change Science". In: vol. 1, pp. 93–127.

Twomey, S. (1974). "Pollution and the planetary albedo". 8, 12: pp. 1251–1256.

Voggenberger, U., L. Haimberger, F. Ambrogi, and P. Poli (2023). "Balloon drift estimation and improved position estimates for radiosondes". 2023: pp. 1–29.

Wei, L., Z. Pu, and S. Wang (2013). "Numerical simulation of the life cycle of a persistent wintertime inversion over Salt Lake City". 148: pp. 399–418.

Xu, T., Y. Song, M. Liu, X. Cai, H. Zhang, J. Guo, and T. Zhu (2019). "Temperature inversions in severe polluted days derived from radiosonde data in North China from 2011 to 2016". 647: pp. 1011–1020. DOI: https://doi.org/10.1016/j.scitotenv.2018.08.088. URL: https://www.sciencedirect.com/science/article/pii/S0048969718330547.

Yang, X., C. Zhao, L. Zhou, Y. Wang, and X. Liu (2016). "Distinct impact of different types of aerosols on surface solar radiation in China". 121, 11: pp. 6459–6471.

Zardi, D. and C. D. Whiteman (2013). "Diurnal Mountain Wind Systems". In: *Mountain Weather Research and Forecasting: Recent Progress and Current Challenges*. Ed. by F. K. Chow, S. F. De Wekker, and B. J. Snyder. Dordrecht: Springer Netherlands, pp. 35–119. ISBN: 978-94-007-4098-3. DOI: 10.1007/978-94-007-4098-3_2. URL: https://doi.org/10.1007/978-94-007-4098-3_2.

6 Appendix

Appendix: Regression Analysis

In this section, the tables of the regression analysis are presented. The tables are the model summary output from the `statsmodels` Python module (Seabold and Perktold 2010).

Modelling Temperature Station Data

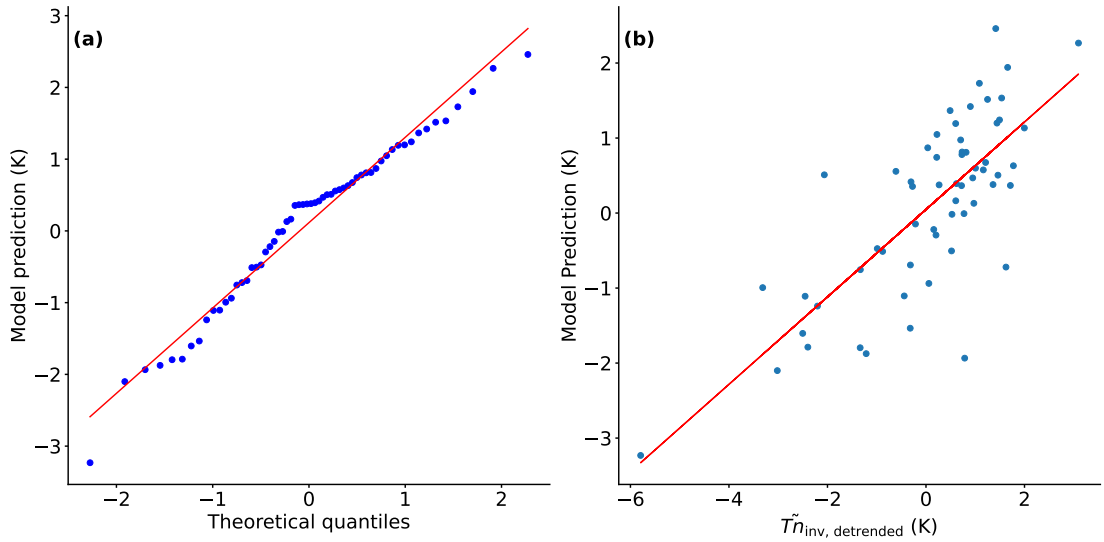


Figure 6.1: QQ-Plot (a) and correlation between the model and the observed data (b) of the regression model of seasonal minimum temperatures Tn at station Graz University. The linear regression model is based on the predictors: Temperature in non inversion days ($\tilde{Tn}_{\text{non-inv, detrended}}$) and inversion magnitude anomaly ($\tilde{M}$).

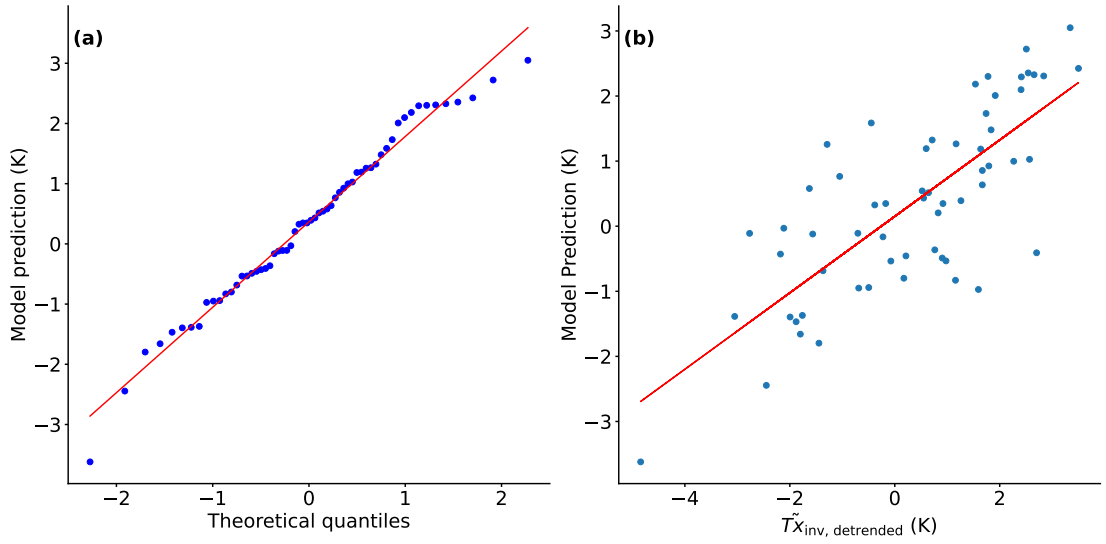


Figure 6.2: QQ-Plot (a) and correlation between the model and the observed data (b) of the regression model of seasonal maximum temperatures Tx at station Graz University. The linear regression model is based on the predictors: Temperature in non inversion days ($\tilde{T}x_{\text{non-inv, detrended}}$) and inversion magnitude anomaly ($\tilde{M}$) and sunshine duration so_h.

Sunshine Duration

Appendix: CCLM-profiles

The PTP based on the maximum temperature Tx is shown in Figure 6.4. This figure is not included in the main text, as the method used to calculate the PTP is not as reliable for maximum temperatures as for minimum temperatures. This is due the fact that the maximum temperatures are often reached at different times of the day for various elevations. Nevertheless, the figure provides an overview of the temperature profiles during the inversion event. It can be seen in Figure 6.4 that the temperature inversion bottom is located almost at the bottom of the domain in the observational data. Since the simulations generally underestimate the inversion layer bottom height, the temperature bias is a lot smaller for the maximum temperatures compared to the minimum temperatures.

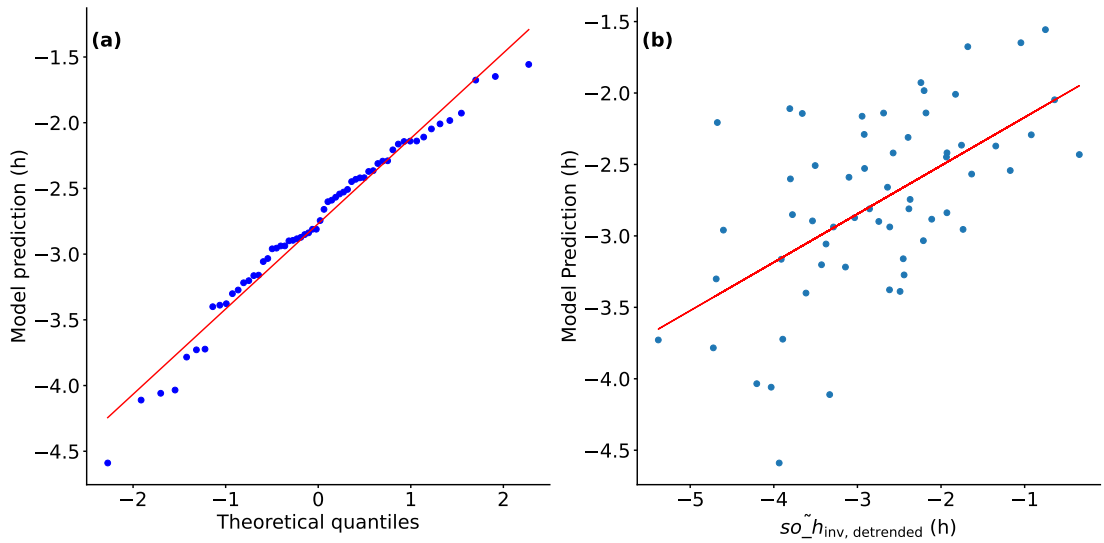


Figure 6.3: QQ-Plot (a) and correlation between the model and the observed data (b) of the regression model of seasonal sunshine duration *so_h* at station Graz University. The linear regression model is based on the predictors: Sunshine duration in non inversion days ($\tilde{so_h}_{\text{non-inv, detrended}}$) and inversion magnitude anomaly ($\tilde{M}$).

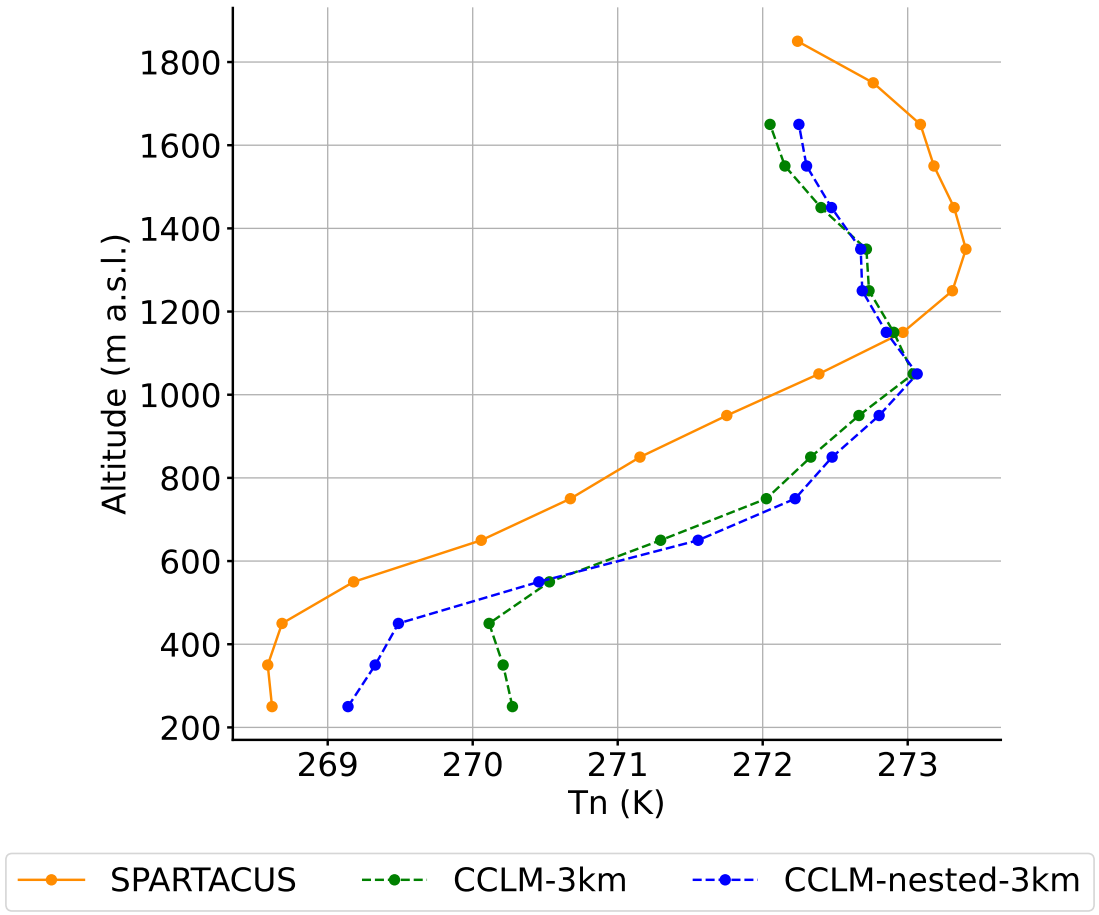


Figure 6.4: Pseudo Temperature Profiles (PTP) of maximum temperature Tx for the mean inversion event from 2009-01-10 to 2009-01-15. Note that the method used to calculate the PTP is not as reliable for maximum temperatures as for minimum temperatures. This is due the fact that the maximum temperatures are often reached at different times of the day for various elevations.

The Basin of Graz frequently experiences temperature inversions that significantly impact local temperatures, cloud cover, and aerosol accumulation. Long-term (period from 1961 to 2020) observational records of temperature in Graz indicate that the characteristics of inversions during winter time have changed due to climate change: the magnitude, the height, the frequency of occurrence as well as the intensity have decreased. The analysis of the weather types during inversion periods, i.e., periods with consecutive days of temperature inversions, shows that the occurrence of anticyclonic weather types has a significant impact on the formation and strength of temperature inversions in the Basin of Graz. A reduction in the frequency of the anticyclonic weather type relate to the found decrease in the number of inversion events over the last 60 years. Furthermore, the records show a stronger warming trend in winter on inversion days compared to non-inversion days, with an additional warming trend for minimum temperatures of 0.1K per decade and for maximum temperatures of 0.2K per decade. Multiple linear regression analyses show that inversion magnitude significantly contributes to the warming trend on local temperature during inversion days. For the seasonal maximum temperatures, increased sunshine duration additionally contributes significantly to the warming trend on inversion days. These findings highlight the critical need for accurate representation of temperature inversions in Regional Climate Models (RCMs), for reliable local climate assessments and future climate projections. To assess the performance of COSMO model in CLimate Mode (CCLM) in representing subsidence temperature inversions, convection permitting simulations with 3km×3km grid spacing of a large scale inversion event in January 2009 are conducted. The results indicate that CCLM captures the presence of the inversion quite well, however the model under represents the inversion magnitude and erroneously underestimates the inversion layer bottom height, introducing considerable biases in modeled temperature and radiation fields, with the biases reaching values of up to 8K for minimum temperatures and 4K for maximum temperatures.

A preliminary analysis of the evaluation runs of the CORDEX-FPSCONV ensemble shows that a correct representation of subsidence inversion is still challenging for stateof- the-art convection permitting models.

SR 109 | 2024 Evaluating the Performance of the CCLM in Representing Subsidence Inversions: A Case Study of the Basin of Graz
Wegener Center Verlag, University of Graz, Austria. ISBN 978-3-9505053-8-2